Electroweak Measurements Using Heavy Quarks Identified in e^+e^- Annihilation

by

Jonathan P. Rodin

Submitted to the Department of Physics
in partial fulfillment of the requirements for the degree of

Doctor of Philosophy

at the

MASSACHUSETTS INSTITUTE OF TECHNOLOGY

February 1998

Author . . . .
⌣
. . . .
Department of Physics
September 15 1997

Certified by . . . .
. . . .
Ulrich J Becker
Professor of Physics
Thesis Supervisor

Accepted by . . . .
George F Koster
Chairman, Departmental Committee on Graduate Students

Electroweak Measurements Using Heavy Quarks Identified in e^+e^- Annihilation

by

Jonathan P. Rodin

Abstract

Since 1989, the Large Electron Positron collider at CERN has been used to study electroweak physics to an unprecedented precision. The data have acted as spectacular confirmation of the Standard Model as the best description of electroweak interactions at scales of ~ 100 GeV. However, in 1995, a possible anomaly appeared in the LEP measurement of $R_b = \frac{\Gamma(Z \to b\bar{b})}{\Gamma(Z \to \text{hadrons})}$ which was more than three standard deviations above the Standard Model prediction. This effect could not be accounted for by minor adjustment of model parameters, in particular the mass of the top quark which had recently been directly measured at the Fermilab Tevatron. In order to investigate whether the deviation could be an indication of physics beyond the Standard Model we present new precise measurements of both R_b and the forward-backward asymmetry of b quark production, A^b_{FB} , using ~ 63 pb^{-1} of data at the Z peak recorded by the L3 detector during 1994-95. The results are:

$$R_b = 0.2146 \pm 0.0017(stat) \pm 0.0033(sys) - 0.139 \, (R_c - 0.171)$$
$$A^b_{FB} = 9.33 \pm 1.40(stat) \pm 0.65(sys) \pm 0.10(QCD)\%$$

This value for R_b agrees with the Standard Model to within one standard deviation. A^b_{FB} leads to a value for the effective weak mixing angle for b-quarks

$$\sin^2 \theta_w^{eff} = 0.2333 \pm 0.0025(stat) \pm 0.0012(sys)$$

which is consistent with values obtained using different decay modes of the Z and from neutrino physics, supporting flavour universality. We thus observe no deviation from the Standard Model and, from the R_b measurement, limit the effects of new physics to $< 1.7\%$ in b decays.

Thesis Supervisor: Ulrich J Becker
Title: Professor of Physics

Contents

1   Introduction

Particle Physics has reached a state of considerable maturity in recent times. The so-called 'Standard Model' [1] [2] [3] [4] has been successfully describing the interactions of quarks, leptons and gauge bosons for some thirty years. This is particularly demonstrated by measurements coming from the **Large Electron Positron** collider at CERN. Since 1989, LEP has been studying the annihilation of electron-positron pairs to fermion anti-fermion pairs at centre of mass energies at or near the mass of the Z boson to unprecedented precision. Results reported by the four LEP experiments have supported the Standard Model to a phenomenal degree of accuracy.

Beyond this overall agreement, the LEP results are precise enough to be sensitive to small ($\sim$ %) corrections to the Standard Model predictions due to processes beyond leading order (radiative corrections). This implies a sensitivity to what have been the two major unknowns of the model: the masses of the top quark and the Higgs boson.

The predictions for different physics channels are more or less effected by these unknowns. An example is the ratio

$$R_b = \frac{\Gamma_{Z \to b\bar{b}}}{\Gamma_{Z \to q\bar{q}}} \tag{1}$$

ie, the Z decay width to b-quarks divided by the Z decay width to any quark. A study of the effects of virtual top and Higgs through radiative corrections indicates that the Standard Model prediction for R_b is rather sensitive to m_{top} and rather insensitive to m_{higgs}. The uncertainty in the R_b prediction was dramatically reduced in 1994 with the announcement of the first observation of the top quark at Fermilab [5]. The very large observed mass of $m_{top} \sim 174$ GeV implied a rather low value for R_b.

However, although the Standard Model showed good consistency elsewhere, the average value of R_b measured by the LEP experiments exceeded the prediction by around three standard deviations. There seemed to be two possible solutions to the problem: either there was a common flaw in the LEP measurements giving an artificially high R_b or the Standard Model gave incorrect predictions in the heavy quark sector. The latter, if true, would be compelling evidence for new physics.

New precise measurements of R_b would be crucial in evaluating the significance of this effect. In 1994, the L3 experiment at LEP was in an excellent position to make such a measurement. A silicon vertex detector was newly installed which promised to drastically improve the identification of $Z \rightarrow b\bar{b}$ decays via the relatively long lifetime of B hadrons. Additionally, LEP was due to run at the Z peak with increased luminosity for two more years.

This thesis describes the attempts made, using $\sim$63 pb^{-1} of Z data taken with the L3 experiment in 1994 and 1995, to make two electroweak measurements in the heavy quark sector, R_b and the forward-backward asymmetry of $b\bar{b}$ production A^b_{FB} , to a precision sufficient to act as evidence either for or against a signal for new physics beyond the Standard Model description of $Z \rightarrow b\bar{b}$ decays.

The SM has been so successful in describing physics at the Z scale that even a small deviation from its predictions would have significant consequences on our ideas about fundamental interactions. On the other hand, if our new measurements are more in agreement with the predictions, we will have taken a significant step towards the complete understanding of electroweak physics at energies of order 100 GeV.

2 Z Physics at LEP: Theoretical Review

2.1 The Basic Process

We are concerned with the annihilation of e^+e^- pairs into fermion anti-fermion pairs which, at centre of mass energies around 90 GeV, proceeds predominantly via $e^+e^- \to Z \to f\bar{f}$ and $e^+e^- \to \gamma \to f\bar{f}$ see fig 1. Here, f is any fermion except the top quark which is too heavy to be produced at LEP.
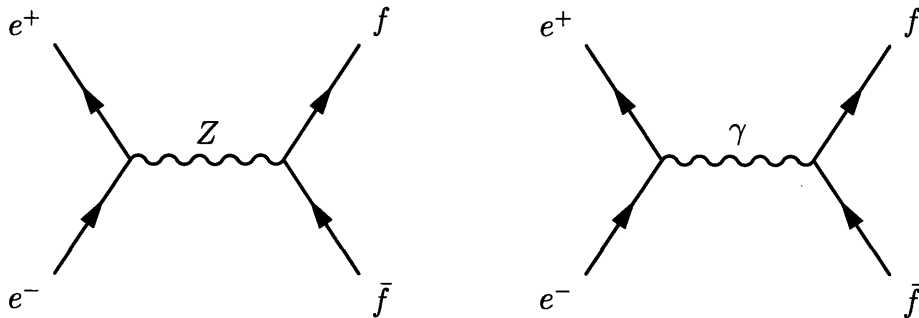
Figure 1: Lowest order Feynman diagrams for $e^+e^- \to f\bar{f}$ where f is any fermion.

To first order (the Born approximation), the differential cross section σ is given by three terms, corresponding to Z and γ mediators and an interference term:

$$\frac{d\sigma}{d\cos\theta} = \mathcal{B}_Z + \mathcal{B}_\gamma + \mathcal{B}_{Z\gamma} \qquad (2)$$

where θ is the angle between the incident electron and outgoing fermion.

The three terms are calculable in the electroweak Standard Model which is described in the Appendix. Here we just quote the results: [1]

$$
\begin{aligned}
\mathcal{B}_Z &= \frac{N_c^f G_F^2 m_Z^4 s}{64\pi[(s - m_z^2)^2 + m_Z^2 \Gamma_Z^2]} \\
&\times [(R_e^2 + L_e^2)(R_f^2 + L_f^2)(1 + \cos^2\theta) + 2((R_e^2 - L_e^2)(R_f^2 - L_f^2)\cos\theta] \\
\mathcal{B}_\gamma &= \frac{N_c^f \pi \alpha^2 Q_f^2}{2s}(1 + \cos^2\theta)
\end{aligned}
$$

$$\qquad (3)$$
$$\qquad (4)$$

---

[1] We have made the approximation that the fermions are massless. Also, these equations are not valid for $e^+e^- \to e^+e^-$ where t-channel photon exchange is important.

$$\begin{aligned}
\mathcal{B}_{Z\gamma} &= -\frac{N_c^f \alpha Q_f G_F m_Z^2 (s - m_Z^2)}{8\sqrt{2}[(s - m_Z^2)^2 + m_Z^2 \Gamma_Z^2]} \\
&\times \quad [(R_e + L_e)(R_f + L_f)(1 + \cos^2 \theta) + 2((R_e - L_e)(R_f - L_f)\cos\theta] \quad (5)
\end{aligned}$$

where Q_f is the charge of the outgoing fermion, N_c^f the number of fermion colours (1 for leptons, 3 for quarks), m_Z, Γ_Z the mass and width of the Z, $\sqrt{s}$ is the e^+e^- centre of mass energy and α, G_F are the QED and Fermi coupling constants respectively. R_f and L_f represent the couplings of the Z to left and right-handed fermions respectively. We may write them in terms of the vector, C_V^f, and axial-vector, C_A^f, couplings of the Z to fermion f (see appendix):

$$\begin{aligned}
C_V^f &= I_3^f - 2\sin^2\theta_w Q_f & (6) \\
C_A^f &= I_3^f & (7) \\
R_f &= C_V^f - C_A^f & (8) \\
L_f &= C_V^f + C_A^f & (9)
\end{aligned}$$

where I_3^f is the third component of weak isospin for fermion f and θ_w is the weak mixing angle.

It is apparent from the above that at LEP 1, where $\sqrt{s} \sim m_z$, Z exchange is dominant (by a factor $\sim$300). Consequently, we shall neglect γ exchange for now, although ultimately it will be taken into account when we quote final results (section 9.6).

2.2 Production of Heavy Quarks

The partial decay width of the Z to a particular $f\bar{f}$ pair in the Standard Model is:

$$\Gamma_{Z \to f\bar{f}} = \frac{1}{3} N_c m_Z \alpha ((c_V^f)^2 + (c_A^f)^2) \quad (10)$$

where c_v^f and c_A^f are closely related to C_v^f and C_A^f:

11

$$c_v^f = \frac{C_v^f}{2\sin\theta_w\cos\theta_w} \tag{11}$$

$$c_A^f = \frac{C_A^f}{2\sin\theta_w\cos\theta_w} \tag{12}$$

We can use equation 10 to make an estimate of the relative production of heavy (ie, b) quarks at LEP. If we take the ratio (equation(1))

$$R_b = \frac{\Gamma_{Z\to b\bar{b}}}{\Gamma_{Z\to q\bar{q}}}$$

N_c, m_Z and α cancel, leaving the result in terms of vector and axial-vector couplings of the Z to each type of quark, q, accessible at LEP:

$$R_b = \frac{(c_v^b)^2 + (c_a^b)^2}{\sum_q (c_v^q)^2 + (c_a^q)^2} \tag{13}$$

For $\sin^2\theta_w \sim 0.23$ [45], this gives $R_b \sim 0.2$, ie, about 20% of hadronic Z decays are expected to be to b-quarks. Higher order (radiative) corrections to this result are discussed below.

2.3 Forward Backward Asymmetry

Other aspects of the production of b-quarks in e^+e^- annihilation are sensitive to the electroweak coupling of the Z. An example is the forward-backward asymmetry.

An $e^+e^- \to b\bar{b}$ event, may be classified as *forward* or *backward* according to whether the projection of the outgoing b momentum along the beam line is parallel or anti-parallel to the direction of travel of the incident electron (see figure 2). For photon exchange, the process is forward-backward symmetric and the differential cross section follows the form:

$$\frac{d\sigma}{d\cos\theta} \propto 1 + \cos^2\theta \tag{14}$$
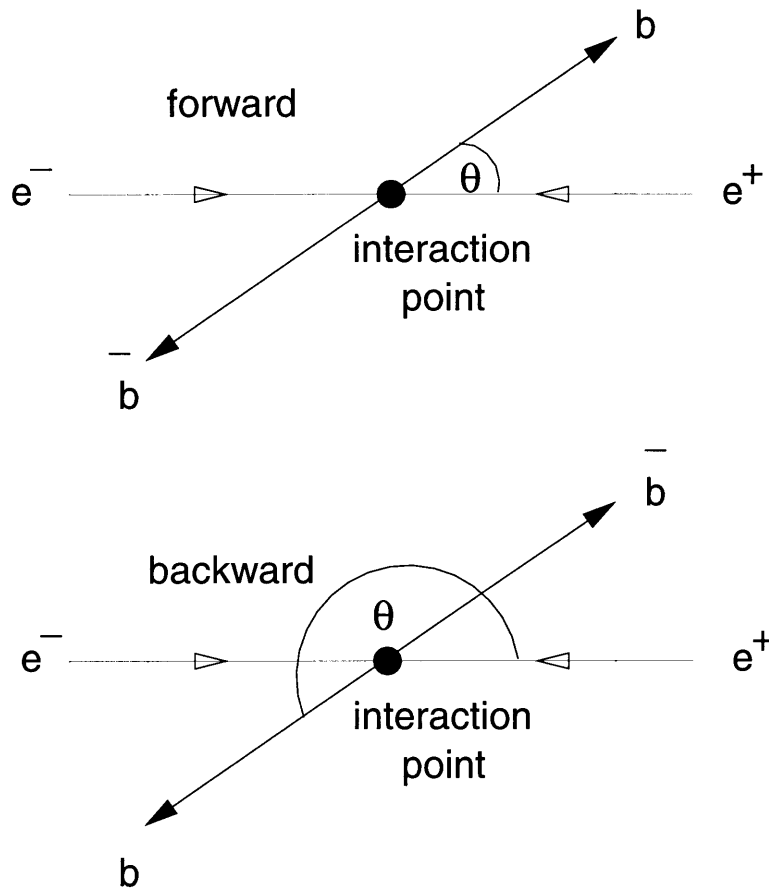
Figure 2: Definition of forward and backward $e^+e^- \to Z \to b\bar{b}$ events. θ is the angle between the directions of the incoming electron and the outgoing negative b-quark.

where θ is the angle between the incoming electron and outgoing negative b-quark (in the centre of mass frame = the lab frame at LEP).

Because of the parity violating nature of the weak interaction, for Z exchange there is a forward-backward asymmetry and the differential cross section is modified to

$$\frac{d\sigma}{d\cos\theta} \propto 1 + \cos^2\theta + \frac{8}{3}A^b_{fb}\cos\theta \tag{15}$$

where the asymmetry, A^b_{FB} , is defined in terms of the cross sections for forward (σ_F) and backward (σ_B) events:

$$A^b_{fb} = \frac{\sigma_F - \sigma_B}{\sigma_F + \sigma_B} \tag{16}$$

In the Standard Model the asymmetry is expressed as the product of two terms, one describing the behaviour of the incoming e^+e^- pair, the other the outgoing $b\bar{b}$ pair:

$$A^b_{FB} = \frac{3}{4}\mathcal{A}_e\mathcal{A}_b \tag{17}$$

where $\mathcal{A}_{e,b}$ are given by

$$\mathcal{A}_e = \frac{2c^e_v c^e_A}{(c^e_v)^2 + (c^e_A)^2} \tag{18}$$

$$\mathcal{A}_b = \frac{2c^b_v c^b_A}{(c^b_v)^2 + (c^b_A)^2} \tag{19}$$

For $\sin^2\theta_w \sim 0.23$ we obtain $A^b_{FB} \sim 0.10$, ie, an expected forward-backward asymmetry of b-quark production of around 10%. Strictly speaking, this asymmetry is a negative number, reflecting the conventional negative charge of the b-quark that has positive baryon number.

Electroweak radiative corrections modify the asymmetry only slightly. The corrections are conventionally absorbed by modifying equation (17) to contain an effective

14

weak mixing angle, $\sin^2 \theta_w^{eff}$. Measurement of the asymmetry is then used to give a precise measurement of $\sin^2 \theta_w^{eff}$ for b-quarks.

A central assumption of the Standard Model is that all quarks and leptons are subject to the same basic electroweak interaction. This assumption can be tested by comparing the value of $\sin^2 \theta_w^{eff}$ obtained from A_{FB}^b with that obtained from different decay channels of the Z. Any discrepancy would imply that there is new physics that causes a breakdown of flavour universality.

The sensitivity of $\sin^2 \theta_w^{eff}$ to the measured asymmetry for a particular fermion anti-fermion pair, $f\bar{f}$, is different depending on the charge of f. At LEP, we may measure the asymmetry for b-quarks, c-quarks and charged leptons, l. The sensitivities are approximately:

$$\Delta(\sin^2 \theta_w^{eff}) \approx -\frac{1}{6}\Delta(A_{FB}^b) \tag{20}$$

$$\Delta(\sin^2 \theta_w^{eff}) \approx -\frac{1}{4}\Delta(A_{FB}^c) \tag{21}$$

$$\Delta(\sin^2 \theta_w^{eff}) \approx -\frac{1}{2}\Delta(A_{FB}^l) \tag{22}$$

Thus, if we assume flavour universality, A_{FB}^b gives the most precise determination of $\sin^2 \theta_w^{eff}$ from an asymmetry measurement.

2.4 Radiative Corrections

The above treatment is only to first order which is not sufficient for comparison to the extremely precise LEP 1 results. For a meaningful comparison it is necessary to take into account higher order diagrams (radiative corrections). These fall into two categories:

- 'QED corrections', which consist of those diagrams with an extra photon added to the Born diagrams either as a real bremsstrahlung photon or virtual photon exchange, figure 3. These are not considered 'interesting' as they are completely calculable and are not influenced by possible new physics. However, they are

15
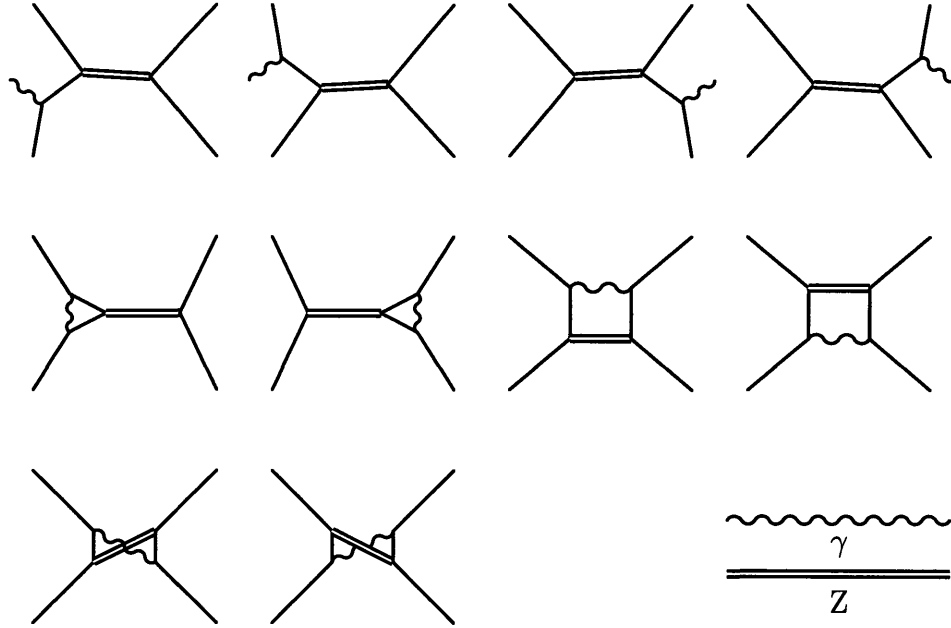
Figure 3: Most important QED corrections to $e^+e^- \to f\bar{f}$ around the Z resonance.

relatively large at LEP energies and must be fully taken into account. QED corrections form a gauge invariant subset. They depend on the details of an particular experiment via the cuts applied to the final state photons. This is further described in in reference [6].

- 'Weak corrections', which collect all other one-loop diagrams. These can be divided into those which involve corrections to the Z propagator, fig 4a and the set of vertex corrections, fig 4b. They are generally independent of experimental cuts.

Weak corrections are a rich area of study. All of the fundamental fermions and bosons can enter into the propagator and vertex corrections with the result that even particles which are too heavy to be produced directly will have an effect on the precise Standard Model prediction for a particular process. By comparing LEP results with these predictions, it is possible to deduce, for example, the mass of the top quark, within the context of the SM, even though it cannot be directly seen at
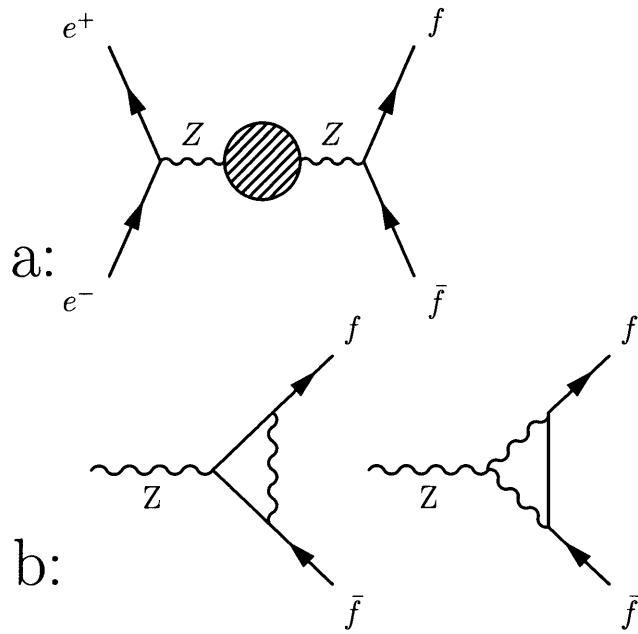
Figure 4: a: Propagator corrections to $e^+e^- \rightarrow Z \rightarrow f\bar{f}$. The shaded area represents a virtual loop of any of the fundamental fermions or bosons. b: Vertex corrections. Here, the straight lines represent fermions, the wiggly lines vector bosons (W or Z). For simplicity, we have not shown diagrams involving virtual Higgs bosons.
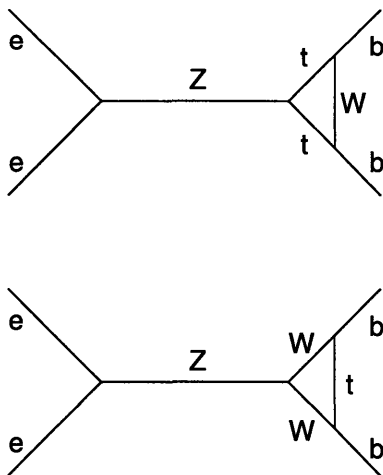
Figure 5: Vertex corrections to $e^+e^- \to Z \to b\bar{b}$

LEP. Comparison with a direct measurement of m_{top} (for example, from the Fermilab Tevatron) tests the validity of the model. As an equivalent test, we can use the Fermilab m_{top} to make precise Standard Model predictions for particular observables which can be compared with direct measurement at LEP.

Even if m_{top} is known, the precision of the Standard Model is still limited by the unknown mass of the Higgs Boson. However, SM predictions are less sensitive to m_{higgs} (logarithmic) than to m_{top} (quadratic). The change in predictions caused by varying m_{higgs} between reasonable limits (60-1000 GeV) is less than the present experimental resolution.

Even to one loop order, the detailed calculation of electroweak radiative corrections is extremely involved and is too lengthy to include here [6]. We can, however, gain an intuitive understanding of the result of dominant radiative corrections in the context of $Z \to b\bar{b}$ decays which are particularly sensitive to top mass effects.

2.5   Corrections to $Z \to b\bar{b}$

Figure 5 shows the most important electroweak vertex corrections to $e^+e^- \to Z \to b\bar{b}$. Notice that corrections featuring the top are dominant. This is because the b and t quarks share the same weak isospin doublet; it is not the case for other final state quarks where transitions involving the top are Cabibbo-suppressed by at least

a factor of 10. By contrast, propagator corrections are the same for any final state fermion.

Let us write the Z decay width to a light quark pair as

$$\Gamma_{q\bar{q}} = \Gamma^0_{q\bar{q}} + \Delta_p \qquad (q \neq b) \tag{23}$$

where $\Gamma^0_{q\bar{q}}$ is the (QED corrected) born-level width and Δ_p is the correction due to the presence of virtual loops in the Z propagator. We can estimate the dependence of Δ_p on m_{top}. The amplitude $\mathcal{M}$ for $Z \to q\bar{q}$ can be written as

$$\mathcal{M} \quad = \qquad A \qquad + \qquad B \tag{24}$$

Since $B \ll A$:

$$\Gamma_{q\bar{q}} \sim \mathcal{M}^2 \sim A^2 + 2AB \tag{25}$$

The m_{top} dependence is due to the presence of two virtual top propagators in B which may be written as

$$B \quad \sim \quad \left(\frac{i(q + m_{top})}{q^2 - m_{top}{}^2} \right)^2 \tag{26}$$

$$\sim \quad \left(\frac{1}{q - m_{top}} \right)^2 \tag{27}$$

where q is the four momentum of the top. Thus, we expect Δ_p to have a quadratic m_{top} dependence. Similar considerations show that Δ_p has a roughly logarithmic dependence on m_{higgs}.

For $Z \to b\bar{b}$, the vertex corrections give an additional top dependence characterised by Δ_v:

$$\Gamma_{b\bar{b}} = \Gamma^0_{b\bar{b}} + \Delta_p + \Delta_v \qquad (28)$$

It turns out [7] that Δ_p and Δ_v largely cancel each other leaving $\Gamma_{b\bar{b}}$ rather insensitive to m_{top}.

The total hadronic width is

$$
\begin{aligned}
\Gamma_{had} &= \sum_{q=1,5} \Gamma_{q\bar{q}} && (29) \\
&= \Gamma^0_{had} + \Delta(m_{top}{}^2) && (30)
\end{aligned}
$$

where Δ is the overall correction due to virtual top loops in the Z propagator for light quark events.

We can now estimate the dependence of R_b on m_{top} :

$$
\begin{aligned}
R_b &= \frac{\Gamma_{b\bar{b}}}{\Gamma_{had}} && (31) \\
&\approx \frac{\Gamma^0_{b\bar{b}}}{\Gamma_{had} + \Delta(m_{top}{}^2)} && (32) \\
&\approx R^0_b(1 - \delta(m_{top}{}^2)) && (33)
\end{aligned}
$$

where R^0_b is the (QED corrected) Born approximation and $\delta = \Delta/\Gamma_{had} \ll 1$. Thus, we expect R_b to have an approximately quadratic dependence on m_{top} through radiative corrections. When taking the equivalent ratio for light quarks, eg, R_d, the top-dependent corrections largely cancel leaving the result rather independent of m_{top}.

The exact dependence of R_b on m_{top} can be calculated with the ZFITTER program [8]. The results are shown in fig 6. Our simple analysis does indeed give the right qualitative behaviour. Also shown is the dependence of R_d on m_{top} where the sensitivity is much smaller, as expected.

Without a direct measurement of m_{top}, this curve can be interpreted as the uncertainty in the Standard Model prediction for R_b. However, in 1994 the CDF col-
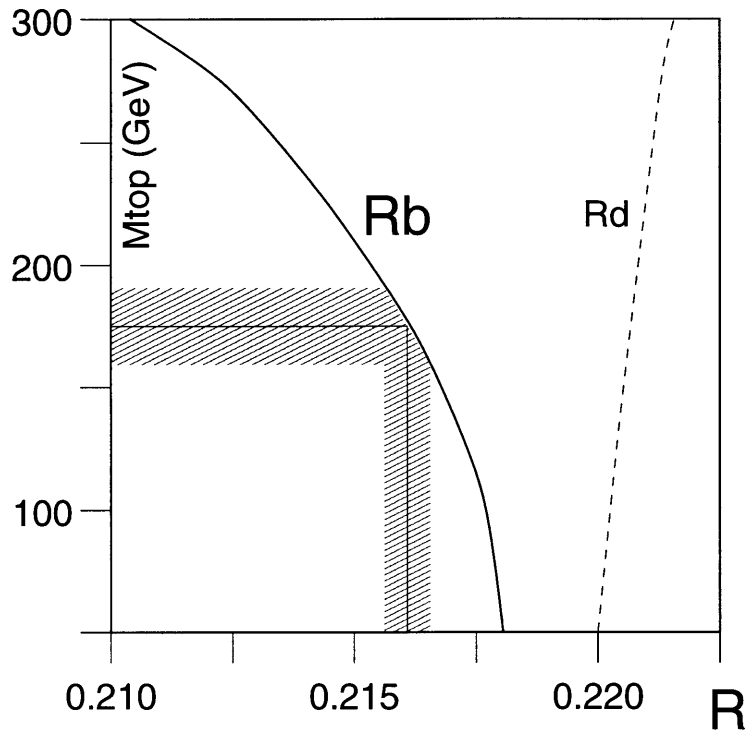
Figure 6: Standard Model predictions for the variation of R_b with the mass of the top quark. The curve is taken from the ZFITTER program [8]. The value of R_b for the first Fermilab measured value of m_{top} = 174±16 GeV [5] is highlighted. The effect on the curves of varying the Higgs mass between 60 and 1000 GeV is smaller than the resolution of the lines. The dashed line shows the equivalent curve for R_d, the corresponding ratio for d quarks.

laboration at the Fermilab Tevatron announced the discovery of the top quark at a mass of 174 ± 16 GeV [5]. The Standard Model prediction can now be read off the graph: $R_b = 0.2155 \pm 0.0004$, where the error is due to the uncertainty in the top mass. This gives us an opportunity to test the Standard Model by comparing precision measurements of R_b to this prediction. A significant discrepancy must be interpreted as a signal for new physics beyond the SM.

In summary, we have defined two important observable quantities in electroweak heavy flavour physics at LEP, R_b and A_{FB}^b , and examined why their measurement constitutes an important test of the Standard Model. In the next section we shall discuss the status of these and other electroweak measurements at LEP when this thesis was proposed (Summer 1995).

3 Z Physics at LEP: Experimental Review

3.1 General Electroweak Measurements

The following Z decays have been studied at LEP 1:

- $e^+e^- \to q\bar{q}(\gamma)$ (hadronic)

- $e^+e^- \to \mu^+\mu^-(\gamma)$ (dimuon)

- $e^+e^- \to \tau^+\tau^-(\gamma)$ (tau)

- $e^+e^- \to e^+e^-(\gamma)$ (bhabha)

- $e^+e^- \to \nu\bar{\nu}(\gamma)$ (invisible)

where (γ) indicates the possible presence of initial or final-state radiation.

The integrated luminosity per year as recorded by the L3 experiment is given in table 1, along with the number of events of each type.

Year	1990/91	1992	1993	1994	1995	total
$\mathcal{L}$ (pb^{-1})	18.4	22.4	31.7	43.2	19.4	135.1
N_E	7	1	3	1	3	
hadronic	416	678	646	1307	311	3358
dimuon	14	21	21	42	9	107
tau	10	15	20	42	7	94
bhabha	16	22	23	43	12	116
total	456	736	710	1434	339	3675

Table 1: Integrated luminosity and number of events (in units of 10^3) recorded by L3 at LEP 1 ($\sqrt{s} \approx m_Z$). In some years the centre of mass energy was scanned over a few energy points within 2-3 GeV of the Z peak. N_E gives the number of energy points per year.

Measured cross sections for each type of decay are used to extract the properties of the Z boson, namely, its mass, total width and hadronic and lepton partial decay widths. Further information on electroweak parameters is gained from measurements of forward-backward asymmetries and of the polarisation of τ leptons. The difference

between the measured total width and the sum of the observable partial widths is attributed to invisible Z decays into neutrinos and leads to a determination of the number of light neutrino families in the context of the Standard Model : $N_\nu = 2.98 \pm 0.06$ [9]. This measurement can be independently performed by analysing the reaction $Z \to \nu\bar{\nu}\gamma$ where the photon is detected: $N_\nu = 3.14 \pm 0.25$ [9] (largely model independent).

Let us define some measurable quantities of interest:

- The mass and total width of the Z boson: m_Z, Γ_Z

- The cross section for e^+e^- annihilation to hadrons at the Z pole: σ_h^0

- The ratios $R_l \equiv \Gamma_{had}/\Gamma_{ll}$ where Γ_{had} is the Z decay width to hadrons and Γ_{ll} the width to $l\bar{l}$ ($l = e, \mu, \tau$). The partial widths are given to first order in the Standard Model by equation(10):

- The lepton forward-backward asymmetries, A_{FB}^l ($l = e, \mu, \tau$) defined in an analogous way to the $b\bar{b}$ asymmetry in the previous chapter.

- The tau polarisation:
$$\mathcal{P}_\tau \equiv \frac{\sigma_R - \sigma_L}{\sigma_R + \sigma_L} \tag{34}$$

where σ_R, σ_L are the τ-pair cross sections with a right and left handed τ^- respectively. The angular distribution of $\mathcal{P}_\tau$ as a function of the angle θ between the e^- and τ^- is given by:

$$\mathcal{P}_\tau(\cos\theta) = -\frac{\mathcal{A}_\tau(1 + \cos^2\theta) + 2\mathcal{A}_e\cos\theta}{1 + \cos^2\theta + 2\mathcal{A}_\tau\mathcal{A}_e\cos\theta} \tag{35}$$

with $\mathcal{A}_\tau$ and $\mathcal{A}_e$ defined as in equation(19).

- The ratios of the partial width of the Z to b and c quarks to its total hadronic width, $R_b \equiv \Gamma_{b\bar{b}}/\Gamma_{had}$ and $R_c \equiv \Gamma_{c\bar{c}}/\Gamma_{had}$

- The forward-backward asymmetries for b and c quark production: A_{FB}^b and A_{FB}^c.

24

These quantities have been measured by all four LEP experiments and averaged [10]. The results, as presented at the 1995 summer conferences [11], are given in table 2 together with the Standard Model predictions evaluated for $m_{top} = 174$ GeV, $m_{higgs} = 300$ GeV.

Parameter	LEP average	Standard Model	Significance
m_Z (GeV)	91.1885 ± 0.0022	input	-
Γ_Z (GeV)	2.4963 ± 0.0032	2.493	+1.03
σ_h^0 (nb)	41.488 ± 0.078	41.48	+0.10
R_e	20.797 ± 0.058	20.736	+1.05
R_μ	20.796 ± 0.043	20.736	+1.40
R_τ	20.813 ± 0.061	20.736	+1.26
A_{FB}^e	0.0157 ± 0.0028	0.0151	+0.21
A_{FB}^μ	0.0163 ± 0.0016	0.0151	+0.75
A_{FB}^τ	0.0206 ± 0.0023	0.0151	+2.39
$\mathcal{A}_\tau$	0.1418 ± 0.0075	0.142	-0.03
R_b	0.2205 ± 0.0016	0.2155	**+3.13**
R_c	0.1540 ± 0.0074	0.171	-2.30
A_{FB}^b	0.0997 ± 0.0031	0.0995	+0.06
A_{FB}^c	0.0729 ± 0.0058	0.071	+0.33

Table 2: LEP electroweak measurements as of summer 1995. Here, significance is defined as (measured value - SM value)/measured error.

The agreement between these exceptionally precise measurements and the Standard Model predictions is remarkable. However, there is one notable exception: R_b is more than three standard deviations from the SM prediction as calculated using the Fermilab measured top mass. This result, taken at face value, represents evidence for new physics.

3.2   Measuring R_b at LEP

Let us look in more detail at the LEP R_b measurements. The key to making such a measurement is to design an efficient and self-calibrating method of distinguishing (*tagging*) $Z \to b\bar{b}$ decays from Z decays to light quarks. High efficiency is desirable because it allows us to tag more events thereby reducing the statistical error on the result. A self-calibrating tag is one where the efficiency can be determined from the

data themselves. This reduces systematic errors by minimising the dependence on Monte Carlo simulation.

There are three principal sources of information available to identify $Z \to b\bar{b}$ decays:

- Lepton Tag: leptons (in practice electrons and muons) coming from semi-leptonic decays of the heavy b quark tend to have higher transverse momentum with respect to the quark direction than corresponding leptons from light quarks.

- Event Shape Tag: because of their high mass, b quarks produced in e^+e^- collisions tend to carry a larger fraction of the beam energy than other quarks. This is apparent in a number of 'event shape' variables such as the momentum and space distribution of final state particles. Such variables are usually combined via a neural network to maximise tagging efficiency.

- Lifetime Tag: Hadrons containing b quarks (generically called 'B') have long lifetimes compared with those of lighter hadrons. This is a consequence of the small magnitude of the Cabibbo Kobayashi Maskawa matrix elements V_{bc} and V_{bu} which dictate the decay rates of the b to lighter quarks[2]. Precise tracking information close to the e^+e^- interaction point allows a tag to be built using charged tracks from B decays.

Of the three methods, the lifetime tag is by far the most efficient, (typically 20-25% of $Z \to b\bar{b}$ events are tagged with a sample purity of $\sim$90%) and will be described in detail in section 6. Different tags are sometimes combined into a single multivariate tag which can increase the tagging efficiency.

The tags can be constructed to be self-calibrating by exploiting the fact that in a $Z \to b\bar{b}$ event, there are two b-quarks that emerge approximately back-to-back which can, in principle, be tagged independently of one another. An event is split into two

---

[2]the CKM matrix is defined in the Appendix, equation(69).

hemispheres[3] which contain, in general, one b-quark each. By counting the number of events in which zero, one or two hemispheres are tagged, the tagging efficiency may be determined from the data themselves. This powerful method is described fully in section 7.1.

The status of LEP measurements of R_b as presented in summer 1995, is given in table 3 and shown graphically in fig 7.

Experiment	Tagging Method	$R_b \times 10^2$	stat. error	sys. error	ref.
ALEPH	lifetime	21.87	0.22	0.25	[13]
ALEPH	event shape	22.80	0.54	0.48	[14]
ALEPH	multivariate	21.62	0.62	0.50	[15]
DELPHI	lifetime	22.10	0.16	0.20	[16]
DELPHI	lepton	21.45	0.89	0.67	[17]
L3	event shape	22.20	0.30	0.70	[18]
L3	lepton	21.87	0.81	0.58	[19]
OPAL	lifetime	21.97	0.14	0.22	[20]
OPAL	lepton	22.50	1.10	0.66	[21]
Standard Model	-	21.55	-	0.04	[8]

Table 3: LEP measurements of R_b as of summer 1995 together with the Standard Model prediction with $m_{top} = 174$ GeV.

The superiority if the lifetime tag is clear from the smaller statistical and systematic errors associated with it. It is also clear that any single measurement of R_b would not be sufficient to claim a significant difference from the Standard Model prediction. It is only when all of the measurements are combined that such a discrepancy becomes apparent. This could be an indication that a systematic effect common to all experiments has not been taken properly into account.

3.3   Possible Physics Interpretations

Let us examine how the R_b discrepancy could be an interpretted in terms of new (ie, non Standard Model) physics. Any scenario that attempts to do this must

---

[3]hemispheres are defined in section 5.2.5
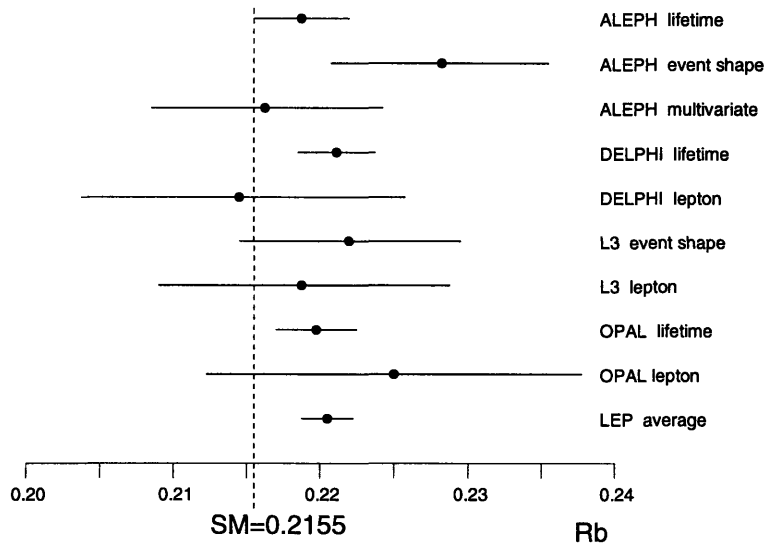
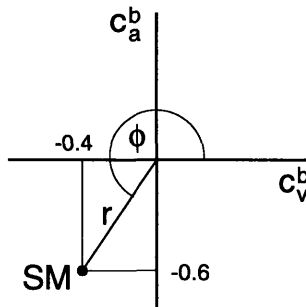Figure 7: Graphical representation of the data in table 3.

Figure 8: Coordinate system with the vector (c_v^b) and axial-vector (c_a^b) Z-b couplings as axes. Each point $(r\phi)$ in the plane represents a different coupling: r is interpretted as the strength, ϕ the degree of parity violation. The point shown is for the Standard Model with $\sin^2 \theta_w = 0.23$

also be consistent with all existing precision tests of the SM, in particular the A_{FB}^b measurement which shows no deviation from the Standard Model prediction.

We can make some general comments about the properties that any new theory must have. From equations (13) and (17) we know that the partial Z decay width to $b\bar{b}$ and the $b\bar{b}$ forward backward asymmetry can be written in terms of vector and axial-vector couplings of the Z to b-quarks:

$$\Gamma_{Z\to b\bar{b}} \propto (c_v^b)^2 + (c_a^b)^2 \tag{36}$$

$$A_{FB}^b \propto \frac{c_v^b c_a^b}{(c_v^b)^2 + (c_a^b)^2} \tag{37}$$

If we represent c_v and c_a as the axes of a 2-dimensional coordinate system, figure 8, and switch to polar coordinates, $r\phi$, we can interpret r as giving the strength of the Z-b coupling, ϕ as a measure of the parity violating nature of the interaction. Re-writing equations (36) and (37) we have

$$\Gamma_{Z\to b\bar{b}} \propto r \tag{38}$$

$$A_{FB}^b \propto \frac{r^2 \sin^2 \phi \cos^2 \phi}{r^2 \sin^2 \phi + r^2 \cos^2 \phi} \tag{39}$$

$$= \sin^2 \phi \cos^2 \phi \tag{40}$$

$$\propto \sin^2 2\phi \tag{41}$$

Any new model that increases $\Gamma_{Z\to b\bar{b}}$ but preserves A_{FB}^b must therefore increase the Z-b coupling strength but leave the parity violation unchanged. It is difficult to construct such models but some possible examples are:

1: $\Gamma_{Z\to b\bar{b}}$ increased via additional production of $b\bar{b}$ pairs from gluons (gluon splitting) in the hadronisation process. This is plausible as quark/gluon hadronisation is not fully computable due to the non-perturbative nature of QCD. Some experimental checks of this hypothesis have been made [22] but do not indicate an effect.

2: Additional radiative corrections to the $Z \to b\bar{b}$ vertex induced by new particles that couple to the b quark. Models with a large parameter space, such as Supersymmetry [23] can be arranged to increase R_b in this way [24].

3: Mixing of the Z with an additional Z' boson with suppressed coupling to leptons (leptophobic) has been proposed [25].

4 The L3 detector at LEP

4.1 The LEP machine

CERN, the European centre for particle physics, located at the Swiss-French border near Geneva, has played a leading role in the understanding of fundamental physics. Since its beginnings in 1954 the laboratory has been instrumental in numerous major discoveries, notably the first observation of weak neutral currents in 1973 [26] and the discovery of the intermediate vector bosons W and Z in 1983 [27]. W and Z had been predicted by electroweak theory and their discovery was heralded as a triumph of the Glashow Weinberg Salam model [1] [2] [3] [4].

The Large Electron Positron collider was built to study the properties of W and Z in detail and thereby make precise tests of the GWS Model as well as to search for indications of new physics. Housed in a specially built 27km circular tunnel, LEP was built in two stages. The first (LEP 1) was completed in 1989 and provided colliding beams of approximately 45 GeV in order to study production and decay of the Z boson. LEP 2 began in 1996 with beams of around 80 GeV that allow the production of W pairs.

A schematic view of LEP is shown in figure 9. The ring consists of eight 2800m bending sections and eight 490m straight sections. Four experiments, ALEPH, DELPHI, L3 and OPAL are located at the center of alternate straight sections. The electron and positron beams are split into four or eight bunches which are timed to cross at the interaction points. In 1995 a new technique was introduced whereby each bunch is replaced by up to four closely-spaced bunchlets. This can increase the luminosity considerably. With four bunches in each beam, the bunch crossing rate seen by each experiment is approximately 44 kHz.

Superconducting quadrupoles either side of each experiment squeeze the beams to give a luminosity of $\sim 10^{31}$ cm^{-2}s^{-1}. Conventional radio frequency cavities in LEP 1 accelerate the beams and compensate for synchrotron radiation losses. For LEP 2 these are complemented by additional superconducting cavities. The beams are injected into LEP at 22 GeV via a complex system of smaller accelerators, figure 10.
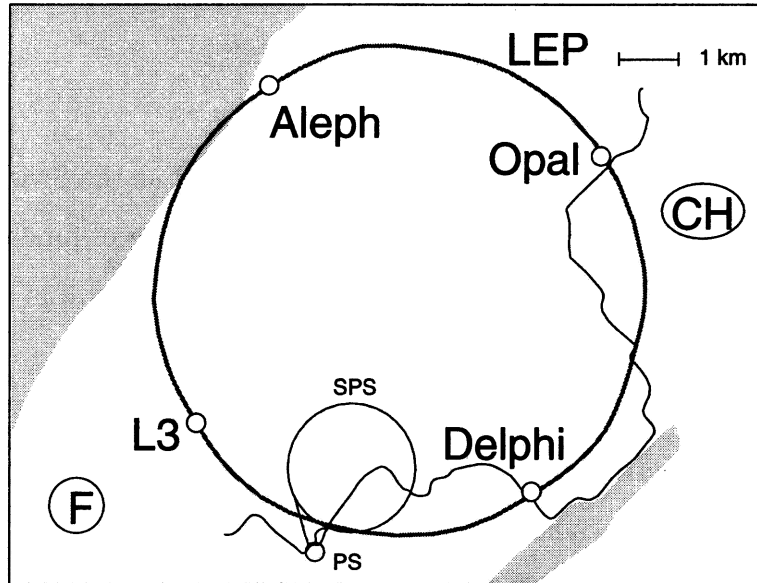
Figure 9: A plan of the CERN site showing the Large Electron Positron collider (LEP), the Super Proton Synchrotron (SPS), Proton Syncrotron (PS), and the four LEP experiments ALEPH, DELPHI, L3 and OPAL.

Once accelerated they can circulate for up to about 20 hours giving several thousand Z decays per fill.

4.2   The L3 detector

L3 is a large detector designed to study e^+e^- collisions at centre of mass energies of up to 200 GeV with an emphasis on the precise energy measurement of electrons, photons, muons and jets. Figure 11 shows a perspective view of the detector. It is located in a specially constructed cavern at interaction point 2 of the LEP ring, 50m under the village of Sergy in the foothills of the Jura mountains in France.

The experiment consists of a number of sub-detectors housed in a 7800 ton solenoid which provides a uniform magnetic field of 0.5 T running along the beam direction. The detectors are supported by a 32 m long, 4.45 m diameter steel tube running concentric to the LEP beam line. This support tube can be adjusted to allow alignment of all sub-detectors relative to the e^+e^- beams. The central section of the support tube houses the *inner detector* elements arranged as *barrel* and *endcap* components
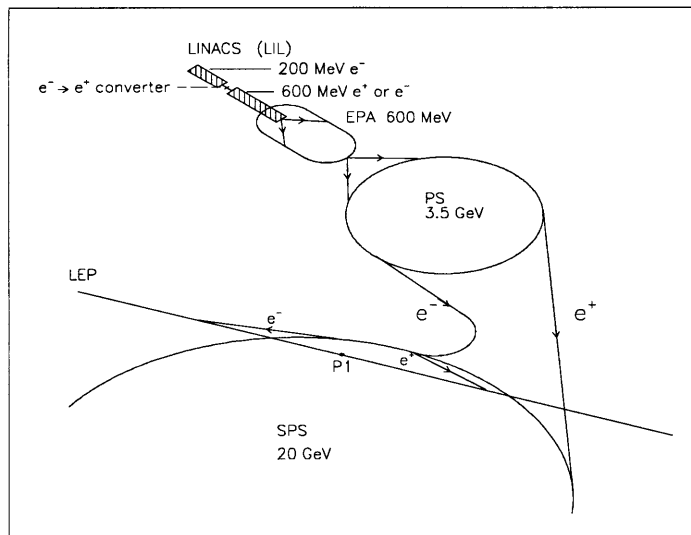
Figure 10: A schematic view of the e^+e^- injection system through linac, accumulator (EPA), Proton Synchrotron (PS), Super Proton Synchrotron (SPS) and into LEP.

around the beam pipe and in the forward/backward directions respectively.

Working out from the e^+e^- interaction point there is a high resolution silicon vertex detector (SMD), a particle tracker (TEC), an electromagnetic calorimeter made from BGO crystals, a uranium hadron calorimeter and a muon filter. Outside the support tube, but within the magnet volume, are three layers of muon chambers arranged concentrically around the beam axis. From 1995 there has been an additional Forward/Backward muon system consisting of chambers arranged on either side of the solenoid endcaps.

Between the hadron and electromagnetic calorimeters there is also a scintillation counter system which is used to provide timing information for trigger purposes, see below. In the far forward and backward regions there are the two halves of the luminosity monitor which count bhabha ($Z \rightarrow e^+e^-$) events to provide a normalisation for cross section measurements.

The design and operation of each sub-detector is outlined below, particularly the inner tracker (SMD+TEC) which is the most important part of L3 for the analyses

33
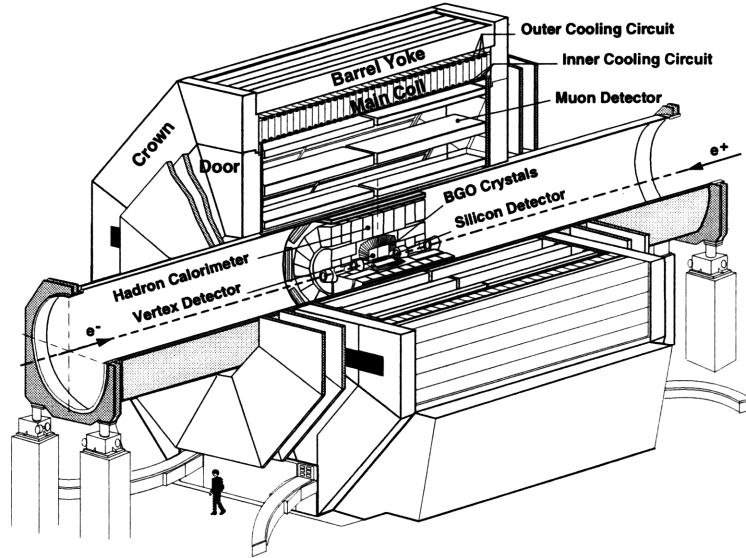
Figure 11: Perspective view of the L3 detector.

presented in this thesis. A more detailed description is the detector can be found in reference [28].

4.2.1   Coordinate System

To facilitate discussion of the detector components, a standard coordinate system has been agreed upon:

- The origin of coordinates is at the nominal e^+e^- interaction point.

- The x axis runs from the origin to the centre of the LEP machine.

- The y axis runs vertically through the origin.

- The z axis runs from the origin in the direction of the incoming electron beam.

- The polar angle, θ, is defined as the angle with respect to the z axis.

- The azimuthal angle, ϕ, is defined at the angle in the xy plane with respect to the x axis.

- The xy plane is also referred to as the $r\phi$ plane where r is the radial distance from the origin.

4.3   Magnet

The magnet is in two parts: the solenoid and the toroid. The solenoid provides a bending field to measure particle momenta transverse to the beam direction. The toroid is a part of the forward/backward muon system described below.

The solenoid consists of a yoke, poles (endcaps) and a coil. The coil is made from aluminium plates welded together to form 168 turns. An active thermal shield on its inside protects the detectors. The magnetic structure is made of soft iron with a 0.5 % carbon content. Each pole is divided into two 340 ton half-doors which can be opened to provide access to the muon chambers. The magnetic field is 0.5 T along the beam line with a high degree of uniformity as determined by a number of Hall probes, magneto-resistors and NMR probes located at various points in the detector volume.

When closed, the doors of each solenoid pole form an octagonally shaped torus. These are magnetised by 36 turns per side of aluminium conductor between the inner and outer radii of the doors. The magnetic field varies from 1.24 T at low radii to 0.8 T at larger radii. This is measured by hall probes and induction loops.

4.4   Muon Spectrometer

The barrel muon detector ($|\cos\theta| < 0.72$) consists of two ferris wheels each of which supports eight independent units or *octants*, figure 12. Each octant consists of five precision (P) chambers: two in the outer layer (MO) with 16 signal wires, two in the middle layer (MM) with 24 signal wires and one inner chamber (MI) with 16 signal wires, figure 13. These together measure track coordinates in the xy plane.

In addition, the top and bottom of each MI and MO chamber are closed with drift chambers designed to measure the z-coordinate (the z-chambers). The barrel muon spectrometer measures the momentum transverse to the beam axis (P_t) of 45 GeV
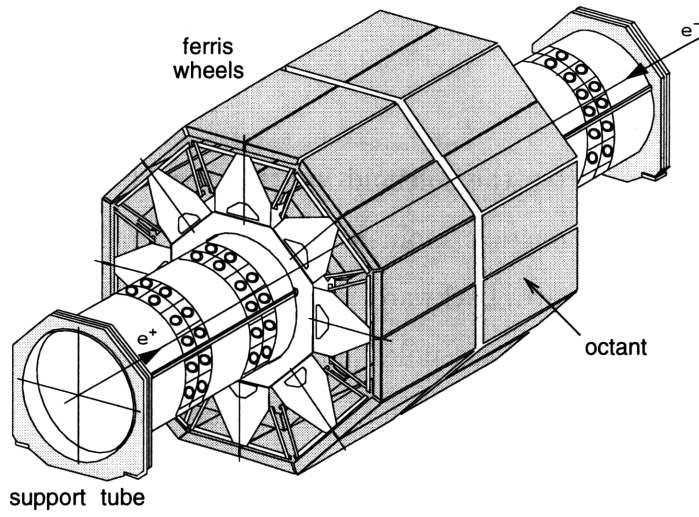
Figure 12: Perspective view of the muon spectrometer.
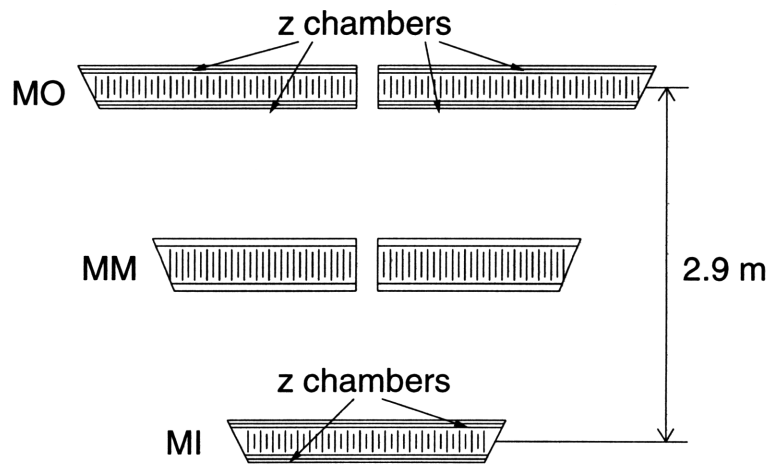
Figure 13: Layout of one muon chamber octant showing the five P chambers MI,MM,MO and six z chambers.
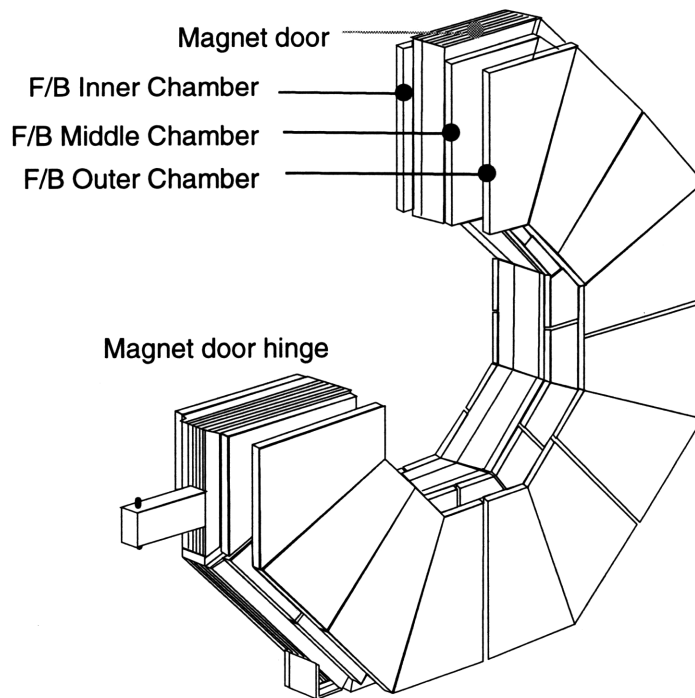
Figure 14: The forward/backward muon system mounted on the magnet door.

muons with a resolution of about 2.5%.

The forward/backward muon system $(0.72 < |\cos\theta| < 0.91)$ is composed of 96 drift chambers mounted in three layers around the toroidal endcap of the magnet. One layer (FI) is located inside the magnet volume and two (FM,FO) are outside, figure 14. The momentum resolution of the FB system for 45 GeV muons ranges from $\sim5\%$ to $\sim30\%$ depending on polar angle.

For triggering, the FM and FO layers are covered by resistive plate chambers (RPCs).

4.5 Hadron Calorimeter

The energy of hadrons emerging from e^+e^- collisions is measured by the total absorption method with both an electromagnetic and hadron calorimeter. The hadron calorimeter is divided into barrel $(|\cos\theta| < 0.82)$ and endcap $(0.82 < |\cos\theta| < 0.99)$
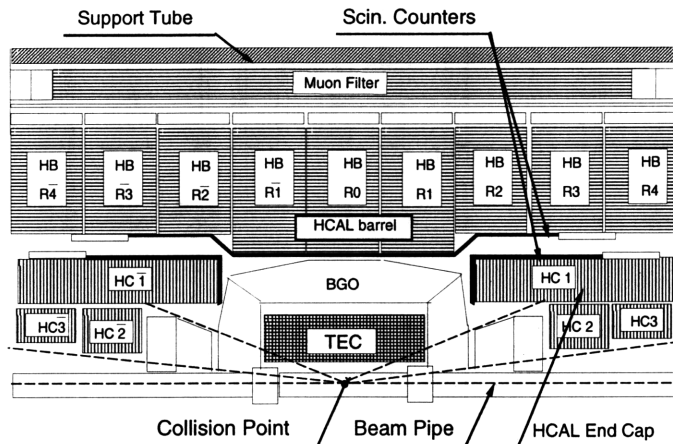
Figure 15: The hadron calorimeter. Note the position of the barrel (HB) and endcap (HC) modules. The position of the scintillation counters is also shown.

regions, figure 15. It is a fine sampling calorimeter made from depleted uranium absorber plates interspersed with ~8000 proportional wire chambers. The total energy of hadronic events from Z decay is measured with a resolution of better than 10%. The fine segmentation of the calorimeters also allows the measurement of the axis of hadronic jets with a resolution of approximately 2.5°.

The HCAL acts as a filter as well as a calorimeter by allowing only non-showering particles to reach the muon detector. It is augmented in this task by the Muon Filter, a sandwich of brass absorber plates and proportional tubes between the HCAL and the support tube, which adds about 1 absorption length to the calorimeter.

4.6   Scintillation Counters

Situated between the hadron and electromagnetic calorimeters are 30 plastic scintillation counters covering the region $|\cos\theta| < 0.83$, figure 15 . (Since 1995 there have also been scintillators in the endcap regions but they are not used in the data analysed for this thesis). The scintillator hit multiplicity is used to distinguish hadronic events from background. The time of flight is also used to reject cosmic background from

dimuon events: muon pairs coming from $Z \to \mu^+ \mu^-$ events hit opposite scintillation counters at the same time whereas a single cosmic muon passing through the $e^+ e^-$ interaction point hits opposite counters with a time difference of 5.8 ns. A time of flight resolution of 460 ps is observed.

4.7 Electromagnetic Calorimeter

The electromagnetic calorimeter, figure 16, is made from $\sim$11000 Bismuth Germanium Oxide (BGO) crystals which act as both the showering and the detecting medium. It has excellent spatial and energy resolution for electrons and photons over a wide range of energies (100 MeV to 100 GeV), figure 17. It is again divided into barrel and endcap regions. Each crystal is a truncated pyramid, about 2×2 cm at the inner end, 3×3 cm at the outer end. They are arranged to all point to the interaction point with a small angular offset to reduce photon leakage. The signal is read out by photo-diodes glued to the back of each crystal.

There is a forward tracking chamber (FTC) located at the end of each endcap, measuring the position and direction of charged particles to 200μm and 10mrad precision respectively.

4.8 Luminosity Monitor

The luminosity monitor (LUMI) consists of two arrays of 304 BGO crystals arranged symmetrically on either side of the interaction point, covering the range $24.93 < \theta < 69.94$ mrad. It is designed to monitor the rate of $Z \to e^+ e^-$ events which are strongly peaked in this region. Since the cross section for these events is well known, the rate can be used to calibrate the luminosity seen by L3 to a precision of around 0.6%.

4.9 Inner Tracker

The inner part of L3 is devoted to precision tracking of charged particles coming from the $e^+ e^-$ interaction point. The bulk of the tracking is done by a Time Expansion Chamber (TEC) which gives up to 62 tracking points in the $r\phi$ plane for r between

39
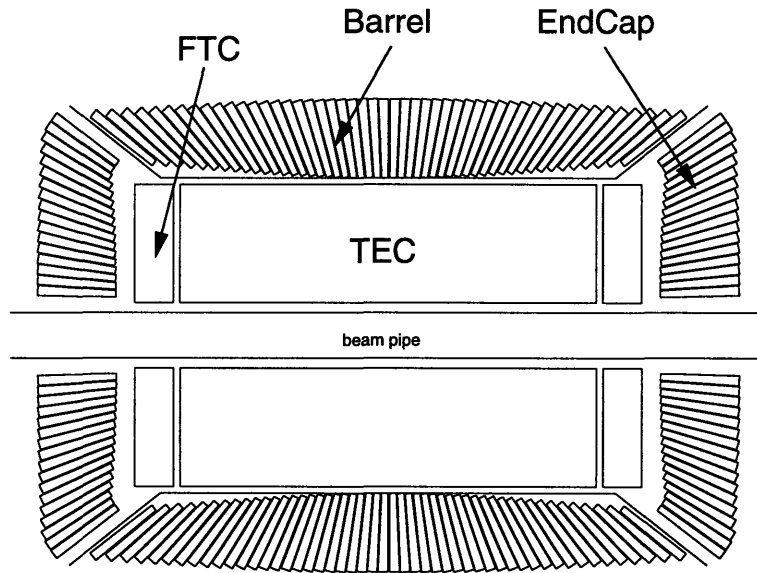
Figure 16: The BGO electromagnetic calorimeter.
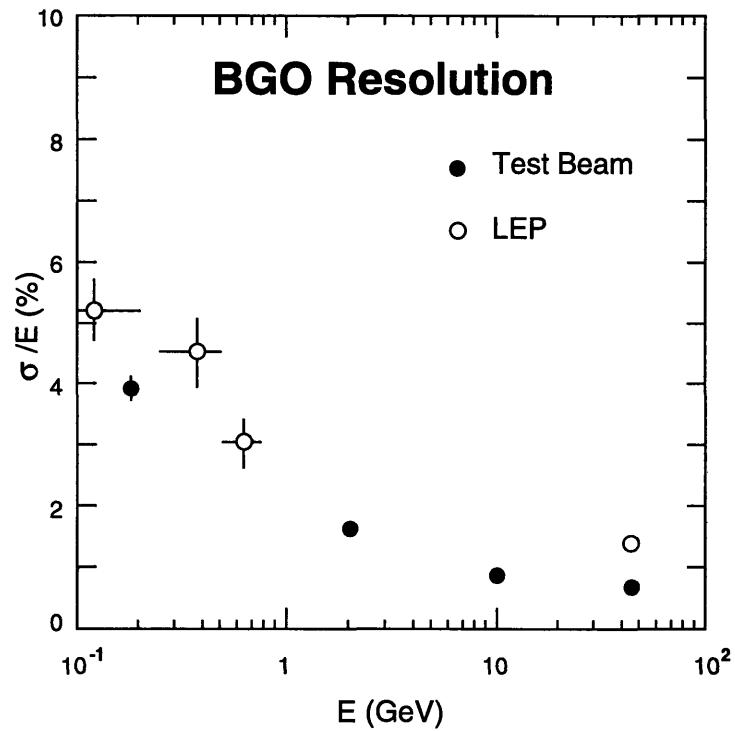
Figure 17: Energy resolution for electrons as a function of their energy as measured in the BGO.
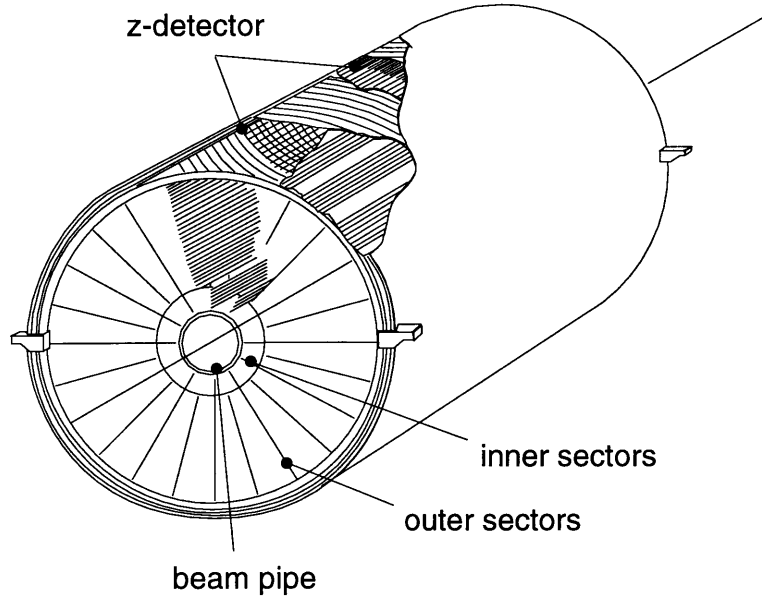
Figure 18: The Time Expansion Chamber. Note the two concentric cylinders around the beam pipe and the division into 24 outer sectors, 12 inner.

10 and 45 cm. This is supplemented by up to three very precise points close to the interaction point, both in the $r\phi$ plane and along the z direction, provided by the two layers of Silicon Microvertex Detector (SMD). Up to four points along z are also given by two layers of proportional chamber just outside the TEC (the z-detector).

The TEC is shown in perspective view in figure 18. It is housed in the volume between two cylinders running concentrically with the beam pipe and divided into an inner and an outer region. The inner region is further divided into 12 equal sectors, the outer into 24. Figure 19 shows the $r\phi$ projection of one inner/two outer sectors. The high amplification region at the sense wire plane is separated from the low field drift region by a grid wire plane. A low diffusion gas mixture is used (CO_2 : iC_2H_4 (80:20)) at a pressure of 1.2 bar. The drift velocity is a low 6 mm/μs and the magnetic deflection (Lorentz) angle is only 2.3°. These design features allow an exceptional single point resolution of $\sim 50\mu m$.

The Silicon Microvertex Detector (SMD), figure 20, is built from 2 layers of double-sided silicon strip detectors, at 6 and 8 cm radially from the interaction region respectively. It is capable of providing $r\phi$ and z coordinate measurements for $|\cos\theta| \leq 0.93$.

41
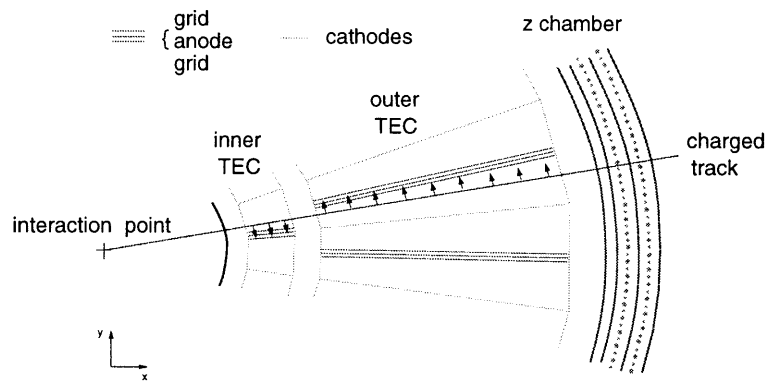
Figure 19: One inner/two outer TEC sectors, $r\phi$ view.
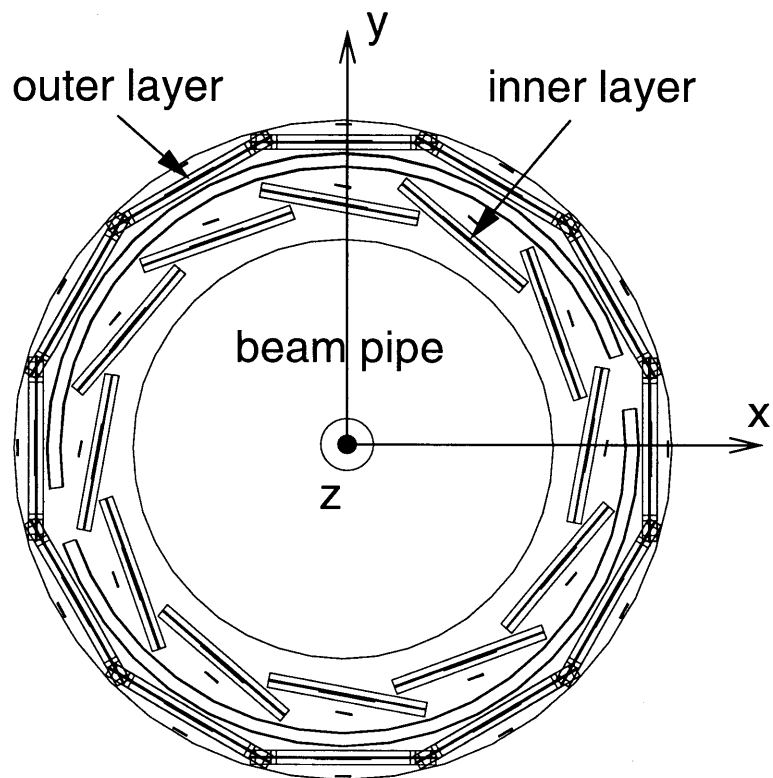
Figure 20: The Silicon Microvertex Detector - end view.
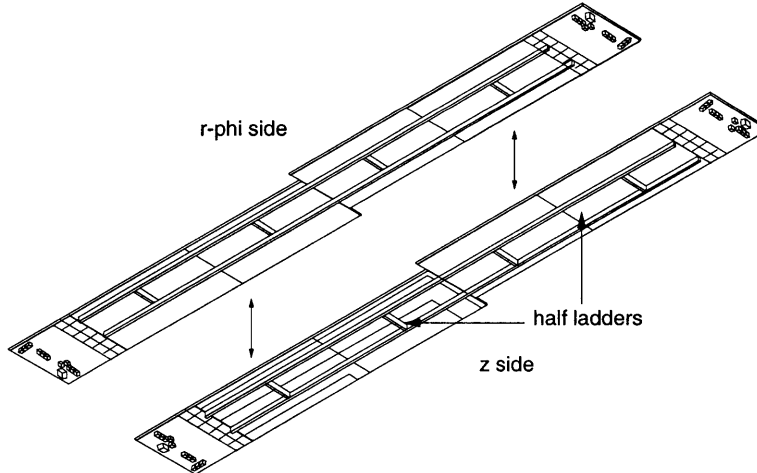
Figure 21: Exploded view of one SMD ladder. Each half ladder consists of two double sided silicon detectors.

The basic detector element is a *ladder*, figure 21. There are in total 24 ladders, each of which is built from two separate half-ladders. Each half ladder is in turn built from 2 electrically and mechanically joined silicon sensors. Each sensor is 70 mm long, 40 mm wide and made from 300 μm thick n-type silicon. On one side (the junction side) there are implantation strips every 25 μm with a readout pitch of 50 μm. These run parallel to the long side of the sensor and give an $r\phi$ coordinate. On the other (ohmic) side, running perpendicular to the junction side strips, are n^+ implantation strips with interspersing p^+ blocking strips designed to interrupt accumulated surface charge. The readout pitch is 150 μm for $|\cos\theta| \leq 0.53$ and 200 μm over the rest of the angular range. This side measures a z coordinate.

The inner ladders are mounted parallel to the beam line with a 5 % overlap as an alignment aid. The outer ladders are mounted at a stereo angle of 2° with respect to the beam line to facilitate pattern recognition, particularly reconstruction of the z coordinate. More information on the construction and operation of the SMD can be found in [29] and [30].

43

5 Event Trigger, Reconstruction and Simulation

In general terms, the output of the detector is just a large number of digital and analogue signals for every beam crossing. In order to turn this data into real physics we have to do two things:

- Trigger: identify the beam crossings in which an interesting event took place and write the data to tape.

- Reconstruct: reduce the raw data to physics quantities of interest, eg, particle energies/trajectories.

For comparison, events are also generated according to the Standard (or any other) Model and passed through a detector simulation.

These tasks are performed by means of dedicated software either written specifically for the L3 experiment or modified from existing CERN code. Triggering and detector monitoring is performed by the online cluster, a VAX system. Reconstruction, simulation and data analysis are performed offline by a number of UNIX workstations.

5.1 Trigger

The trigger uses combined information from each of the sub-detectors to determine whether a beam crossing has produced an e^+e^- collision. Only if the trigger decision is positive are data written to tape. This is necessary because the LEP beam crossing frequency ($\sim$50 kHz) is much greater than the maximum event write rate ($\sim$1 Hz). Ideally, the trigger should reach its decision in time for the next beam crossing. Because of the short time available, not all of the information available from the detector can be used. The trigger should be efficient in that it accepts all e^+e^- interactions with minimum bias. It should also select events with minimum contamination by background processes (detector noise, beam-gas/wall collisions and cosmic muons).

To satisfy these criteria, the L3 trigger is divided into three levels with increasing complexity and a corresponding reduction in speed from level 1 to level 3. Each level consists of a number of separate triggers, corresponding to different event signatures,

44

that are logically ORed to come to the final decision. The trigger is described briefly below and in more detail in reference [31].

5.1.1 Level 1

The level 1 trigger is fast enough to make a decision in the time between beam crossings (11 or 22 μs, depending on the number of bunches (8 or 4) in LEP). If the decision is positive the event is passed to the higher levels. If negative, the event is rejected and the detector readied for the next beam crossing.

There are five components to the trigger:

- Calorimetric trigger: The energy deposited in the BGO and HCAL must exceed certain cuts (eg, total energy $>$ 25 GeV).

- Scintillator trigger: Selects events with high scintillator hit multiplicity ($\geq$ 5).

- Muon trigger: There must be hits in two or three layers of the muon spectrometer on a path pointing to the interaction point.

- TEC trigger: Selects events with at least two charged tracks.

- Luminosity trigger: Looks for back-to-back energy deposition in the luminosity monitor with, eg, total energy $>$ 30 GeV.

The exact values of the cuts can be varied to give a reasonably constant trigger rate for different beam conditions.

The most important components for the analyses presented here are those which select $Z \rightarrow q\bar{q}$ events, ie, the calorimetric, scintillator and TEC triggers.

5.1.2 Level 2 and Level 3 Triggers

The higher level triggers serve to reject background events that have passed level 1. They use more information from the detector and take more time to reach a decision: level 2 correlates information from level 1, level 3 has access to the complete event information allowing more detailed decision making.

The trigger system allows the recording of events with a live time of above 90% and has an efficiency for $Z \rightarrow q\bar{q}$ events of over 99.9%.

5.2 Event Reconstruction

Event reconstruction first takes place within each sub-detector where the raw data are formed into objects such as tracks or calorimetric clusters. These objects are then combined across the detector to characterise the event as a whole.

5.2.1 Muon Spectrometer

Hits in the three layers of the muon spectrometer are combined into *segments* which are further combined to form tracks which are fitted with a helix to give a momentum and charge measurement. The mean energy loss of a minimum ionising particle traversing the inner detector is added to the momentum to give the muon momentum at the interaction point.

5.2.2 HCAL

Charges measured on the wires of the proportional chambers are converted into energies and combined into geometrical clusters by energy-weighting the hits.

5.2.3 ECAL

Signals in the crystal matrix are grouped into energy *bumps*. The position of the bumps are determined by a center of gravity method. Shower-shape analysis is performed to try to separate bumps due to showering particles (electrons and photons) from those due to hadrons.

5.2.4 Track and Vertex Reconstruction

We are interested in identifying $Z \rightarrow b\bar{b}$ decays via the relatively long lifetime of B hadrons. This requires very precise reconstruction of charged tracks close to the e^+e^- interaction point. The point of e^+e^- annihilation is different for each event within a
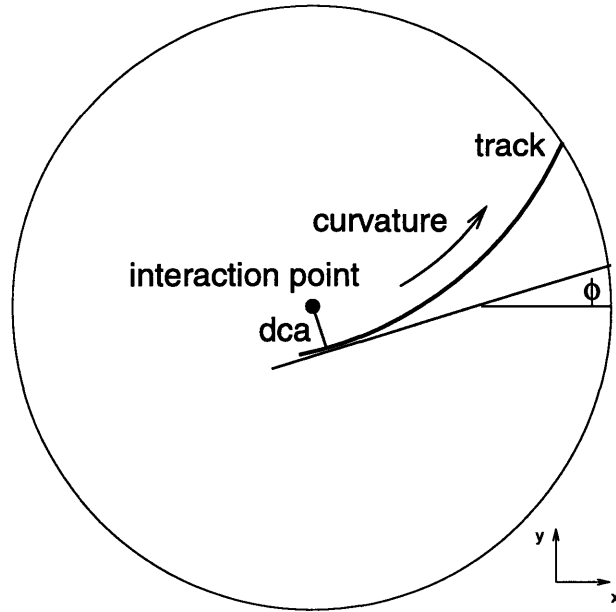
Figure 22: The parameters used to describe a reconstructed charged track.

beam spot of r.m.s. dimensions approximately 110 μm $\times$ 20 μm$\times$10 mm in x, y and z respectively. To identify the e^+e^- interaction point more precisely than this for each event, we use the tracks themselves to estimate a point of common origin, called the primary vertex. Track parameters are then re-defined with respect to this point.

The procedure is:

1. Use TEC and SMD to determine a set of parameters that define each track in an event. These are taken to be the curvature, distance of closest approach (dca) to a nominal interaction point, and the azimuthal angle (ϕ) at the point of closest approach, together with a covariance matrix, see figure 22.

2. Determine the position of the LEP luminous region (beam spot) using tracks from many consecutive events.

3. Use the reconstructed tracks in an event together with the beam spot position to determine the primary vertex for that event.

4. Re-define track parameters with respect to the reconstructed primary vertex.

47

We confine ourselves to reconstruction of tracks and vertices in $r\phi$ only. This is for two reasons: there is more tracking information available in L3 in the $r\phi$ plane than along the z direction and the dimensions of the beam spot mean that the e^+e^- interaction point is very difficult to reconstruct along z.

The inner tracker of L3 reconstructs particle trajectories from hits in the two layers of double sided silicon of the SMD, up to 62 measurements in the TEC and two measurements in the Z chamber. These measurements are combined to determine the three parameters characterising a track in the $r\phi$ plane. The most important parameters for the analyses presented here are the dca and its error, σ_{dca}. Small biases in the dca itself are removed by re-calibrating the mean dca value as a function of the azimuthal angle of the track and as a function of the track position inside TEC sectors. The dca error is re-calibrated using tracks with a high probability to come from the primary vertex. For these, the width of the dca distribution for tracks with high momentum, where multiple scattering is negligible, is used to determine a factor that multiplies the calculated dca error from the track fit. The factor is found to be close to 1, in agreement with an analysis performed using high momentum tracks from $e^+e^- \rightarrow e^+e^-$, $\mu^+\mu^-$, and $\tau^+\tau^-$. In addition, the contribution from multiple scattering, not included in the error calculated in the track fit, is estimated from the dependence of the distribution's width on transverse momentum. It is found that the additional multiple scattering error is 110μm $/(p_\perp\sqrt{\sin\theta})$ for tracks with a hit in the inner SMD layer, 200μm $/(p_\perp\sqrt{\sin\theta})$ for tracks without such a hit, where $p_\perp$ is the track momentum transverse to the beam axis measured in GeV.

The position of the LEP luminous region inside L3 is reconstructed using tracks collected from hadronic events. The position and its error is averaged over 200 events, in order to closely follow drifts of the beam position. The result, called the 200-event-vertex, is the starting point for the reconstruction of the primary vertex in each event, weighted by its error corresponding to the r.m.s. width of the beam spot in the x and y directions.

For the reconstruction of primary vertices, tracks are selected using loose cuts on the track quality. These are:

- The track fit should be performed with at least 20 hits in the TEC and at least one hit in the inner layer of the SMD.

- The distance of closest approach (dca) to the nominal interaction point, initially taken to be the 200-event-vertex, should be less than 1 mm.

- The significance of the dca, defined by the ratio of the dca to its total error, should be less than five.

- The transverse momentum ($p_\perp$) of the track should be greater than 150 MeV.

The procedure uses an iterative method which starts from the 200-event-vertex as an initial estimate of the primary vertex position. At each step of the iteration, the vertex is calculated with all the tracks selected for that step under the hypothesis that they all have their origin at a single point. If the χ^2 probability of the vertex is less than 0.05, the track with the largest contribution to χ^2 is removed and the vertex is recalculated with the remaining tracks. This procedure is repeated until the χ^2 probability of the vertex is at least 0.05 or only three tracks are left. In every step, the 200-event-vertex is used as a constraint. With this procedure, a primary vertex is reconstructed in all selected events, see below. The average uncertainty on the primary vertex position in the x direction is 42 μm for light-quark events and 77 μm for b-events. It depends on the azimuthal angle of the event thrust and on the number of tracks retained for its determination. The degraded resolution for b-events is due to the unavoidable inclusion of b-decay tracks in the vertex determination. The uncertainty in the y direction is dominated by the small vertical width of the beam spot (< 20 μm).

5.2.5 Reconstruction Across L3

Tracks in the muon spectrometer are linked with HCAL clusters, BGO bumps, TEC tracks and SMD hits to form muon candidates. Remaining calorimetric objects are then combined to form Smallest Resolvable Clusters (SRCs) which are regions of calorimetric activity characterised by vectors $\vec{P_i}$ whose magnitude is the total SRC
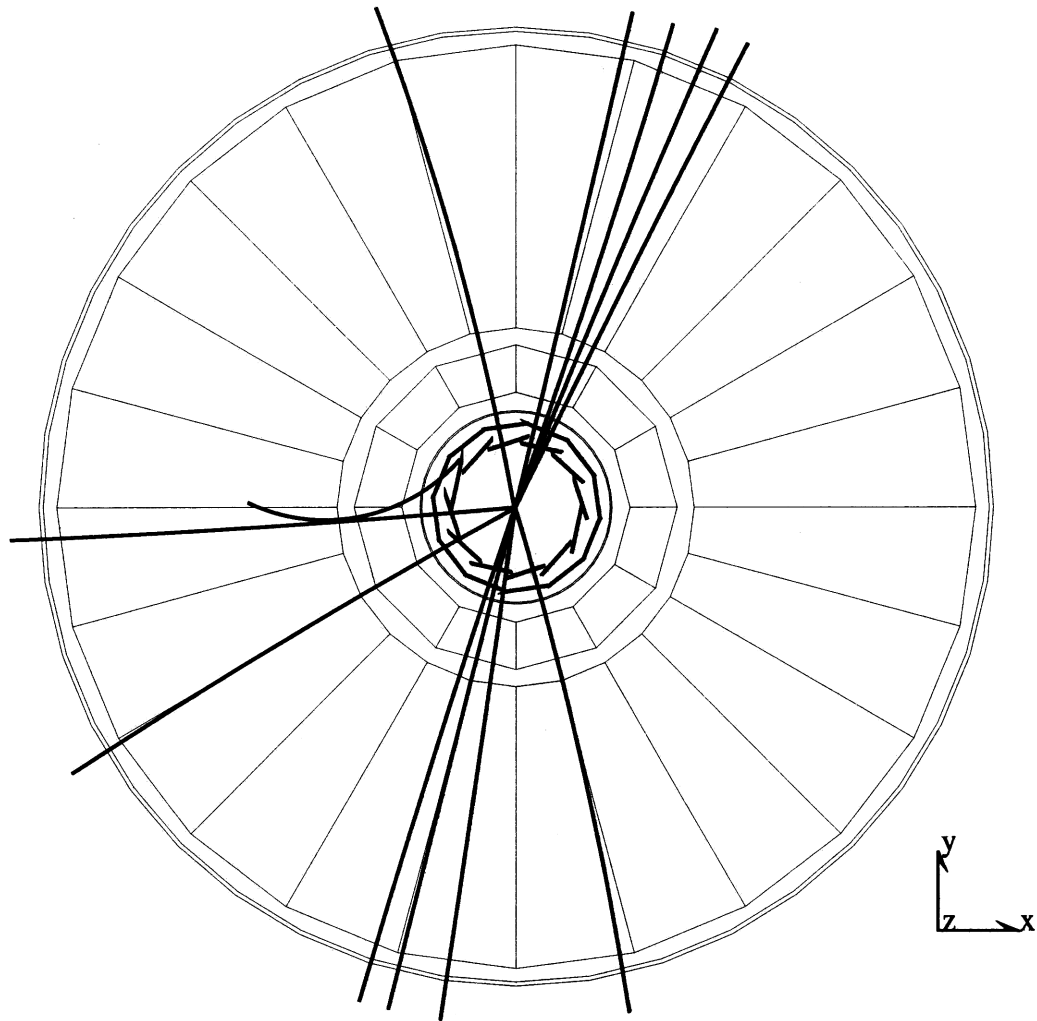
Transverse Imbalance :	.0342	Longitudinal Imbalance :	-.0086
Thrust : .9561	Major : .1237		Minor : .0571
Event DAQ Time :	*940626 133721*		

Figure 23: x-y view of a typical hadronic event as reconstructed in the L3 detector. Only the tracking detector elements (TEC+SMD) are shown. Some general information about the event, is also given.

energy and whose direction is given by the energy weighted sum of the positions of the SRC components. SRCs and muons are combined into jets using the LUCLUS [33] algorithm.

A *thrust* axis, $\vec{n}_T$, is defined for each event by maximising

$$S = \sum_i |\vec{P}_i \cdot \vec{n}_T| \tag{42}$$

The event thrust is defined as

$$T = \frac{\sum_i |\vec{P}_i \cdot \vec{n}_T|}{\sum_i \vec{P}_i} \tag{43}$$

For isotropic events $T = 0.5$; for events where the final state particles are collinear $T = 1$ and $\vec{n}_T$ indicates the line of flight of the particles. Most events lie between these two extremes.

We can also define transverse and longitudinal energy imbalances:

$$\text{Transverse Imbalance} = \frac{\sum \vec{E}_\perp}{\sum E} \tag{44}$$

$$\text{Longitudinal Imbalance} = \frac{\sum \vec{E}_\parallel}{\sum E} \tag{45}$$

where $\vec{E}_\perp$ and $\vec{E}_\parallel$ are the measured SRC energies transverse and longitudinal to the beam direction respectively. We can also define two hemispheres per event by a plane through the origin and perpendicular to the thrust axis; in an $e^+e^- \rightarrow q\bar{q}$ event, the quark and antiquark generally emerge into opposite hemispheres.

Figure 23 shows a typical hadronic event as reconstructed in the L3 detector, shown in xy projection along with some general event information. Here only the central tracking elements (TEC+SMD) are shown.

5.3 Hadronic Event Selection

The analyses presented in this thesis require a high purity sample of $Z \to q\bar{q}$ decays. Such events are selected from the background of other Z decays and non-Z events using information from the electromagnetic and hadron calorimeters. To be selected, events must pass the following cuts [32]:

- $0.5 < E_{vis}/\sqrt{s} < 1.5$ where E_{vis} is the the total calorimetric energy observed in the detector and $\sqrt{s}$ is the e^+e^- centre of mass energy.

- Longitudinal Imbalance < 0.6.

- Transverse Imbalance < 0.5.

- There must be at least 14 SRCs in the barrel region, at least 18 in the endcap.

These cuts select $Z \to q\bar{q}$ events with an efficiency of over 99% with a background contamination of less than 0.15%.

In addition, some other cuts are imposed in order to have an event sample well suited to b-tagging:

- The event must not be a part of a 'bad run' which are defined at the time of data taking as runs in which a part of the detector was not working correctly (the most common fault is an over-current in a sub-detector leading to a sub-nominal high voltage setting). For our purposes, the detector elements that must be fully operational are SMD+TEC+ECAL+HCAL.

- The thrust of the event must lie in the barrel region of the detector: $|\cos\theta_{\text{thrust}}| <$ 0.7. This ensures that the majority of tracks pass through the SMD active region.

- There must be at least four reconstructed tracks.

- There must be at least two reconstructed jets.

- A primary vertex must be found.

These selection criteria are applied to the data collected by L3 in 1994 and 1995, when the SMD was fully installed and operational. The integrated luminosity at the Z peak delivered by LEP in these years was 43.2 and 19.4 pb^{-1} respectively. The reduction of these events to those used in the final analyses is shown in table 4. A total of 924k events pass all cuts corresponding to an integrated luminosity of $\sim$31 pb^{-1}.

requirement	no. of events $/10^3$
hadronic selection	1721
good runs	1647
barrel region	1032
$\geq$ 4 tracks	952
$\geq$ 2 jets	924
Primary Vertex	924

Table 4: Numbers of events passing the selection cuts. Each figure is the number of events passing that and all previous cuts.

5.4 Simulation

Computer simulation is an essential part of the data analysis that facilitates the understanding of the physics, detector response and systematic errors at a level which makes precision measurements possible. Because of the non-analytical nature of many of the modelled processes, in particular the fragmentation of quarks and gluons into hadrons, the simulation is performed using Monte Carlo techniques and is known simply as 'Monte Carlo' throughout the remainder of this thesis.

The simulation takes place in two stages:

Event generation where events are created according to a physical model and the results are stored as sets of particle types and energy-momentum four vectors. For the analyses presented here, event generation is performed by the JETSET [33] program that generates $e^+e^- \rightarrow f\bar{f}$ events according to Standard Model processes and performs subsequent decays using experimental data on lifetimes and branching ratios as input. Quark-gluon fragmentation is simulated using a string model.

Detector simulation where the generated particles are propagated through a detailed representation of the detector including the response of each active detector element and the effects of showering in the detector materials. This is performed by a specialised version of GEANT3 [34]. The output is a number of digitised events that can be reconstructed using exactly the same procedure as for the real data. To achieve high precision physics results, the detector simulation is accurate to typically 10-100 μm and 10-1000 KeV. In addition, the calorimeter responses are tuned with the help of test beam data [35]. Detector imperfections (dead cells, noisy wires etc) vary with time and must be properly simulated. This is done during reconstruction when information from the online database of the detector status is used.

In principle, the number of simulated events should be much larger than the number of events in the real data sample. However, event simulation is very time consuming, taking some minutes of CPU time for each event. Consequently, a limited number of events are generated, typically 4-5 times the number of real data events used for a particular analysis. This represents the point where the error due to limited Monte Carlo statistics becomes a small fraction of the other errors on the measured quantity of interest. For the analyses presented here, the Monte Carlo sample is about 4.7 million fully simulated $e^+e^- \rightarrow q\bar{q}$ events.

6 Lifetime Tagging of Heavy Quarks

The lifetime information used to tag $Z \rightarrow b\bar{b}$ can be accessed in two principal ways. One method exploits the large impact parameters, with respect to the primary vertex, of tracks coming from B hadron decays (impact parameter tag). The other looks for secondary vertices that are significantly displaced from the primary vertex (decay length tag). The two methods are illustrated in figure 24. The impact parameter tag is described in detail below and is used as the primary b-tag in the remainder of this thesis.
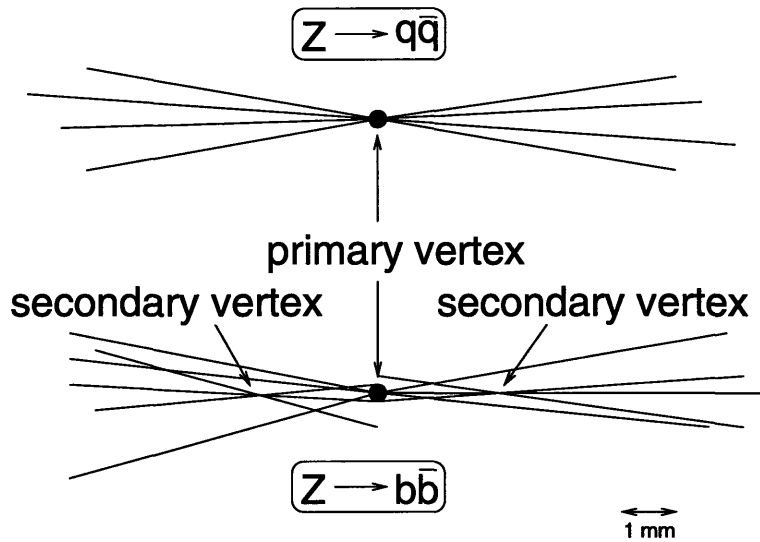
Figure 24: Schematic representations of $Z \rightarrow q\bar{q}$ and $Z \rightarrow b\bar{b}$ decays close to the e^+e^- interaction point, projected onto a plane perpendicular to the beam axis. Here q is any light quark (udsc). Note how the long lifetime ($\sim$ ps) of hadrons containing b quarks leads to tracks with large (up to about 1 mm) impact parameters with respect to the interaction point and allows the reconstruction of secondary vertices significantly removed (a few mm) from the primary.

6.1 Impact Parameter Tag

The aim of the tag is to construct a discriminating variable D which is related to the likelihood that a particular set of tracks is consistent with having the primary vertex as a common origin. The sensitive single track quantity used for constructing
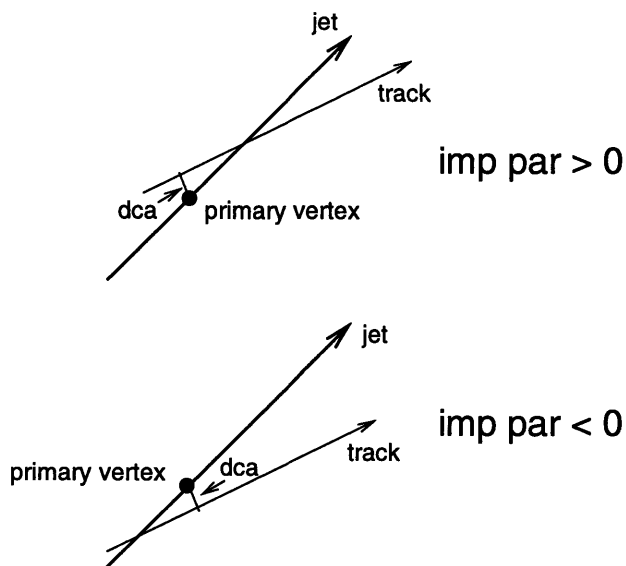
Figure 25: The impact parameter sign convention.

D is the impact parameter, defined as the distance of closest approach (dca), in $r\phi$, of the track to the primary vertex with a sign that is positive if the track intersects the direction of the accompanying jet in the direction of the jet's total momentum, negative if it intersects opposite to that direction, see figure 25. Tracks coming from the decay of long lived particles tend to have positive impact parameters; those with negative impact parameter are assumed to originate from the primary vertex and give a measure of the tracking resolution.

In addition, the impact parameter uncertainty is determined from the error in the track fit, the error in the position of the primary vertex and a contribution due to the multiple scattering of the particle through the material of the detector. These are determined according to the procedure described in section 5.2.4 and added in quadrature. The ratio of the impact parameter and its error defines the significance s.

The discriminant variable is constructed on the basis of a resolution function, $R(x)$, which describes the probability that a track which comes from the primary vertex is measured to have an apparent impact parameter significance $|x|$. Since tracks with negative impact parameters are assumed to originate from the primary

vertex, we can use their distribution to determine $R(x)$ from the data sample itself: $R(x)$ is taken to be the normalised distribution of the absolute value of the impact parameter for negative tracks.

The probability P for a track with impact parameter significance s to come from the primary vertex is given by

$$P(s) = \frac{\int_{|s|}^{\infty} R(x)dx}{\int_{0}^{\infty} R(x)dx} \tag{46}$$

P is uniformly distributed between 0 and 1 for tracks which are consistent, within the resolution, with the primary vertex. For tracks with lifetime information, P is peaked at 0.

The likelihood $L(n)$ that a set of n tracks is consistent with having a single primary vertex as common origin is then

$$L(n) = \prod_{i=1}^{n} P(s_i) \sum_{j=0}^{n-1} \frac{(-\ln \prod_{i=1}^{n} P(s_i))^j}{j!} \tag{47}$$

In principle, $\prod_{i=1}^{n} P(s_i)$, ie, the product of probabilities of all tracks in the selected set, contains all of the lifetime information available. However, this quantity depends strongly on the number of tracks, n, included in the product. This has a diluting effect on our ability to discriminate between events with and without lifetime information. The more complicated variable $L(n)$ is constructed to be flat between 0 and 1 for the case of no lifetime information, regardless of n. When lifetime information is present, $L(n)$ is always close to zero.

The discriminant variable is then defined as

$$D = -\log_{10} L(n) \tag{48}$$

such that a large D indicates lifetime information in the track sample whereas a small value of D indicates that all the tracks are consistent with a single primary vertex.

$L(n)$ can be determined for any set of n tracks. The most useful sets are:

- All tracks in an event. This leads to an *event discriminant.*

- All tracks in a hemisphere as defined in section 5.2.5 (*hemisphere discriminant*).

- All tracks associated with a jet (*jet discriminant*).

The choice of discriminant depends on the physics goals of a particular analysis. We will be particularly concerned with the event and hemisphere discriminants.

Tracks are selected according to the following quality criteria which are optimised to give the highest tagging efficiency:

- The effective track length as reconstructed in the TEC should correspond to at least 40 radial wire distances, with at least 30 hits included in the track fit.

- The distance of closest approach (dca) to the primary vertex should be less than 1.5 mm, or 3 mm for tracks with no SMD information.

- The reconstructed track momentum transverse to the beam axis should exceed 0.5 GeV.

- The angular separation of the track from the anode and cathode planes of the TEC, where the resolution is degraded, should exceed $\delta\phi = 11$ mrad.

- If a track comprises no hits from the SMD, at least 2 hits from the inner TEC should be used in the track fit.

Figure 26 shows the impact parameter significance distribution for all selected tracks. Data is compared with the Monte Carlo expectation with the Standard Model value for $R_b = 0.2155$. In order to achieve the excellent agreement shown, the Monte Carlo tracks were smeared slightly with respect to the output from the standard detector simulation. The effect of this smearing on the final physics results will be addressed in section 7.2.1.

Tracks are classified into six categories according to the number of associated SMD hits, table 5. We expect increasing impact parameter resolution for categories 1→6. This is seen in the decreasing r.m.s. of the track impact parameter distributions.

The proportion of tracks in each category is shown for data and Monte Carlo in figure 27. For a perfect detector we expect each track to have associated with it one

track category	inner SMD hits	outer SMD hits	IP r.m.s. (mm)
1	0	0	0.588
2	0	1	0.295
3	1	0	0.225
4	1	1	0.208
5	2	0	0.207
6	2	1	0.189

Table 5: Definition of track categories according to the number of associated hits in the inner and outer layers of the SMD. The r.m.s. of the distribution of track impact parameters for each category is also shown.

hit in both the inner and outer SMD, with 5% of tracks having two hits in the inner due to the geometrical overlap (ie, 95% in category 4, 5% in category 6). Because of the finite SMD efficiency, a large number of tracks are moved to lower categories and a degradation from the ideal track quality is seen. However, more than 50% of the tracks have at least one SMD hit which, as is apparent from the r.m.s. widths in table 5, represents a significant improvement over the use of TEC alone.

Separate resolution functions $R(x)$ are constructed for each track category by fitting the negative side of the ip significance distribution for those tracks. The r.m.s. width of the significance in each class is compatible with one, but the distributions have substantial tails. Therefore, $R(x)$ is constructed as a sum of two Gaussian functions and an exponential tail.

The resolution functions thus determined are used to calculate track probabilities $P(s)$. The distribution of $P(s)$ is shown in Figure 28. The agreement between data and Monte Carlo is good. Also shown is the track probability distribution for Z $\rightarrow$ uds, c and b events taken from the Monte Carlo. Note how the long lifetime of hadrons containing b quarks leads to a large peak at zero probability. The smaller peak for c events is due to the shorter, but still observable lifetime of c-hadrons. The uds distribution is almost flat indicating that all tracks are consistent, within the resolution, with a common primary vertex.

The distribution of the hemisphere discriminant $D(n)$ in data and Monte Carlo is shown in Figure 29, together with the MC components in terms of primary quark

59
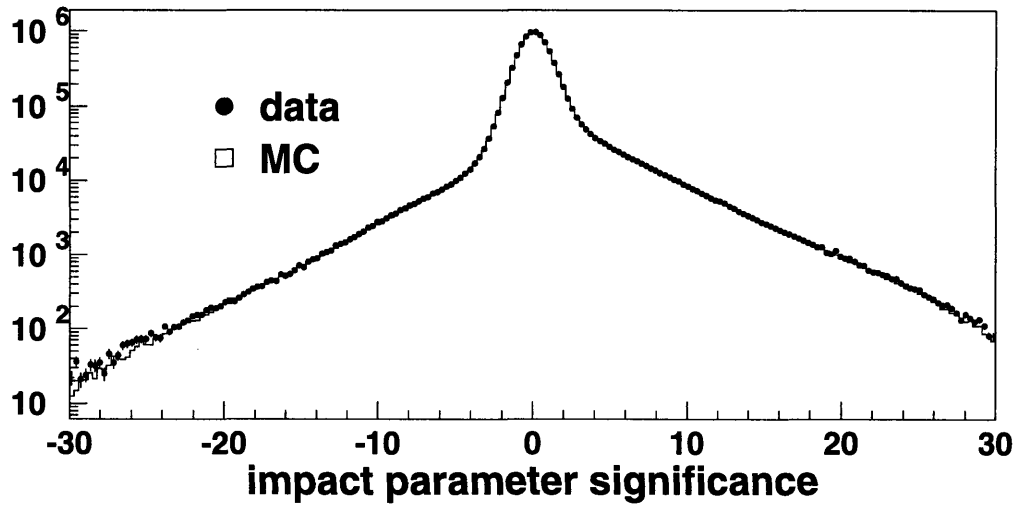
Figure 26: Impact parameter significance distribution for all tracks in data and Monte Carlo. $R_b = 0.2155$ was used for the MC.
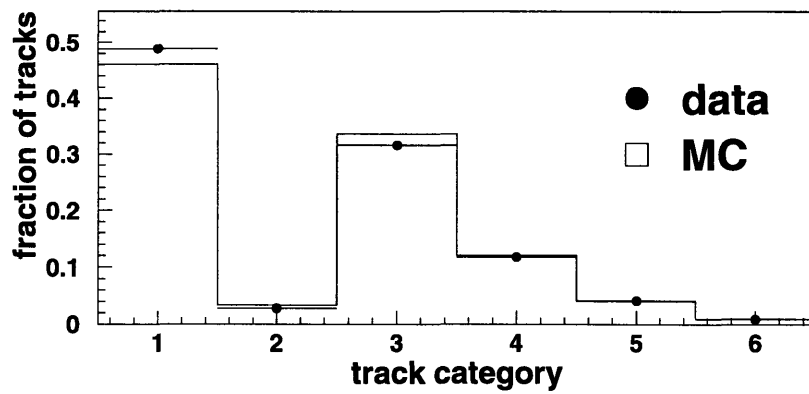
Figure 27: Track category distribution in data and Monte Carlo. The categories are described in table 5.
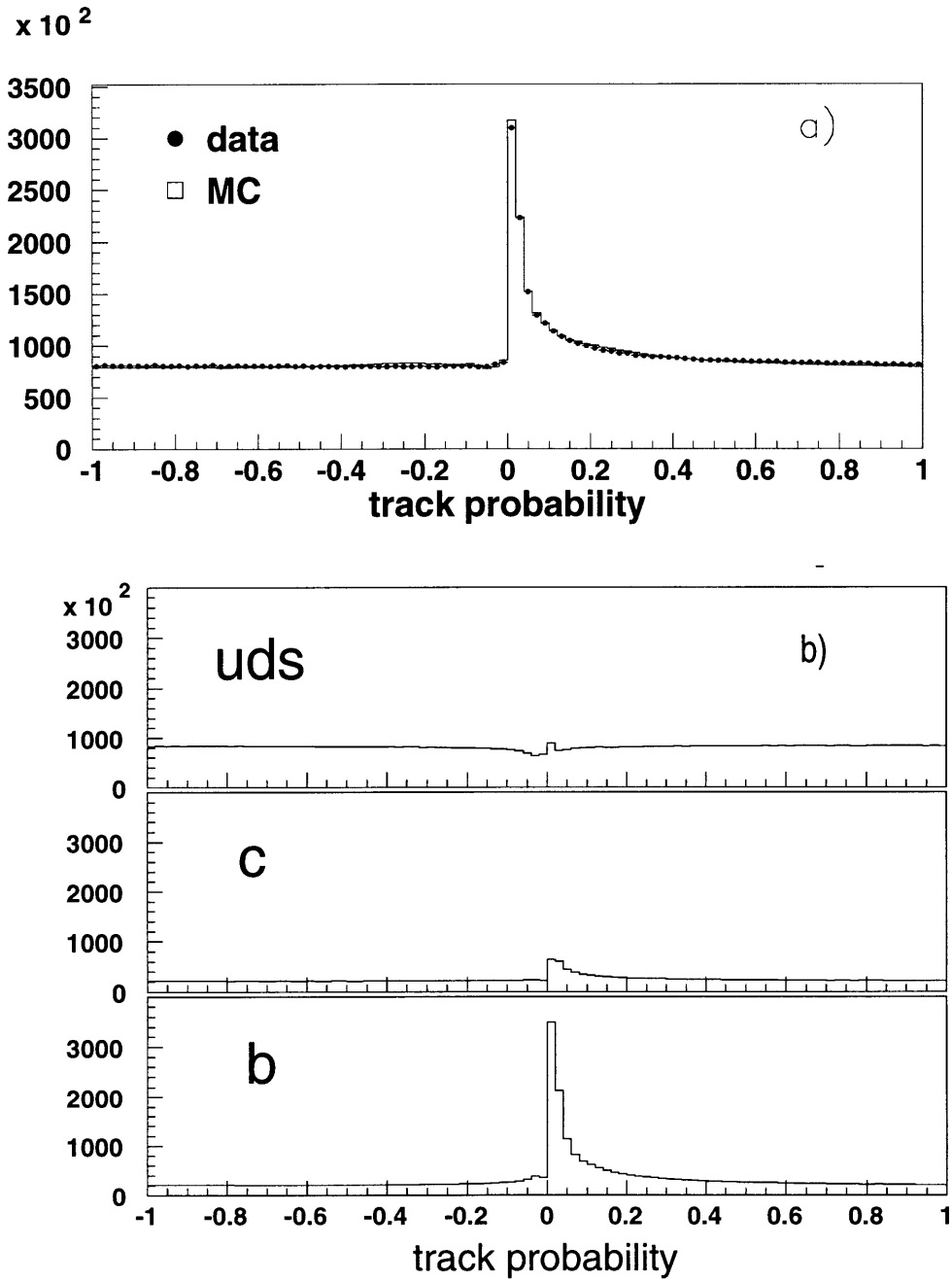
Figure 28: Track probability distribution. Tracks with negative significance are shown with a negative probability. The peak at zero probability is due to tracks with lifetime information. a) compares data with Monte Carlo, b) shows the distribution for samples of uds, c and b events taken from MC.

flavours. The agreement is good for the bulk as well as the tail of the distribution and the b-tagging power of the discriminant is clearly exhibited.

As an illustration, we look at two events, close to the interaction point as reconstructed using TEC and SMD information, figure 30. Also shown are the associated event discriminants. Event a) has tracks clearly consistent with a single primary vertex and thus has a low D value (D=0.02). Event b) has large numbers of tracks with significant impact parameters with respect to the primary vertex and has a high value of D (D=4.2). In the context of this analysis, we would classify the first event as a light quark event, the second a $Z \rightarrow b\bar{b}$ event.
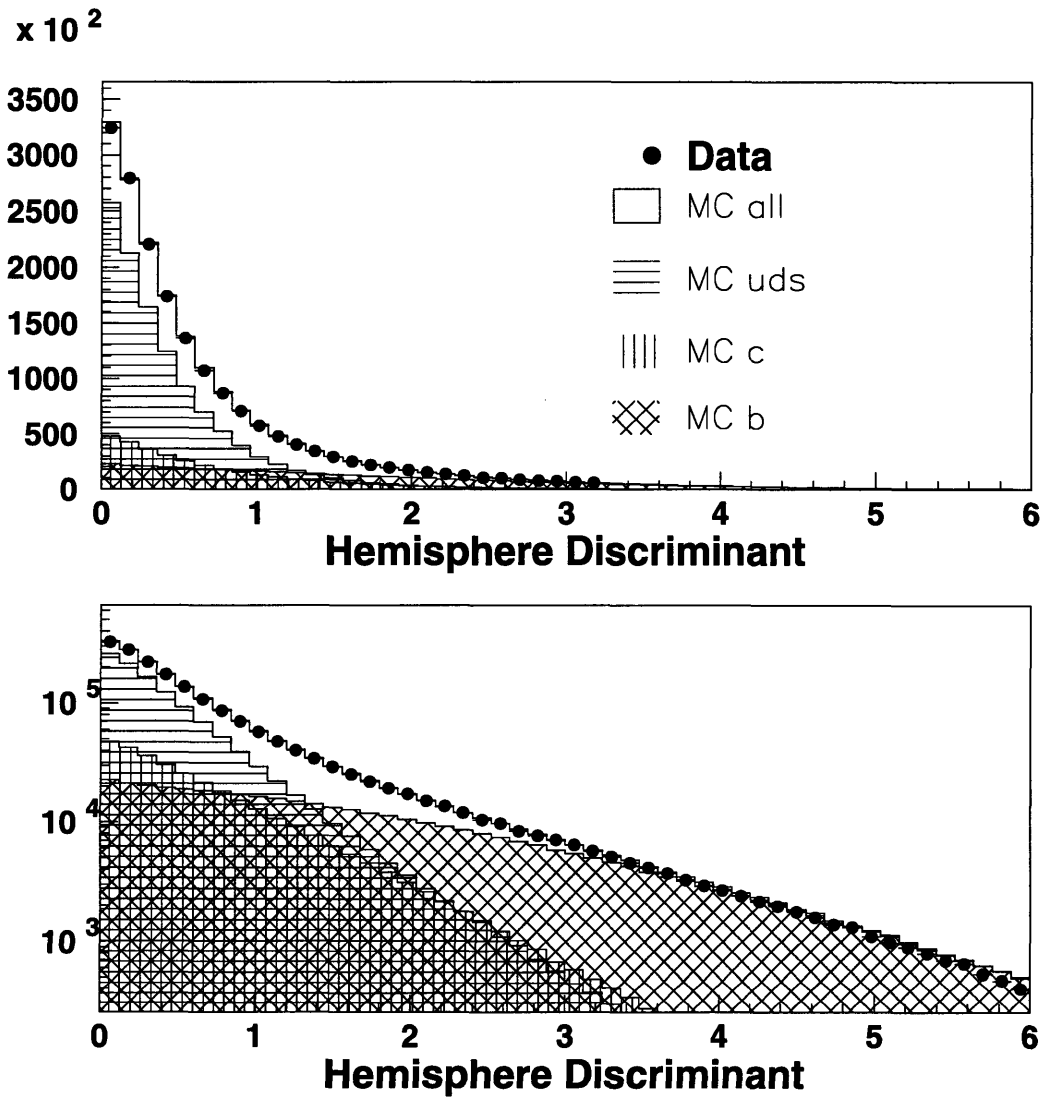
Figure 29: Hemisphere discriminant distribution in data and Monte Carlo plotted on linear and logarithmic scales. The flavour composition of the MC is also shown.
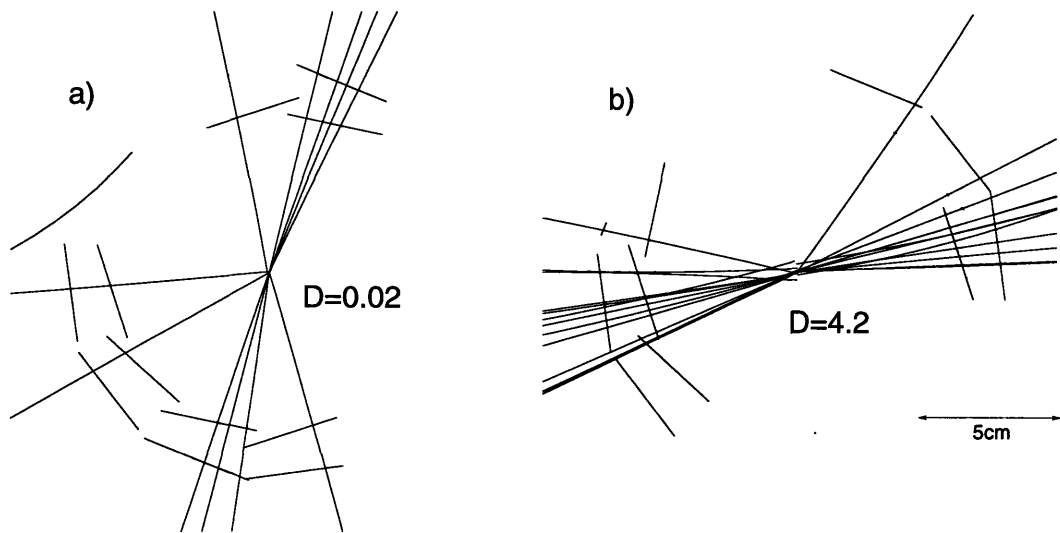
Figure 30: Two events as reconstructed in L3 and shown very close to the interaction point together with the the SMD layers that have contributed to the tracking. Associated event discriminants, D, as calculated using the techniques described in this section are also shown. a) is interpreted as a Z decay to light quarks, b) as a $Z \to b\bar{b}$ decay. a) is a magnified version of the event shown in figure 23.

7 Partial Z Decay Width to b$\bar{\text{b}}$

The impact parameter tag is used to extract a value of R_b using a *double tag* method. This technique is constructed so that the tagging efficiency may be obtained from the data itself, thus minimising dependence on the Monte Carlo simulation and associated systematic errors.

7.1 The Double Tag Method

In a hadronic event, the quark and anti-quark are generally produced approximately back-to-back and enter into opposite hemispheres. This allows us, in principle, to tag each hemisphere independently and, by counting the number of events where one, both or neither hemisphere is tagged, determine the b-tagging efficiency without reference to Monte Carlo simulation. The situation is complicated by the presence of light quark events in the sample and correlations between the hemispheres.

The discriminant D defined in equation 48 is determined in both hemispheres of the event separately, with the event's primary vertex in common. The number $N_t(D)$ of tagged hemispheres, ie, those that that have a discriminant greater than D, is related to the total number N_{had} of hadronic events by

$$\frac{N_t(D)}{2\,N_{had}} = R_b \left(\epsilon_b - \epsilon_{uds}\right) + R_c \left(\epsilon_c - \epsilon_{uds}\right) + \epsilon_{uds} \tag{49}$$

where $\epsilon_b(D)$, $\epsilon_c(D)$ and $\epsilon_{uds}(D)$ are the efficiencies of obtaining a single tag from b, c and light quark hemispheres respectively.

The number of events in which both hemispheres are tagged, $N_{tt}(D)$, is given by

$$\frac{N_{tt}(D)}{N_{had}} = R_b \left(C_b\epsilon_b^2 - c_{uds}\epsilon_{uds}^2\right) + R_c \left(c_c\epsilon_c^2 - c_{uds}\epsilon_{uds}^2\right) + c_{uds}\epsilon_{uds}^2 \tag{50}$$

where the additional factors $C_b(D)$, $c_c(D)$ and $c_{uds}(D)$, called hemisphere correlation factors, quantify correlations between tagging in the two hemispheres, which lead to a deviation from the simple power law reduction of the efficiencies. These factors are constructed such that $C = 1$ represents no correlation, $C > 1$ a positive correlation

65

and $C < 1$ an anti-correlation between the tagging efficiencies in the two hemispheres.

We determine R_b and ϵ_b from equations (49) and (50). The relative rate of c production, R_c is fixed to its Standard Model value of 0.171. The sensitivity of R_b to the assumed R_c will be stated explicitly with the final result. The efficiencies for quarks lighter than b, as well as the hemisphere correlation factors, are taken from the Monte Carlo simulation. However, only the factor C_b is relevant to the analysis for samples of high b purity.

The efficiency for b-tagging and the purity of the tagged sample are varied by cutting at various values of the discriminant variable D as shown in Figure 31 for the data and the Monte Carlo simulation. There is a residual difference between the efficiencies observed in data and Monte Carlo of $\sim 1\%$ absolute, independent of the discriminant cut over a wide range. This discrepancy does not directly propagate to an error in R_b since the Monte Carlo efficiency is not used. However, a change in efficiency may indirectly change the values of ϵ_c, ϵ_{uds} and C_b as obtained from Monte Carlo. This will be accounted for in the estimation of systematic errors.

Figure 32 shows values of R_b obtained as a function of the discriminant cut, for $b\bar{b}$ purities between 62% ($D > 1.25$) and 92% ($D > 3.15$). Good stability is shown with respect to the cut value. In order to decide on the discriminant cut at which to make the final measurement, we must make an estimate of the systematic errors. The cut may then be chosen to be that which minimises the total (statistical $\oplus$ systematic) error. This is described in the following sections.

7.2   Systematic Errors

The following contributions to the systematic error are considered:

- tracking resolution

- systematic error from background modelling

- systematics from hemisphere correlations

- finite Monte Carlo statistics
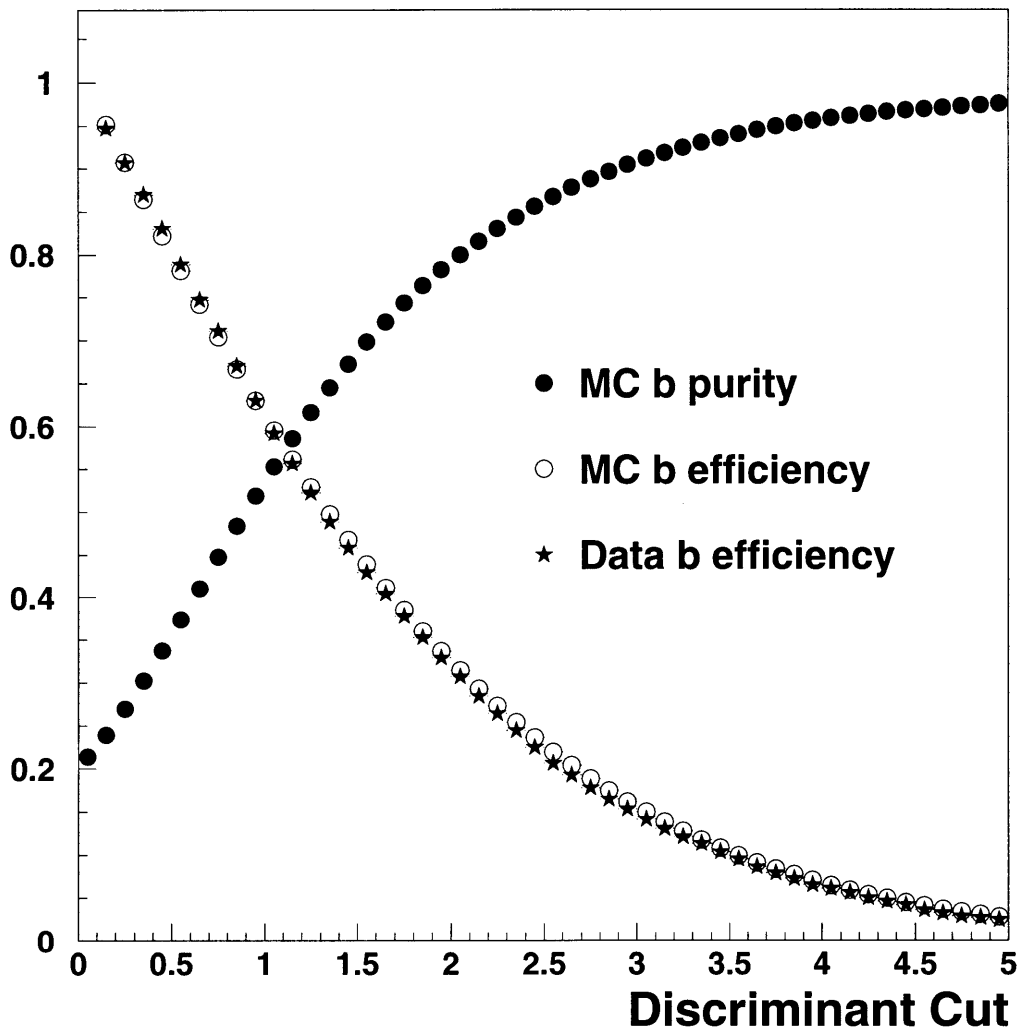
Figure 31: Efficiency and purity of the b̄b sample obtained as a function of the hemisphere discriminant cut. The data efficiency is determined using equations (49) and (50).
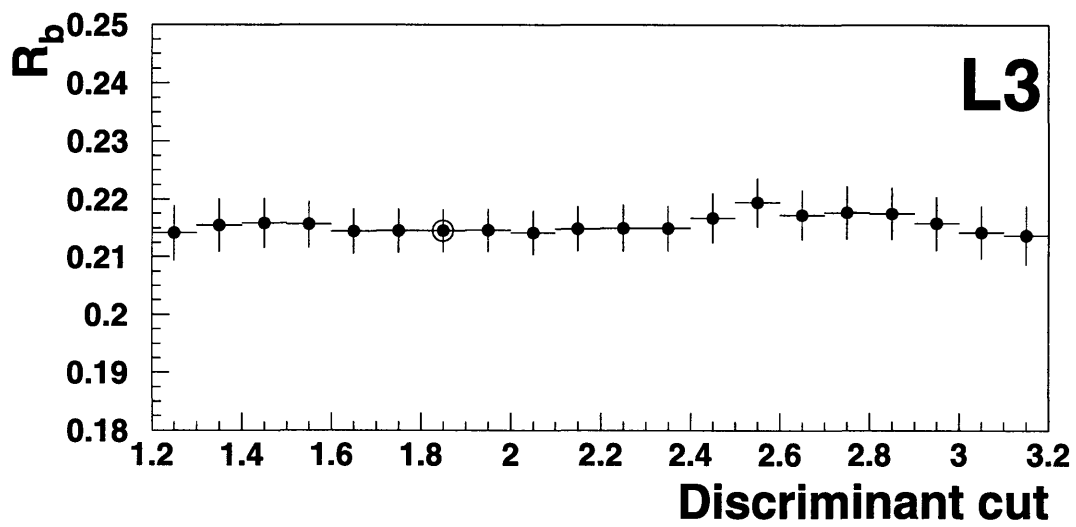
Figure 32: R_b as a function of discriminant cut. Errors shown are statistical $\oplus$ systematic. The systematic error estimation is described in section 7.2. The highlighted point is the R_b value associated with the lowest total error that is taken for the final measurement.

7.2.1 Tracking Resolution

Tracking resolution, ie, the distribution of negative track impact parameters, may be incorrectly modelled in the Monte Carlo. Since the resolution functions, $R(x)$, for each SMD hit pattern are determined from the data themselves, the measured value of R_b is largely insensitive to uncertainties in tracking resolution simulation. However, auxiliary parameters such as the hemisphere correlation and background efficiency may be influenced by tracking resolution uncertainty in the MC which has a secondary effect on R_b .

The magnitude of this uncertainty is estimated by performing the analysis both with and without the additional smearing, described in section 6.1, applied to tracks in the Monte Carlo. Half of the difference between the two R_b determinations is taken as the systematic error due to tracking resolution.

7.2.2 Background Modelling

The background efficiencies ϵ_{uds} and ϵ_c, which enter equations (49) and (50) are determined from the Monte Carlo and are hence sensitive to uncertainties in the simulation, particularly of charm quark fragmentation and in the production and decay of long lived hadrons.

The following sources of error are considered:

- the fragmentation of charmed hadrons,

- the production rates of the individual charm species,

- the lifetime of the individual charm species

- their decay multiplicities.

- fractions of long lived K^0 and Λ

- probabilities of gluon splitting to $b\bar{b}$ and $c\bar{c}$

The variation of the parameters is performed following the suggestions of reference [36]. The parameter ranges are listed in table 6. Events in the Monte Carlo are

re-weighted according to these ranges and the resultant changes in ϵ_{uds} and ϵ_c are propagated through to errors in R_b.

error source	value± error
Fractions in $c\bar{c}$ events:	
D^+	0.231 ± 0.026 [36]
D_s	0.110 ± 0.017 [36]
Λ_c	0.063 ± 0.029 [36]
Charm decay parameters:	
D^0 lifetime	0.415 ± 0.004 ps [37]
D^+ lifetime	1.057 ± 0.015 ps [37]
D_s lifetime	0.467 ± 0.017 ps [37]
Λ_c lifetime	0.206 ± 0.012 ps [37]
D decay multiplicity	2.53 ± 0.06 [38]
$D \rightarrow K^0$ multiplicity	0.46 ± 0.06 [38]
Charm fragmentation parameter:	
$< x_E(c) >$	0.484 ± 0.016 [36]
Fractions in uds events:	
K^0 and Λ	JETSET $\pm$ 10%
$g \rightarrow c\bar{c}$	2.38 ± 0.048 % [36]
$g \rightarrow b\bar{b}$	$(0.13 \pm 0.04) \times g \rightarrow c\bar{c}$ [36]

Table 6: Variation of modelling parameters used for the determination of the systematic error. The charm fragmentation error is inflated by a factor of two in order to account for uncertainties of the shape of the fragmentation function.

7.2.3 Hemisphere Correlations

Correlations between the b-tagging efficiencies in the two hemispheres of an event can arise from various sources. As the value of R_b obtained by the double tag method is directly proportional to the correlation coefficient, C_b, it is important to understand the origins of this effect. In addition, since we take C_b from the Monte Carlo, there is a systematic error associated with it due to uncertainties in the simulation. The method described below is an attempt to both understand the origins of the correlation and to quantify the Monte Carlo uncertainties.

A possible source of correlation can be quantified by choosing a variable q for each hemisphere which could be influenced by tagging in the opposite hemisphere. For a

70
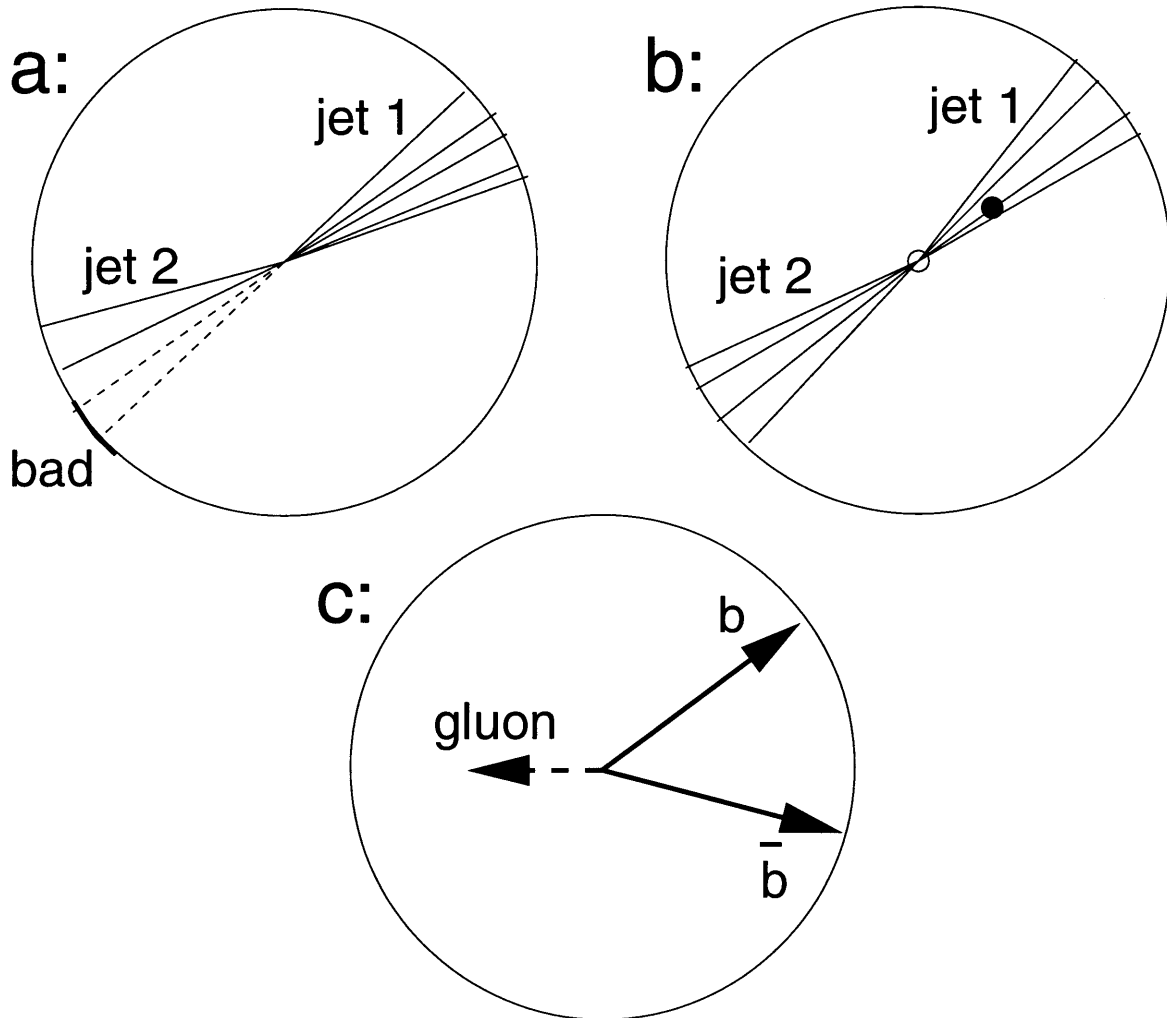
Figure 33: Illustration of the three main sources of hemisphere correlation: a) Bad region of the detector leads to badly reconstructed tracks, hence a loss in tagging efficiency, in one hemisphere. b) Badly reconstructed vertex (black circle) some distance from the real vertex (white circle) gives artificially large impact parameters in one hemisphere, artificially small in the other. c) Emission of a hard gluon pushes both b quarks into the same hemisphere.

particular cut on the hemisphere discriminant we then define three distributions:

- the normalised distribution of q for all hemispheres, $N(q)$.

- the single hemisphere tagging efficiency as a function of q, $\epsilon(q)$

- the normalised distribution of q in co-tagged hemispheres $C(q)$ (a co-tagged hemisphere is one opposite a tagged hemisphere, regardless of whether it is itself tagged).

We then form a coefficient, C_b^q, reflecting the correlation characterised by q for this particular discriminant cut, D:

$$C_b^q = \frac{\int \epsilon(q) \; C(q) \; dq}{\int \epsilon(q) \; N(q) \; dq} \tag{51}$$

$C_b^q = 1$ implies that there is no correlation between the hemisphere tagging efficiencies characterised by q. $C_b^q > 1$ indicates a positive correlation, $C_b^q < 1$ an anti-correlation.

We repeat the analysis for a number of different variables q. For a sample of $Z \to b\bar{b}$ Monte Carlo , the sum of the separate components, $1+\sum(C_b^q - 1)$, is then compared with the total measured correlation in the sample C_b. If the agreement is reasonable we can be sure to have identified the most important sources of correlation. We can then compare the correlation components in data and Monte Carlo, with a mixture of quark flavours, to estimate the error on the Monte Carlo prediction for the total correlation.

We considered three sources of correlation, described below and illustrated schematically in figure 33:

1. Detector effects: inefficient regions of the detector can lead to correlations due to the back-to-back nature of hadronic events. This is estimated using $q = \cos \theta$ and $q = \phi$ where θ and ϕ are the polar and azimuthal angles of the most energetic jet in each hemisphere.

2. Reconstruction effects: both hemispheres use the same primary vertex which is heavily constrained by the position of the 200-event-vertex. If the reconstructed

primary vertex is artificially shifted into one hemisphere, that hemisphere will have a low tagging efficiency, the other a high efficiency. This leads to a negative correlation ($C_b < 1$). To quantify this effect, a primary vertex is constructed separately in each hemisphere using only the tracks assigned to it. q is taken to be the distance in the xy plane between the vertex in each hemisphere and the overall event vertex. q is given a sign according to how far each hemisphere vertex moves when the 200-event-vertex constraint is removed: the hemisphere in which the movement is greater is assigned $q > 0$, the other $q < 0$.

3. Physics effects: The presence of hard gluons in an event can influence the tagging efficiency of both hemispheres by taking energy away from the primary quarks or, in the extreme case, by pushing both quarks into the same hemisphere. The event thrust, T, is a measure of this effect and we take $q = \pm T$ with the positive sign for the hemisphere with the highest energy jet.

Fig. 34a shows the correlation due to the above three sources together with their linear sum and the total measured correlation as a function of the cut on the hemisphere discriminant for a sample of simulated $Z \to b\bar{b}$ events. The dominant components are those due to gluon radiation and vertex bias. The component sum shows reasonable agreement with the total correlation in the region of the cuts used for the R_b measurement. The small remaining discrepancy is due to additional sources of correlation or to interference between the sources considered. The systematic error arising from these effects is taken to be negligible.

We expect the different components to vary depending on the flavour composition of the data sample. In principle, we should compare components for pure $b\bar{b}$ samples in both data and Monte Carlo to truly measure the quality of the MC correlation simulation. Since this is impossible in the data, we obtain a 70% b-purity by requiring the event discriminant to be greater than 1.5. The data is compared with a sample of mixed-flavour MC with the same cut on the event discriminant. A comparison of the resulting component sums is shown in figure 34b. The MC component sum is slightly different from that in Fig. 34a demonstrating the difference in correlation in
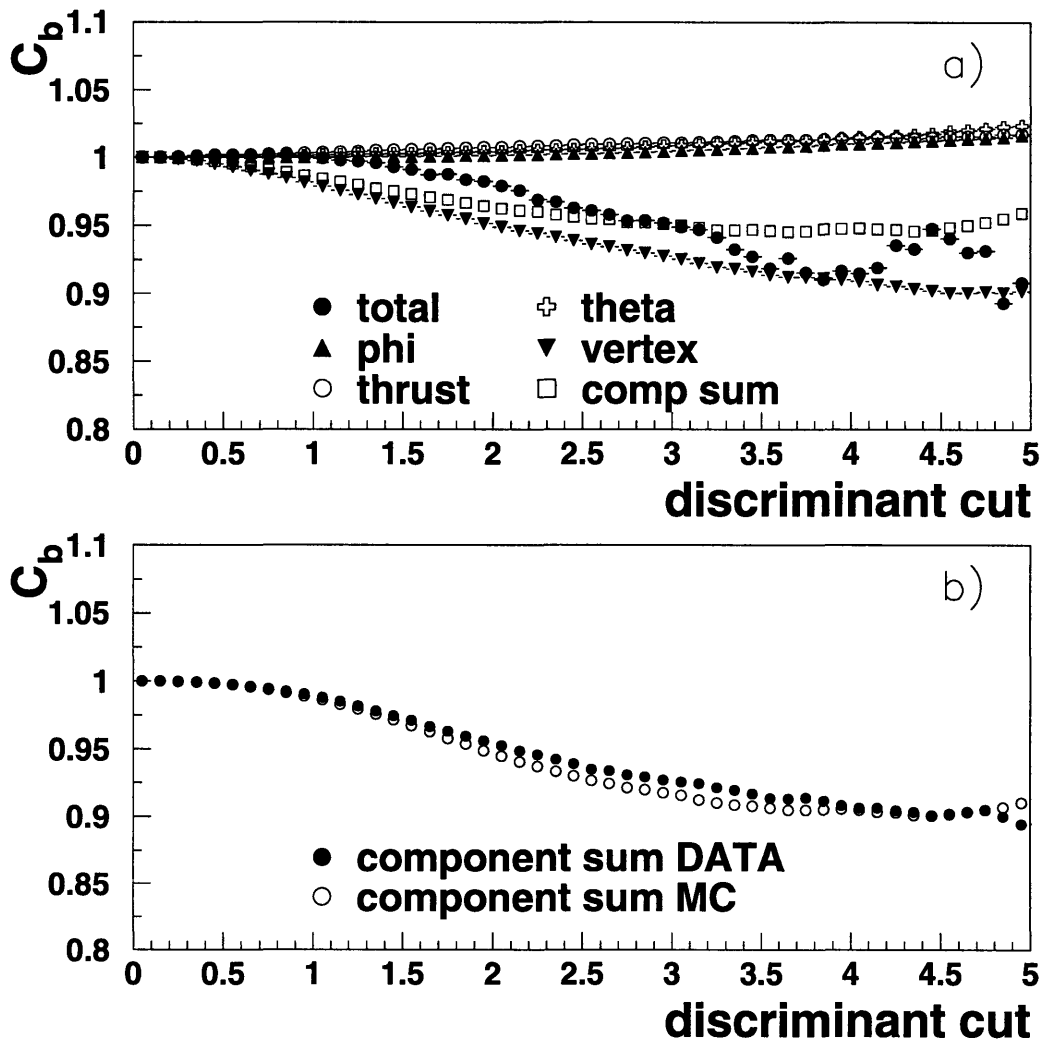
Figure 34: a) Correlation components and total measured correlation for simulated $Z \rightarrow b\bar{b}$ events. b) Correlation component sum in data and Monte Carlo. Here, events are required to have an event discriminant > 1.5 giving a b-purity of $\sim 70\%$. The difference between the plots is taken as the systematic error on C_b.
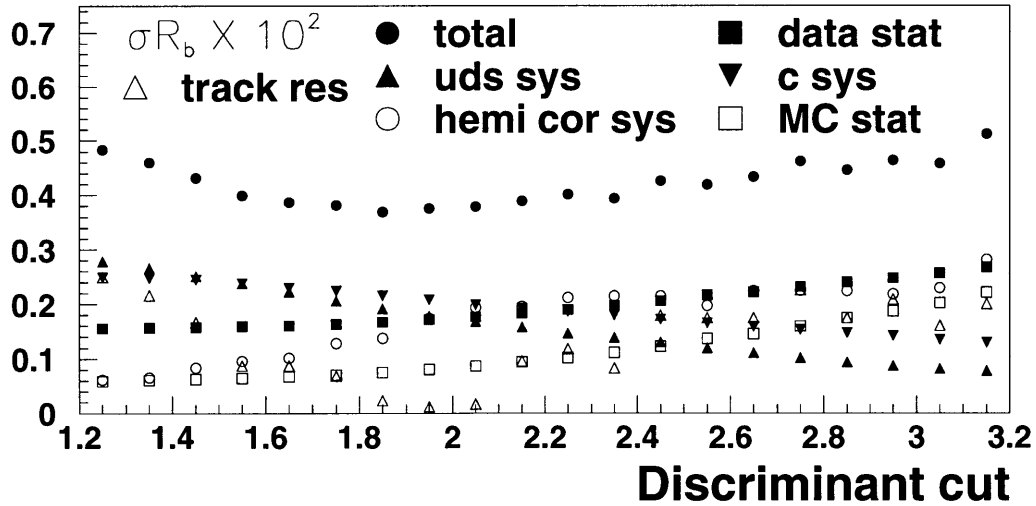
Figure 35: Statistical, systematic and total errors for R_b as a function of the discriminant cut.

a 100% $b\bar{b}$ sample and a sample with $\sim$ 30 % light quark contamination. There is a small difference between component sums in data and Monte Carlo, the latter slightly overestimating the vertex bias contribution. This difference is taken as the systematic error on the correlation coefficient and propagated through to a systematic error on R_b.

7.2.4 Monte Carlo Statistics

The error on ϵ_{uds}, ϵ_c and C_b due to the use of finite Monte Carlo statistics is propagated to through to an error on R_b.

7.3 Results

Figure 35 shows the statistical and systematic errors on R_b as a function of the discriminant cut. Minimising the total (statistical $\oplus$ systematic) error, we choose $D > 1.85$ to define the central value of our measurement. This corresponds to a b-purity of 76%.

At this point, $\epsilon_{uds} = 1.92 \pm 0.05\%$ and $\epsilon_c = 6.99 \pm 0.26\%$. Error breakdowns are shown in Table 7 and 8 . Since the individual charm lifetimes are measured very precisely, the fractions of the different species becomes one of the major error contributions. Among all the charmed hadrons, the D^+ properties lead to the dominant errors because it has the longest lifetime.

The value of the correlation coefficient for $D > 1.85$ is $c_b = 0.980 \pm 0.003(stat) \pm 0.006(sys)$, where the first error comes from Monte Carlo statistics and the systematic error has been assigned according to the study described in the previous section.

The final measurement of R_b using data collected by L3 in 1994-1995 is

$$R_b = 0.2146 \pm 0.0017(\text{stat}) \pm 0.0033(\text{sys}) - 0.139 \ (R_c - 0.171) \qquad (52)$$

The breakdown of systematic errors is given in table 9. The final term in (52) demonstrates the dependence of the result on the assumed value of R_c via equations (49) and (50). For example, if we chose to use the experimental average ($R_c = 0.1540 \pm 0.0074$ from table 2) instead of the Standard Model value, the central R_b value shifts by 0.0024 to 0.2170. This is within the quoted systematic error.

error source	$\Delta\epsilon_{uds} \times 10^2$
MC Statistics	0.01
Track Resolution	0.04
K^0 and Hyperons	0.03
Gluon splitting	0.01
Total	0.05

Table 7: Error contributions to ϵ_{uds} for a cut at $D > 1.85$.

error source	$\Delta\epsilon_c \times 10^2$
MC Statistics	0.04
Track Resolution	0.09
Charm fractions	0.14
Charm lifetime	0.03
D decay multiplicity and D $\to$ K$_s^0$ multiplicity	0.17
$< x_E(c) >$	0.09
Total	0.26

Table 8: Error contributions to ϵ_c for a cut at $D > 1.85$.

error source	$\Delta R_b \times 10^2$
uds efficiency	0.19
c efficiency	0.22
hemisphere correlations	0.14
tracking resolution	0.02
MC statistics	0.08
total	0.33

Table 9: Breakdown of systematic errors on R_b for a discriminant cut of $D > 1.85$.

8 Cross Check of the R_b Measurement.

To check the R_b measurement, a different signature of $Z \rightarrow b\bar{b}$ decays is used: high momentum leptons coming from the semi-leptonic decay of heavy quarks[4].

8.1 Lepton Tag
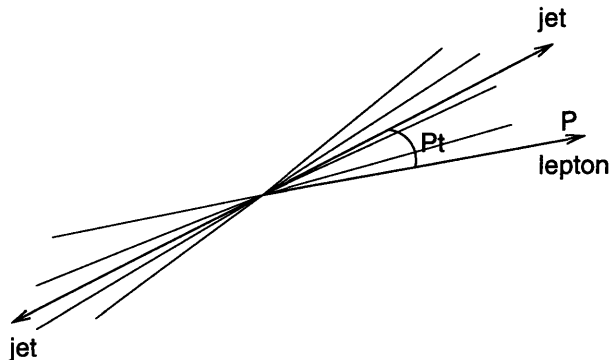
Figure 36: Illustration of a $Z \rightarrow b\bar{b}$ event in which one of the hadrons containing b-quarks decays semi-leptonically. The lepton has both high momentum P and high momentum transverse to the nearest jet P_t.

About 10% of the time, hadrons containing b quarks decay semi-leptonically [41]. Because of the high mass of the b quark, leptons from b decay are distinguished from leptons coming from other semi-leptonic decays by their high momentum (P) and momentum transverse to the axis of the jet with which they are associated (P_t), figure 36. The distribution of P and P_t is shown in figure 37 for electrons and muons[5] produced in hadronic Z decays. The variable used for tagging $Z \rightarrow b\bar{b}$ decays is P_t.

Since neither, either or both of the primary quarks can decay semi-leptonically, we can now proceed with the analysis in exactly the same way as the lifetime tag by looking for events with 0, 1 or 2 tagged hemispheres and performing a double tag analysis (a tagged hemisphere here is one in which there is an electron or muon with P_t exceeding a certain cut). Since the tag does not require detailed tracking information

---

[4]This analysis is taken from [39].

[5]τ leptons are not considered for this analysis because their decay makes them difficult to identify in hadronic events.

Figure 37: P and P_t of electrons and muons with flavour composition in MC.

we can use the entire $Z \rightarrow q\bar{q}$ data sample collected by L3 corresponding to about 3 million events. A list of the numbers of tagged hemispheres (N_t) and double-tagged events (N_{tt}) is given in table 10 for various values of the P_t cut. The low numbers indicate the statistical limitations of the method compared with the lifetime tag.
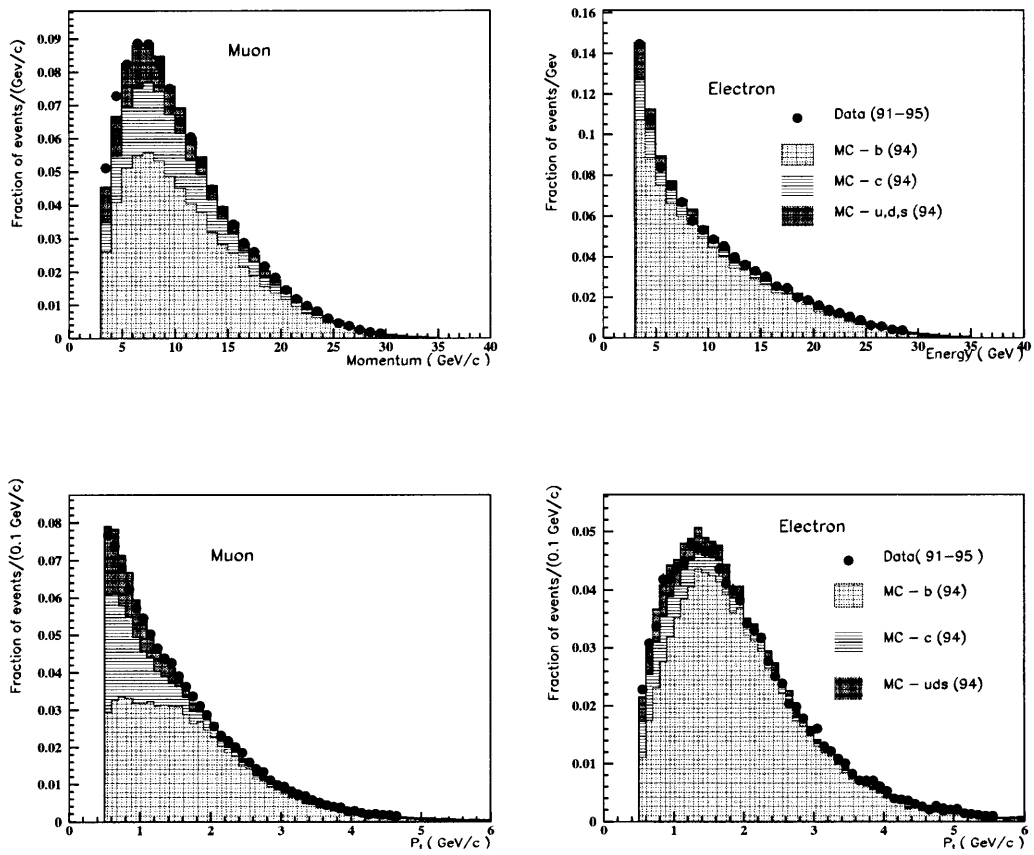
P_t cut	1.0 GeV	2.0 GeV	3.0 GeV
N_t	81324	34640	12270
N_{tt}	3802	624	81

Table 10: Numbers of tagged hemispheres and double-tagged events, lepton tag.

Figure 38 shows the purity of the tag as a function of P_t cut and the double-tag efficiency in data and MC. As with the impact parameter analysis, the Monte Carlo reproduces the data efficiency to within 1% absolute.

8.2 Results

We can now proceed with the analysis of errors in the same way as section 7.2. In addition, we are now sensitive to the semi-leptonic branching ratio for c quarks which enters as the main background to $Z \rightarrow b\bar{b}$ events. We take $BR(c \rightarrow l) = 9.8 \pm 0.5\%$ from [36].

The analysis of hemisphere correlations is simpler here. We find the factor C_b to be consistent with 1 (ie, no correlation between the hemispheres) to within the Monte Carlo statistical error which is taken conservatively as the C_b systematic.

Figure 39 shows the measurement errors as a function of P_t cut. A cut of $P_t > 0.9$ GeV is chosen so as to minimise the total error. The systematic errors for this cut are shown in table 11.

The value obtained for R_b is:

$$R_b(\text{lepton tag}) = 0.2226 \pm 0.0038(\text{stat}) \pm 0.0046(\text{syst}) - 0.28\ (R_c - 0.171) \qquad (53)$$

This is in good agreement both with the number obtained using the lifetime tag and
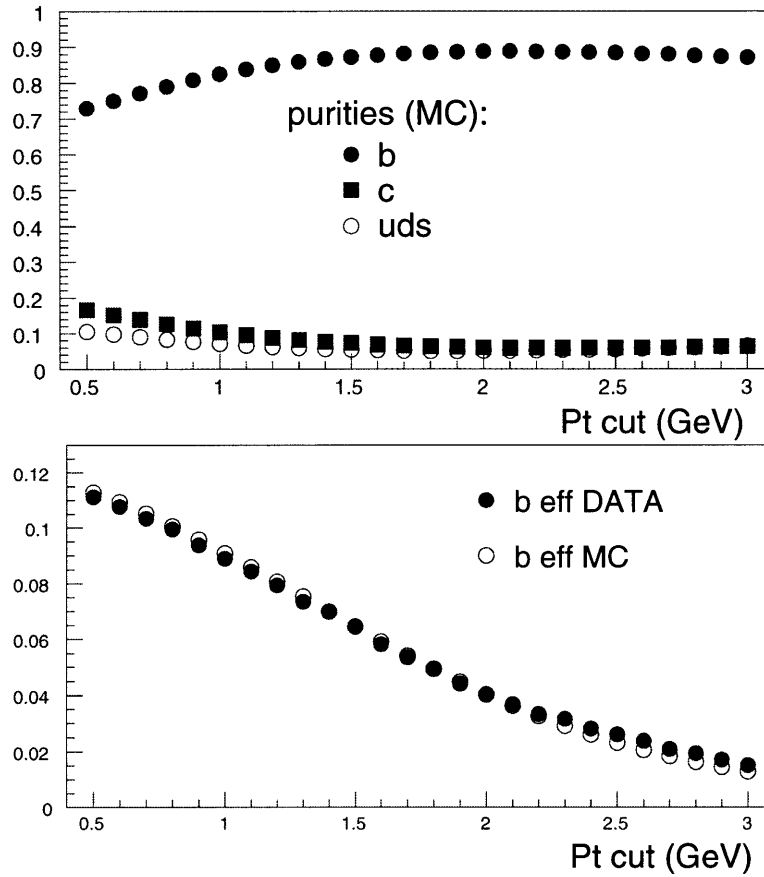
Figure 38: Flavour purity and efficiency of the lepton tag as a function of P_t cut.
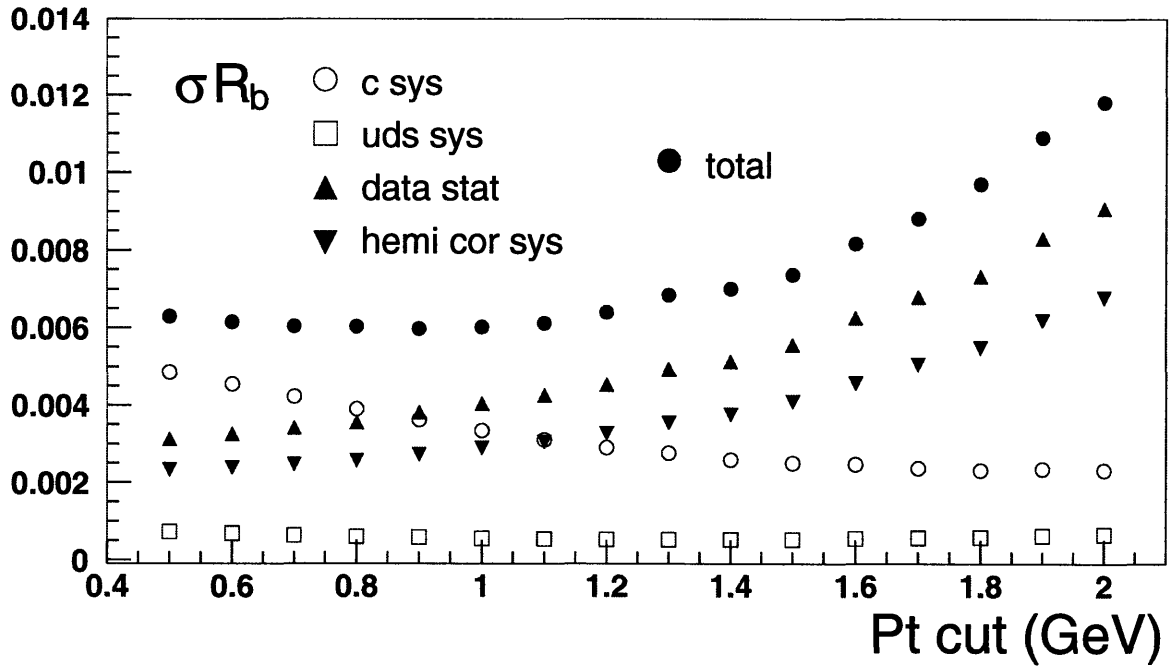
Figure 39: Errors on R_b as a function of P_t cut.

the Standard Model , see fig 40. The statistical limitations of the lepton tag are clear; even though the data sample is more than twice that used for the lifetime analysis, the final statistical error is more than twice as large. Nevertheless, the lepton analysis is a useful cross-check of the R_b measurement.

Source of Uncertainty	ΔR_b
$BR(c \to l)$	0.0028
c fragmentation	0.0023
c MC statistics	0.0006
total c uncertainty	0.0036
uds fragmentation	0.0002
uds MC statistics	0.0006
total uds uncertainty	0.0006
hemisphere correlation	0.0027
lepton identification	0.0005
total	0.0046

Table 11: Breakdown of systematic errors on the R_b measurement using the lepton tag.
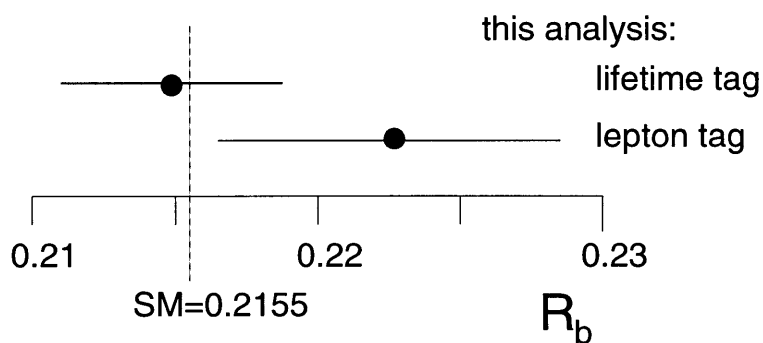
Figure 40: R_b as measured in this thesis using lifetime and lepton tags compared with the Standard Model prediction for $m_{top} = 174$ GeV.

9 Forward Backward Asymmetry of b Quark Production

The forward-backward asymmetry of $Z \rightarrow f\bar{f}$ was defined in section 2.3. For this measurement it is necessary to be able to distinguish the fermion from the anti-fermion. This is done by identifying their charges.

If f is a charged lepton, the charges are easy to determine. The case where f is a quark is complicated by the fact that we do not observe the original quarks but the many final-state particles that are the result of fragmentation. However, some information about the charge of the primary quark remains accessible from the charges and momenta of the final state hadrons.

If a quark decays semi-leptonically, the sign of the quark charge will be given by the sign of the charge of the detected lepton. This method is limited by statistics: B.R. $(b \rightarrow l\nu) \sim 10\%$ where l is an electron or muon [41], ie, we expect to identify the b-quark charge in about 10% of $Z \rightarrow b\bar{b}$ events.

An alternative is to form a *hemisphere charge*, Q_H, from the momentum-weighted average charge of all the final state particles in a hemisphere which, on a statistical basis, reflects the sign of the charge of the primary quark entering that hemisphere. Studies of quark-gluon fragmentation indicate that the quark charge can be determined in up to around 70% of $Z \rightarrow b\bar{b}$ events [40], hence this method has a statistical advantage over the semi-leptonic technique.

9.1 Hemisphere Charge Algorithm

The procedure for constructing Q_H is:

- The event is divided into two hemispheres by a plane through the origin, perpendicular to the beam axis. The forward (backward) hemisphere is defined as the one whose projection along the beam axis is in the direction of the e^- (e^+) beam. The positive (negative) hemisphere is the one into which the positive (negative) primary quark entered.

- Tracks are associated to the nearest jet in ϕ.

- Tracks are assigned to the same hemisphere as their associated jet.

- Q_H is formed for each hemisphere using the tracks assigned to it and the algorithm defined below. Q_F and Q_B denote the hemisphere charges thus obtained in the forward and backward hemispheres respectively.

Charged final-state particles in hadronic Z decays are primarily pions and protons. Their charge $q = \pm 1$ is determined by the direction of bending in the L3 magnetic field as measured in the TEC. High $P_\perp$ (momentum transverse to the beam axis) particles are more likely to carry information about the charge of the primary quark because they tend to come from higher up in the fragmentation chain. However, since the magnetic deflection of high $P_\perp$ particles is small, there is an increased chance of TEC assigning the wrong-sign charge as $P_\perp$ increases. To take these competing effects into account we form Q_H in terms of a momentum-weighted sum of the charge of all tracks in a hemisphere using a variable exponent, k, which is adjusted to give the maximum separation of positive and negative hemispheres [40]. To increase the charge separation we take $P_\perp$ projected along the thrust axis in $r\phi$:

$$Q_H = \frac{\sum q |P_\perp^k \cos \delta|}{\sum |P_\perp^k \cos \delta|} \tag{54}$$

where δ is the angle between the track and the thrust axis in the $r\phi$ plane.

Tracks are selected for the Q_H determination according to the following set of cuts:

- There should be at least 10 associated hits in the TEC.

- The separation between first and last hits should exceed 20 radial wire lengths.

- $P_\perp$ should be between 1 and 50 GeV.

- The distance of closest approach to the primary vertex should be less than 10 mm.

85
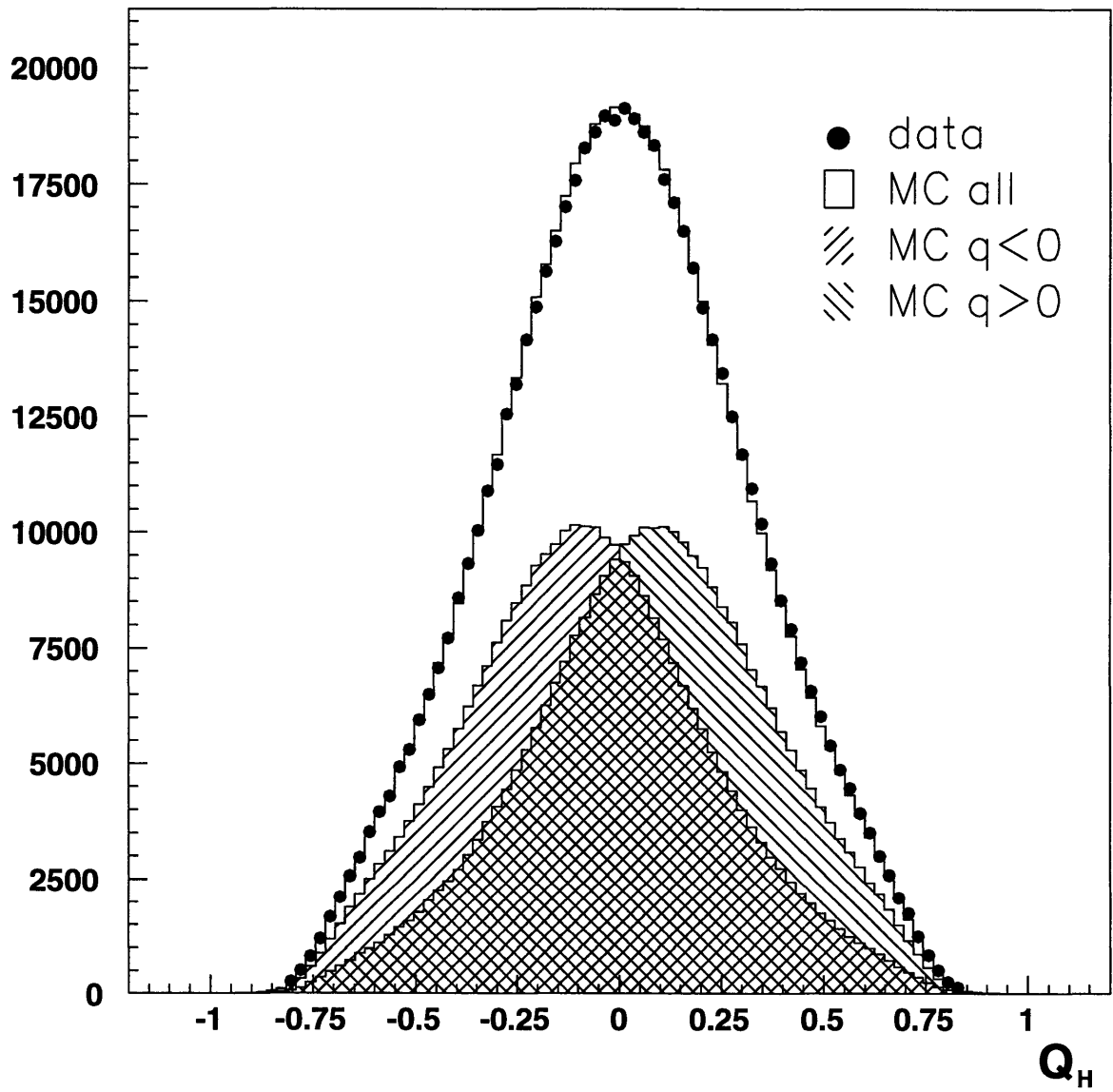
Figure 41: Hemisphere charge for data and MC with $k = 0.5$. For the MC, the charge in hemispheres with a positive ($q > 0$) and negative ($q < 0$) primary quark is also shown.

Figure 41 shows Q_H for data and Monte Carlo with $k = 0.5$. The MC is also split into positive and negative hemispheres and their separation illustrates the principle of the method. The mean and r.m.s. widths of the data and MC distributions are given in table 12.

distribution	mean	r.m.s width
data	0.001	0.308
MC all	-0.001	0.307
MC $q < 0$	-0.081	0.297
MC $q > 0$	0.078	0.297

Table 12: Means and r.m.s. widths of the hemisphere charge distributions in the data and Monte Carlo.

We define a forward (backward) event as one in which the positive quark enters into the forward (backward) hemisphere. For a forward event, $Q_F > Q_B$ indicates that the charge flow of the event has been correctly identified and vice-versa for a backward event. For a sample of MC events we count the number of events in which the charge flow was correctly determined, N_{cor}. Dividing by the total number of events, N_{tot}, we obtain P, the probability of identifying the direction of quark and antiquark:

$$P = N_{cor}/N_{tot} \qquad (55)$$

Figure 42 shows P for a number of different values of the parameter k. The value $k = 0.5$ is found to give the maximum charge-tagging probability, $P \approx 65\%$, and is used in the remainder of this analysis.

9.2 Measuring the Asymmetry

A sample of Z decays consists of N_F forward and N_B backward events. We can also determine the number of apparent forward and backward events by counting those with $Q_F > Q_B$ and $Q_F < Q_B$ respectively, N'_F, N'_B. There are then two asymmetries to consider: the true asymmetry, A, and the apparent asymmetry, A':

87
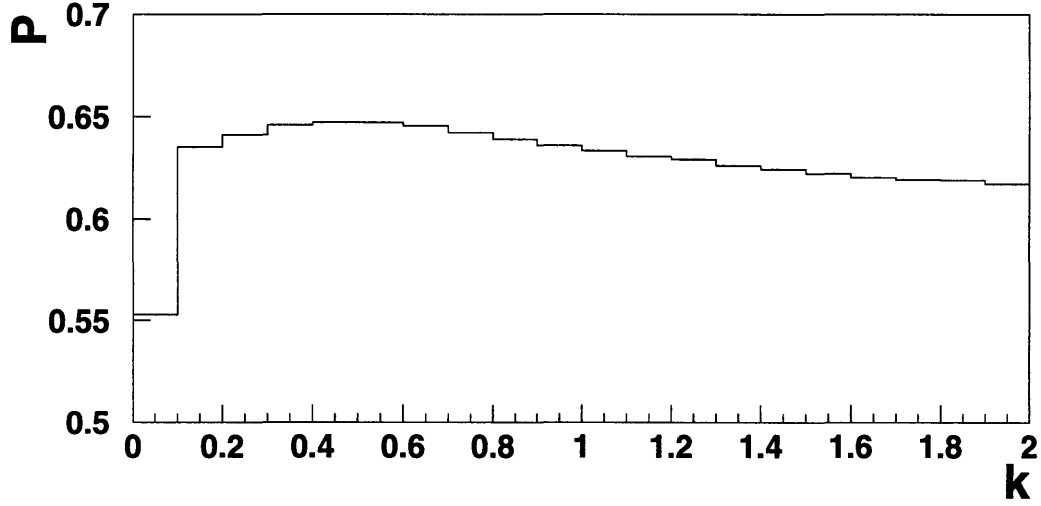
Figure 42: Charge-tagging probability P for different values of the parameter k as determined from the Monte Carlo.

$$A = \frac{N_F - N_B}{N_F + N_B} \quad A' = \frac{N'_F - N'_B}{N'_F + N'_B} \tag{56}$$

These are linked via the charge-tagging probability:

$$A' = A(2P - 1) \tag{57}$$

The apparent asymmetry in the sample is the sum of five terms reflecting the five quark flavours that the Z can decay to (d,u,s,c,b):

$$A' = \sum_{i=1,5} A^i_{FB}(2P_i - 1)f_i s_i \tag{58}$$

where A^i_{FB} is the asymmetry of Z decays to quark flavour i, P_i is the probability of obtaining the correct charge flow in a $Z \rightarrow q_i \bar{q}_i$ event, f_i is the fraction of quark i in the sample and s_i is $+1$ for u,c, -1 for d,s,b (reflecting the fact that the quarks with positive baryon number have opposite sign charges for up and down-type). To extract A^b_{FB} from the data we first apply b-tagging by selecting events with an event

88
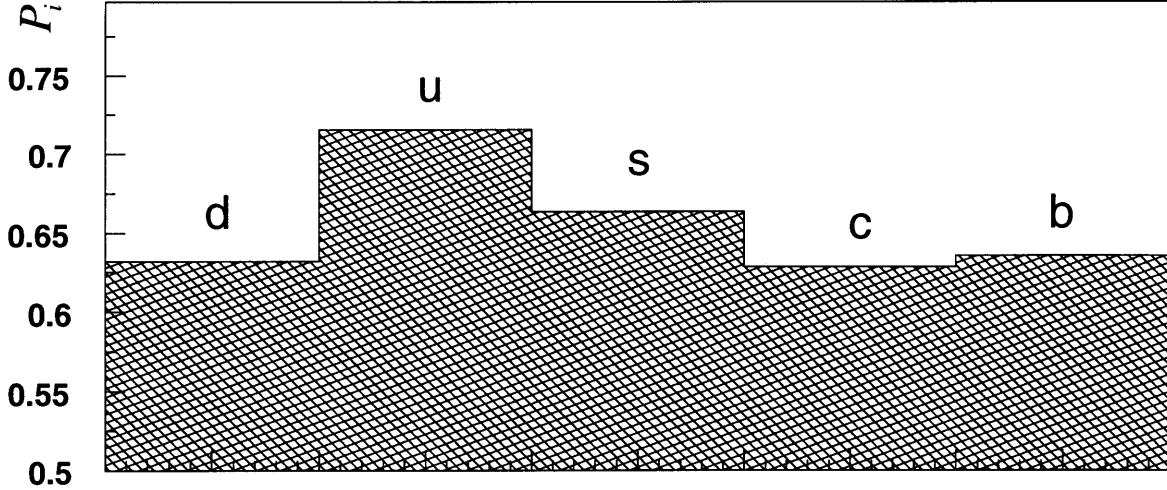
Figure 43: Probability of obtaining the correct charge flow in Z decays to the different quark flavours, taken from Monte Carlo.

discriminant D greater than a certain cut to obtain a sample where $f_i \approx 0$ for $i \neq b$. We assume that $A^d_{FB} = A^s_{FB}$, $A^u_{FB} = A^c_{FB}$ and that these are given by their standard model values, table 13. Then, rearranging equation (58):

$$A^b_{FB} = \frac{A' + A^u_{FB}[(2P_u - 1)f_u + (2P_c - 1)f_c] - A^d_{FB}[(2P_d - 1)f_d + (2P_s - 1)f_s]}{(2P_b - 1)f_b}$$

(59)

A' is measured in the data, P_i and f_i ($i = 1, 5$)must be taken from the MC. Figure 43 shows the MC prediction of P_i for each quark flavour. The f_i depend strongly on the b-tag discriminant cut D.

quark pair	A^q_{FB} (%)
$d\bar{d}$	9.36
$u\bar{u}$	6.00
$s\bar{s}$	9.36
$c\bar{c}$	6.00

Table 13: Values used for the non-b-quark forward-backward asymmetries. These are taken from ZFITTER [8] using $\sqrt{s} = 91.22$ GeV and $m_{top} = 174$ GeV.

9.3 Acceptance Factor

Because of the finite size of the SMD, track quality is diminished in the far forward and backward regions of the detector resulting in a loss of b-tagging efficiency. To counter this affect, a cut is applied to the polar angle of the event thrust, $\cos\theta_{th} < 0.7$, in order to confine most tracks to the efficient region. This means that the measured asymmetry is less than the actual asymmetry in the sample by an *acceptance factor* which can be determined thus:

Since θ_{th} is a good measure of the primary quark direction, it is assumed to follow the form given in section 2.3:

$$\frac{d\sigma}{d\cos\theta_{th}} \propto 1 + \cos^2\theta_{th} + \frac{8}{3}A\cos\theta_{th} \tag{60}$$

Where A is the true asymmetry.

The number of forward and backward events is then obtained by integrating 60 up to the acceptance cut $|(\cos\theta_{th})_{max}| = x$:

$$N_F = x + \frac{4}{3}x^2A + \frac{1}{3}x^3 \tag{61}$$

$$N_B = x - \frac{4}{3}x^2A + \frac{1}{3}x^3 \tag{62}$$

The measured asymmetry is then:

$$A_{measured} = \frac{N_F - N_B}{N_F + N_B} = \frac{4x}{3 + x^2}A \tag{63}$$

Thus, for a cut of $|(\cos\theta_{th})_{max}| = 0.7$ we must multiply the measured asymmetry by 1.246 to obtain the true asymmetry.

Figure 44 shows the acceptance factor corrected b-quark asymmetry measured for various values of the b-tag discriminant cut, D. The errors shown are purely statistical. The measurement shows good stability over a wide range of D cuts. In order to chose the optimum cut we must make an estimation of the systematic errors on the measurement and chose the cut which minimises the total error (statistical $\oplus$ systematic).
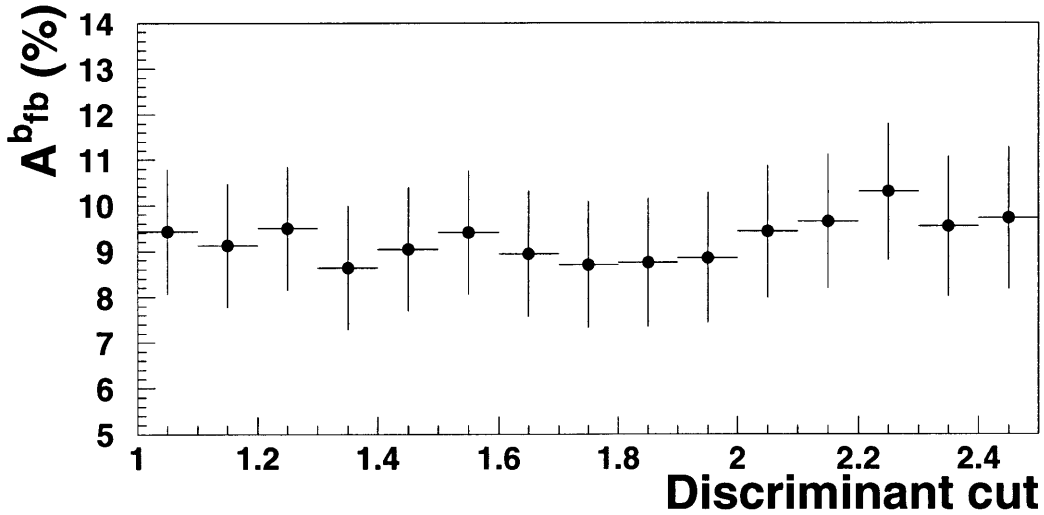
Figure 44: Measured A^b_{FB} for different values of the b-tag discriminant cut. The errors are purely statistical.

9.4 Systematic Errors

The main systematic errors in the A^b_{FB} measurement arise from the use of Monte Carlo simulation to estimate the factors P_i and f_i in equation (59). These can be divided into four areas:

- fragmentation uncertainties

- tagging efficiency estimation

- detector effects

- finite Monte Carlo statistics

Quantitative estimates of these effects are described below.

9.4.1 Fragmentation Uncertainties

Because of the non-perturbative nature of QCD, there is an inherent difficulty in making quantitative predictions about the behaviour of a quark-gluon system as it

91
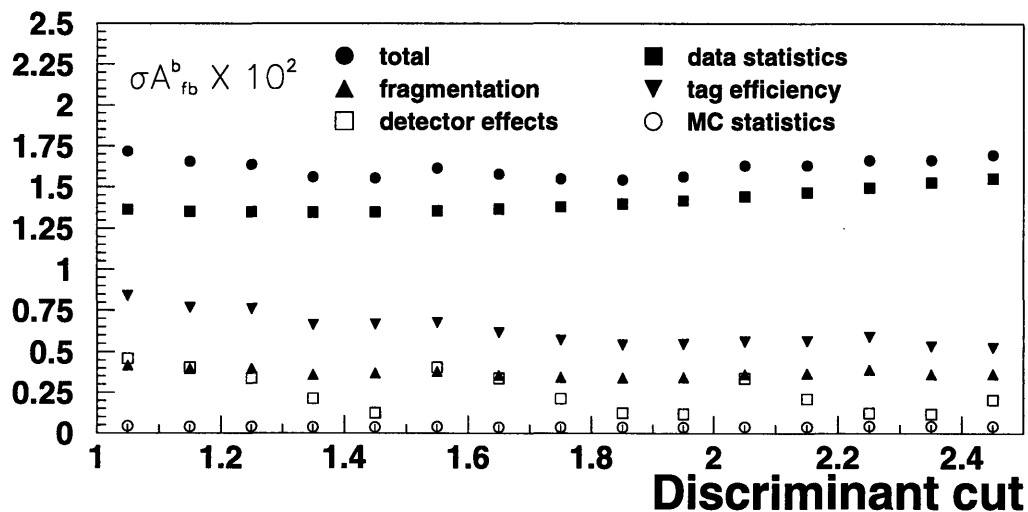
Figure 45: Breakdown of statistical and systematic errors on the A^b_{FB} measurement for different discriminant cuts.

fragments into jets of stable particles. To proceed, assumptions must be made about the nature of the fragmentation process that are both consistent with QCD and computable in a finite time. The approach taken by JETSET is to use a model whereby quarks are joined by a flux-tube of gluons, rather like a string, which can break to form new quark-antiquark pairs [33]. This model is dependent on a large number of parameters which must be tuned to give a realistic representation of the data. Any such tuning will only be approximate and there is thus a basic uncertainty in the predictions of the Monte Carlo. The hemisphere charge is particularly sensitive to this uncertainty and hence the probability of obtaining the correct charge flow for each quark flavour is unknown to some extent.

In order to estimate the size of this effect, particular JETSET parameters, on which the sensitivity of Q_H is thought to be large, are varied by their estimated errors. A fast detector simulation is then used to estimate the corresponding variation in $P_i(i = 1, 5)$ which is then propagated through to an error in A^b_{FB} for each parameter. The total error is taken as the sum in quadrature of the individual errors. A list of

the JETSET parameters considered and the range through which they were varied is given in table 14 along with the associated change in A_{FB}^b for a discriminant cut of 1.85. The precise meanings of these parameters can be found in [33].

Parameter	JETSET Name	Range	$\delta A_{fb}^b \times 10^2$
Λ_{QCD}	PARJ(81)	0.311 ± 0.037 [42]	∓ 0.02
Q_0	PARJ(82)	1.0 ± 0.4 [42]	∓ 0.00
σ_q	PARJ(21)	0.41 ± 0.03 [42]	± 0.19
γ_s	PARJ(2)	0.30 ± 0.03 [42]	∓ 0.11
P_{ud}	PARJ(11)	0.50 ± 0.18 [42]	± 0.00
P_s	PARJ(12)	0.60 ± 0.13 [42]	∓ 0.05
P_{bc}	PARJ(13)	0.75 ± 0.10 [43]	± 0.01
ϵ_b	PARJ(55)	$0.0035^{+0.0015}_{-0.0010}$ [10]	± 0.16
ϵ_c	PARJ(54)	0.03 ± 0.02 [10]	± 0.08
$P(qq)/P(q)$	PARJ(1)	0.100 ± 0.015 [42]	∓ 0.01
Popcorn	PARJ(5)	0.5 ± 0.5 [42]	∓ 0.16
x_d	PARJ(76)	0.70 ± 0.05 [37]	∓ 0.08
x_s	PARJ(77)	$\infty \pm \infty$ [37]	± 0.00
		Total	**0.34**

Table 14: List of JETSET parameters and their ranges used in the fragmentation modelling systematic error study. Associated errors on A_{FB}^b are also shown.

9.4.2   Efficiency Estimation

As was seen in section 6.1, the b-tagging efficiency can be determined from the data alone and compared with that obtained in the Monte Carlo. In figure 31 we see that the difference between data and MC efficiency is never more than 1% absolute. It is a reasonable assumption that the fraction of each quark flavour in a particular sample, f_i, is known in the MC to a similar precision. Thus, by varying each f_i by 1% and summing in quadrature we can estimate the error on A_{FB}^b due to MC efficiency uncertainties.

9.4.3   Detector Effects

The non-ideal nature of the detector can affect the measurement in a number of ways. Most importantly, there can be a dependence of the charge tagging probability on

the thrust direction of the event. For example, events that have a thrust direction nearly orthogonal to the beam axis tend to be less efficient at tagging the direction of charge flow because of a migration of tracks from one hemisphere into the other. This can be accounted for by forming a weight for each event, $w = 1/(2P - 1)$, where P is the charge-tagging probability for that particular event, taking into account the direction of the thrust axis and the primary quark flavour. N_F'' and N_B'' are then the sum of the weights for forward and backward events respectively. If N is the total number of events then:

$$A'' = \frac{N_F'' - N_B''}{N} \tag{64}$$

$$A_{FB}^b = \frac{A'' + A_u[f_u + f_c] - A_d[f_d + f_s]}{f_b} \tag{65}$$

Since it is not clear whether the Monte Carlo accurately predicts the variation of P in different regions of the detector, the central value of A_{FB}^b is taken to be that obtained using equation (59) and half of the difference between equations (59) and (65) is taken as the systematic error due to detector effects.

9.4.4 Monte Carlo Statistics

All of the quantities taken from the Monte Carlo are determined with a finite number of simulated events. There is thus a statistical error associated with each which leads to an error in A_{FB}^b . The number of simulated events is large enough that this error is insignificant compared with other systematic errors.

9.5 Results

The various errors on the A_{FB}^b measurement are shown as a function of discriminant cut in figure 45 as well as the total error which is the quadratic sum of the different contributions. The data statistical error is clearly dominant. A discriminant cut of D=1.85 is chosen as the cut which minimises the total error. The data sample passing

this cut is made up of approximately 83% $b\bar{b}$ events. A summary of the systematic errors for this cut are given in table 15.

Source of Error	$\sigma A^b_{fb} \times 10^2$
fragmentation	0.34
tagging efficiency	0.54
detector effects	0.13
MC statistics	0.04
Total	**0.65**

Table 15: Systematic errors the A^b_{FB} measurement for a discriminant cut of 1.85.

We thus obtain:

$$A^{b,peak}_{FB} = 8.75 \pm 1.40(stat) \pm 0.65(sys)\% \tag{66}$$

where *peak* refers to the fact that the asymmetry is determined at the peak of the $e^+e^- \rightarrow Z \rightarrow f\bar{f}$ cross section ($\sqrt{s} = 91.26$ GeV) which is slightly different to $\sqrt{s} = m_Z = 91.1885$ GeV (the Z-pole). In the next section we shall discuss the conversion of the peak to the pole asymmetry, $A^{b,0}_{FB}$, as well as other small corrections that allow the extraction of $\sin^2 \theta^{eff}_w$.

9.6 Corrections to A^b_{FB}

The most important corrections to the measured A^b_{FB} are:

- Energy shift to $\sqrt{s} = m_Z$ and QED corrections. The latter are mainly due to initial state radiation from the incoming electron or positron which is not included in the definition of the pole asymmetry but is present in the data. These effects can be estimated with ZFITTER [8].

- QCD corrections: these mainly come from the approximation of the direction of flight of the primary quarks by the thrust axis. This effect has been calculated to first order in QCD [44] with a $\sim 25\%$ error.

95

- At the Z-pole, γ exchange and γZ interference have a small but finite effect on the measured asymmetry which, again, is not included in the definition of the pole asymmetry. The size of these effects are also estimated using ZFITTER.

The corrections are summarised in table 16.

Source	$\delta A_{fb}^b \times 10^2$
$\sqrt{s} = m_Z$	-0.13
QED corrections	+0.41
QCD corrections	+0.33 $\pm$0.0010
γ, γZ	-0.03
Total	+0.58 $\pm$0.0010

Table 16: Corrections to be applied to the measured asymmetry in the form $A_{FB}^{b,0} = A_{FB}^{b,peak} + \delta A_{fb}^b$. These values are taken from [10].

After all corrections, the pole asymmetry is

$$A_{FB}^{b,0} = 9.33 \pm 1.40(stat) \pm 0.65(sys) \pm 0.10(QCD)\% \qquad (67)$$

where the last term shows the error associated with the QCD correction uncertainty.

$\sin^2 \theta_w^{eff}$ is extracted from $A_{FB}^{b,0}$ in the context of the Standard Model using equation 17. The result is:

$$\sin^2 \theta_w^{eff} = 0.2333 \pm 0.0025(stat) \pm 0.0012(sys) \qquad (68)$$

where the systematic error includes the QCD error added in quadrature.

10   Conclusions

10.1   Coupling of the Z Boson to b-Quarks

We have presented two detailed measurements that gauge the coupling of the Z boson to b-quarks:

$$R_b = 0.2146 \pm 0.0017(stat) \pm 0.0033(sys) - 0.139 \ (R_c - 0.171)$$

$$A^b_{FB} = 9.33 \pm 1.40(stat) \pm 0.65(sys) \pm 0.10(QCD)\%$$

As discussed in section 3.3, these results can be used to put limits on the vector and axial vector couplings of the Z to b-quarks, c^b_v, c^b_a. The area in c^b_v, c^b_a space allowed by our measurements of R_b and A^b_{FB} is shown in figure 46. The size of the allowed regions follows from the experimental precision of the measurements. The R_b measurement constrains us to a range of radial distances measuring the strength of the Z-b coupling, whereas A^b_{FB} limits the angular range, measuring the degree of parity violation. Our results allow two regions which differ only by the sign of c^b_v and c^b_a. By convention, the third component of weak isospin of the b-quark is negative which restricts us to the negative allowed region in c^b_v, c^b_a space.

Superimposed is the Standard Model point for $m_{top} = 174$ GeV and our deduced value for $\sin^2 \theta^{eff}_w = 0.2333$. The Standard Model point ($c^b_v = -0.407$, $c^b_a = -0.591$) is contained within the allowed region.

Thus we must conclude from our measurements that no evidence is seen for a new physics contribution to $Z \rightarrow b\bar{b}$.

10.2   Flavour Universality

We can also use the results to test another assumption of the Standard Model, namely that of the flavour independence of the Z coupling to different fermions. We compare $\sin^2 \theta^{eff}_w$ deduced from A^b_{FB} with that deduced from the charged lepton forward backward asymmetry and the τ polarisation at L3, table 17 and figure 47. All three
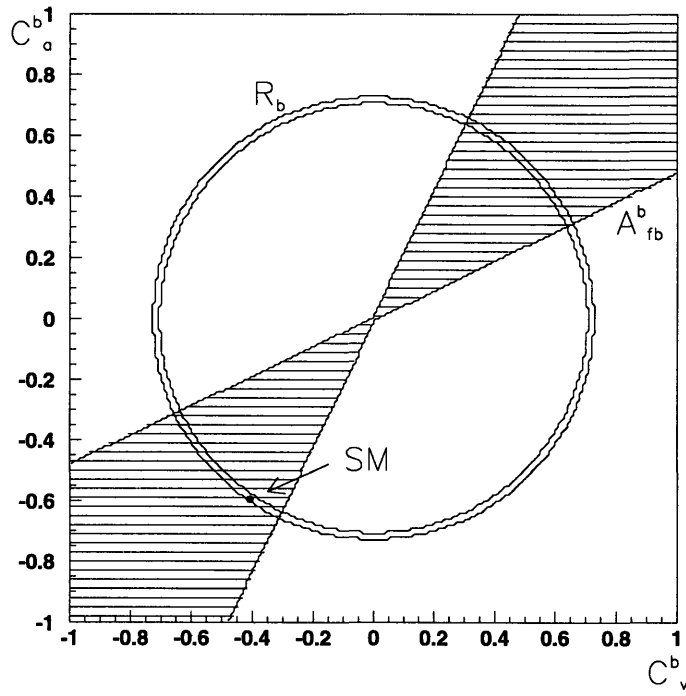
97

Figure 46: Regions in c_v^b, c_a^b space allowed by our measurements of R_b and A_{FB}^b . The area between the two concentric circles is that allowed by R_b , the shaded area is that allowed by A_{FB}^b . The Standard Model point is inside the allowed region.

L3

lepton FB asymmetry   —●—

τ polarisation   —●—

Afb(b) (this analysis)   ———●———

0.220   0.225   0.230   0.235   0.240

$$\sin^2\theta_W^{\text{eff}}$$
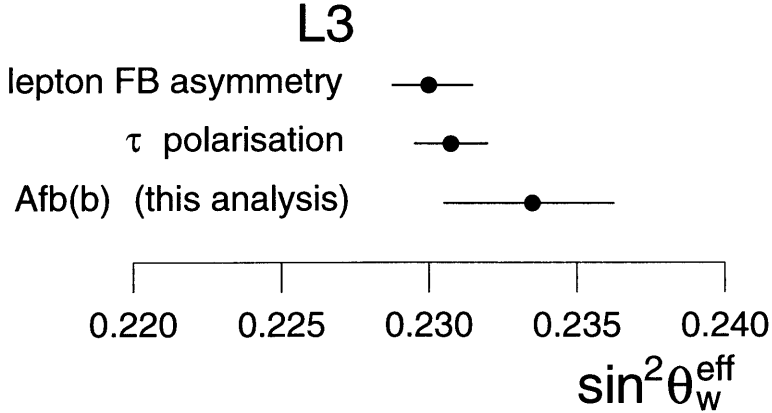
Figure 47: Graphical representation of the data in table 17.

determinations are consistent. This confirms, to the experimental precision, the Standard Model assumption that the Z couples equally to all quarks and leptons regardless of flavour.

Method	$\sin^2\theta_w^{eff}$
lepton FB asymmetry	0.2301 ± 0.0014 [45]
τ polarisation	0.2307 ± 0.0013 [45]
$A_{FB}^{b,0}$ (this analysis)	0.2333 ± 0.0028

Table 17: $\sin^2\theta_w^{eff}$ as determined at L3 using three methods.

10.3   Is There Still an R_b Discrepancy?

The R_b result obtained here is compared with those quoted in section 3.2 in in figure 48.

The analysis here is the most precise L3 measurement of R_b, illustrating the power of the lifetime tagging technique made possible by the Silicon vertex detector.

As demonstrated above, our measurement of R_b is entirely consistent with the Standard Model prediction for the Fermilab top mass of ~174 GeV. However, when all of the measurements are taken into account, the R_b values are consistently higher than the Standard Model . We must ask whether this can be interpreted as evidence

99

for a real discrepancy.

Systematic effects in the analysis and data between different experiments could account for the effect. For example, the hemisphere correlation factor C_b is calculated by all experiments in essentially the same way from the JETSET Monte Carlo. Simulation of correlations between the hemispheres is a subtle and complex issue depending on physics effects in the quark fragmentation as well as detector-dependent contributions. Since R_b is linearly proportional to C_b, any systematic error in the simulation leads to a systematic shift of all determinations of R_b which is very hard to quantify. For this reason alone, any attempt to average the R_b determinations as pseudo-independent results must be treated with a degree of scepticism. Other possible sources of common systematics could be found in the JETSET description of charm and light quark fragmentation although this is more understood and R_b is less sensitive to these effects. The modelling of gluon splitting to $c\bar{c}$ and $b\bar{b}$ pairs is another important source of possible common uncertainty.

We therefore consider our own measurement of R_b in isolation. We observe no evidence, to the measured precision, for a discrepancy in the Standard Model description of the Z branching fraction into b-quarks. The room allowed for new physics contributions to $Z \to b\bar{b}$ is given by $\sigma(R_b)/R_b = 1.7\%$ at 68% CL.

10.4   Prospects for Improvement

We have now reached the end of LEP 1 and no statistically significant e^+e^- data at the Z-peak are expected to be forthcoming in the near future. If we want to increase the precision of the R_b and A_{FB}^b measurements we must look for new ways to analyse the present data set. As the current R_b measurement error is systematics dominated, there is particular room for improvement in this channel.

Hemisphere correlations are an important part of the R_b determination. The dominant cause of the correlation is the single primary vertex that is used to calculate the impact parameters of tracks in each hemisphere. If separate vertices were determined using only the tracks in each hemisphere, the correlation could be reduced to a negligible amount and the systematic error from C_b would effectively disappear. To be

ALEPH lifetime

ALEPH event shape

ALEPH multivariate

DELPHI lifetime

DELPHI lepton

L3 event shape

L3 lepton

OPAL lifetime

OPAL lepton

this measurement

0.20   0.21   0.22   0.23   0.24

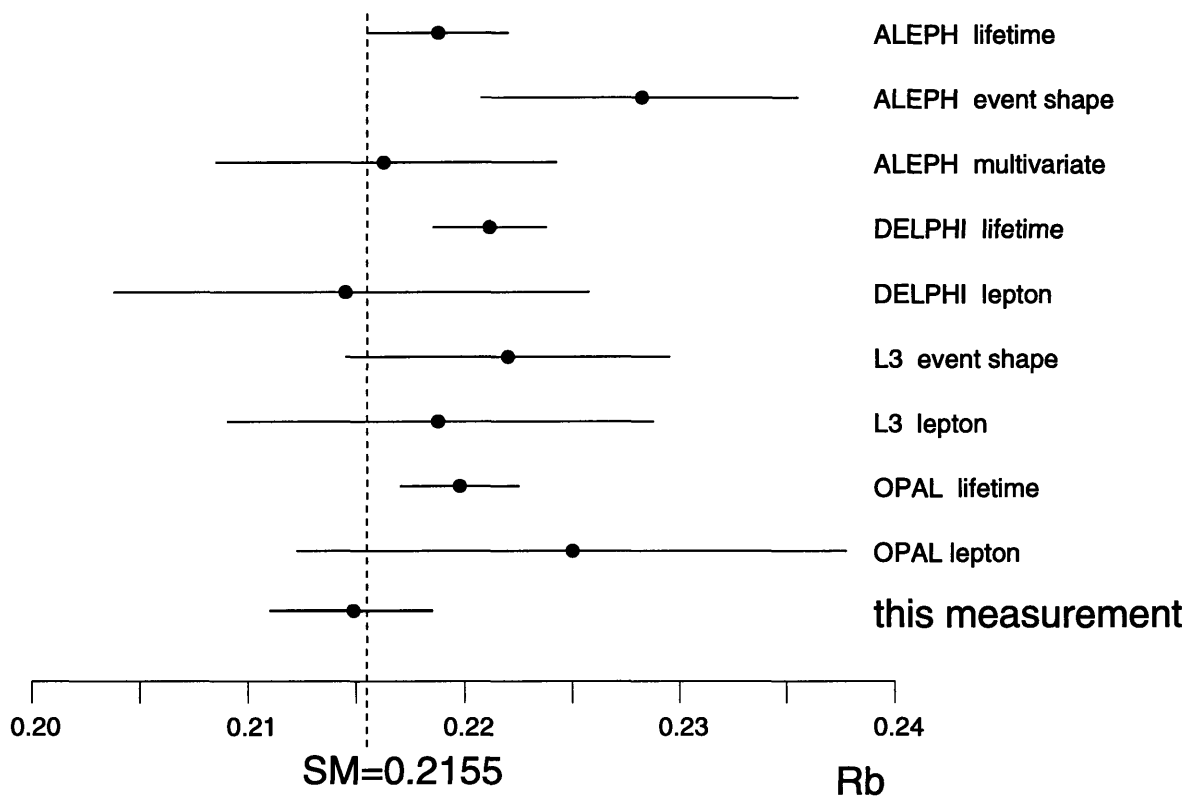SM=0.2155   Rb

Figure 48: This measurement of R_b compared with those referenced in section 3.2.

101

truly independent, however, the hemisphere vertices must be reconstructed without the 200-event vertex constraint. Unfortunately, the vertex finding described in this thesis has a low efficiency ($\sim 10\%$) for finding hemisphere vertices without this constraint and the increase in statistical error due the number of rejected events would far outweigh the decreased systematic error.

Improved tracking could increase this efficiency considerably. For example, fitting tracks with the aid of a Kalman Filter [46] would take into account the effect of multiple scattering in the detector materials in a more proper way than that presented in section 5.2.4. If this is combined with an effective way of adding three-dimensional information to tracks, vertexing and also impact parameter tagging efficiency would be improved.

If 3-D tracks are available, it is also possible to form a 'vertex mass' by determining the invariant mass of tracks associated with a secondary vertex [47]. This mass will be higher for $b\bar{b}$ events and can be used, in conjunction with the impact parameter significance, to increase tagging efficiency.

Three dimensional tracking is being developed at L3 and may be used in future heavy flavour analyses [48].

Further improvement could be made by the combination of several separate tags based on lifetime, lepton, vertex mass and event shape information [49].

These refinements could be reasonably expected to reduce the systematic error on R_b by around 10%.

10.5   Outlook

From our measurements of R_b and A_{FB}^b together with other electroweak results from table 2, we can now claim to understand physics of Z decay to an exceptional level. In particular, the influence of the newly discovered top quark via radiative corrections has been shown to be that predicted by the Standard Model.

At the end of LEP 1, the Standard Model has been spectacularly confirmed as the best description of fundamental interactions at scales of $\sim$100 GeV. The tentative indications of new physics observed in the R_b measurement have not crystallised into

more substantial evidence and could be explained in terms of the difficulties in taking into account common systematic effects among the different LEP results. It seems that signals of physics beyond the Standard Model will not be seen at these energies.

Although the SM has proved extremely successful at predicting LEP 1 results, there are still some missing links to be found. Now that the top quark has been discovered we are left with the as yet unobserved Higgs which is essential for the spontaneous symmetry breaking mechanism that gives the fundamental particles their mass. The details of the Higgs sector may well be revealed at LEP 2 or, later, at the Large Hadron Collider at CERN [50].

One unsatisfactory aspect of the SM is its reliance on a large number of parameters which must be supplied by experiment (three couplings, six quark masses, six lepton masses, one phase and three KM mixing angles, the Higgs mass and two vacuum expectation values). There are also many empirical facts left completely unexplained, such as: Why are there three fermion generations? Why are elementary particle charges quantified in the way they are? Why are P and CP violated? Why do baryon and lepton number appear to be conserved? This implies that the Standard Modelcannot conceptually be the end of the process of unification: some sort of larger symmetry is expected which will become manifest at higher energy scales. Despite much theoretical speculation [51], the form of this new physics is entirely unknown and can only be determined by experiment. We look forward to results from the next generation of colliders with great expectations.

Acknowledgements

I would like to thank Prof U. Becker, my research supervisor and Prof S.C.C. Ting, the spokesman of L3, for making this thesis possible.

I am also grateful to the following people for their help in these analyses (in alphabetical order):

Juan Alcaraz, Bruna Bertucci, Maria Chamizo, Aaron Dominguez, Sajan Easo, Riccardo Faccini, Peter Fisher, Steve Goldfarb, Joel Goldstein, Dirk Kamrad, Emanuel Leonardi, Alex Nippe, Christoph Paus, Magda Pedace, Gerhard Raven, Yoshi Uchida.

Finally, I would like to thank all of my family and friends for their encouragement and support over the years.

Appendix

A The Standard Model of Electroweak Interactions

We believe that all matter is made from quarks and leptons, interacting through the four basic forces of nature: gravity, electromagnetism and the weak and strong nuclear forces. It is one of the greatest intellectual achievements of the twentieth century to have united two of these forces, electromagnetism and the weak nuclear force, into a single *electroweak* force described by the so-called Standard Model. The SM provides a comprehensive description of electroweak phenomena that shows spectacular agreement with all experimental tests to date. It is the result of a long historical path of theoretical and experimental discovery.

A.1 Historical Overview

All modern theories of fundamental interactions are based on the theory of quantum electrodynamics worked out in the 1940s by Feynman, Schwinger and Tomonaga [52]. One of the most important aspects of this work is the concept of renormalisability, the technique of cancelling infinities that makes QED calculable. It was realised that future theories that attempted to describe other forces must at least satisfy this property.

The first attempt to unite the electromagnetic interactions of QED with the weak nuclear force was made by Schwinger in 1957 [53]. In this model, weak interactions were mediated by massive charged vector particles. In 1960, Glashow [1] and Salam [2] independently proposed a similar model which included the idea of gauge invariance, first proposed by Yang and Mills in 1954 [54]. As well as the charged mediators, called W^+ and W^-, this model featured a massive neutral mediating particle, the Z^0. At this time, neutral weak currents had not been observed. The masses of these gauge bosons were put in by hand. Unfortunately, the theory was not renormalisable

for massive intermediates.

A method of generating gauge boson masses in a more natural way was found by Higgs [55] building on the work of Goldstone [56]. A consequence of this *Higgs mechanism* was the presence of massive scalars - Higgs particles. In 1967, Weinberg and Salam independently published an electroweak model for leptons using the Higgs mechanism. An extension to the quark sector was made by Glashow, Illiopoulos and Maiani by the suggestion of an as yet unobserved fourth quark [4]. The renormalisability of this theory was shown by 't Hooft [57].

The key to establishing the Glashow-Weinberg-Salam theory was the first observation of neutral weak currents in 1973 [26]. More confirmation came in 1983 with the first direct observation of the W and Z particles with their predicted masses [27].

A.2   The Standard Model

Outlined below is a short description of the SM, particularly regarding neutral electroweak currents which form the substance of this thesis. More detailed descriptions can be found in, eg, [58], the works on which this outline is based. Familiarity with the techniques and results of QED is also assumed [59].

The building blocks of the Standard Model are the three generations of quarks and leptons. They interact by means of both charged and neutral currents. Parity violation experiments show that the charged current interaction is of a $V - A$ (vector - axial-vector) form and that the left handed fermions form doublet representations of an $SU(2)_L$ group. Right handed fermions form SU(2) singlets as shown in table 18. By analogy to isospin as applied to strong interactions, left handed fermions are assigned weak isospin=$\frac{1}{2}$, right handed fermions weak isospin=0.

The use of the notation d', s', b' in table 18 indicates that the electroweak eigenstates are not those of the strong interaction but are modified according to the Cabibbo-Kobayashi-Maskawa (CKM) formulation:

$$\text{fermion generation}$$

	I	II	III

$$\text{leptons} \quad \begin{pmatrix} \nu_e \\ e \end{pmatrix}_L \quad \begin{pmatrix} \nu_\mu \\ \mu \end{pmatrix}_L \quad \begin{pmatrix} \nu_\tau \\ \tau \end{pmatrix}_L$$
$$e_R \qquad \mu_R \qquad \tau_R$$

$$\text{quarks} \quad \begin{pmatrix} u \\ d' \end{pmatrix}_L \quad \begin{pmatrix} c \\ s' \end{pmatrix}_L \quad \begin{pmatrix} t \\ b' \end{pmatrix}_L$$
$$u_R \qquad c_R \qquad t_R$$
$$d'_R \qquad s'_R \qquad b'_R$$

Table 18: The three generations of quark and lepton arranged into weak isospin doublets and singlets for left and right handed fermions respectively.

$$\begin{pmatrix} d' \\ s' \\ b' \end{pmatrix} = M \begin{pmatrix} d \\ s \\ b \end{pmatrix} \tag{69}$$

where M is a 3×3 matrix.

We can also define *hyperharge*, Y:

$$Q = I_3 + \frac{Y}{2} \tag{70}$$

where Q is the fermion charge and I_3 the third component of its weak isospin. Y generates a symmetry group $U(1)_Y$, which incorporates the electromagnetic interaction.

The Standard Model is constructed from the convolution $SU(2)_L \otimes U(1)_Y$. $SU(2)_L$ describes an isotriplet of vector fields, W_μ^i coupled with strength g to the weak isospin current J_μ^i. $U(1)_Y$ describes a single vector field B_μ coupled with strength $g'/2$ to the weak hypercharge current j_μ^Y. The Lagrangian may be written as:

$$\mathcal{L} = -ig(J^i)^\mu W_\mu^i - i\frac{g'}{2}(j^Y)^\mu B_\mu \tag{71}$$

$W_\mu^\pm = \sqrt{\frac{1}{2}}(W_\mu^1 \mp iW_\mu^2)$ describe massive charged bosons. W_μ^3 and B_μ are neutrals. When the masses of the vector bosons are generated by the Higgs Mechanism, the

two neutral fields mix so that the physical states are

$$A_\mu = B_\mu \cos\theta_W + W_\mu^3 \sin\theta_W \tag{72}$$

$$Z_\mu = -B_\mu \sin\theta_W + W_\mu^3 \cos\theta_W \tag{73}$$

where θ_W is called the weak mixing angle. A_μ is a massless field and corresponds to the photon. Z_μ is massive and represents the Z^0.

The Higgs mechanism provides a relationship between θ_W and the masses of the gauge bosons:

$$\rho \equiv \frac{m_W^2}{m_Z^2 \cos^2\theta_W} \tag{74}$$

In the minimal Standard Model $\rho = 1$.

The coupling strengths g and g' are related to the electromagnetic strength e via:

$$g \sin\theta_W = g' \cos\theta_W = e \tag{75}$$

Thus g and g' can be replaced by e and θ_W, parameters that can be determined by experiment. Further, by requiring the calculations of weak charged current interactions to agree with the older Fermi $V - A$ theory, we obtain an expression for g as a function of the mass of the W boson, m_W and the Fermi coupling constant G_F:
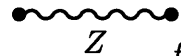
$$g^2 = \frac{8 G_F m_W^2}{\sqrt{2}} \tag{76}$$

In the Standard Model , $W^\pm$ couple to pairs of fermions from a weak isospin doublet, eg, (e, ν_e), (t, b'). This interaction is pure $V - A$. The Z^0 couples to fermion anti-fermion pairs $f\bar{f}$ with vector and axial-vector components C_V^f and C_A^f which depend on the type of fermion f:
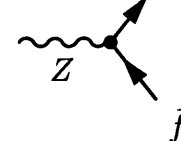
$$C_V^f = I_3^f - 2\sin^2\theta_W Q_f \tag{77}$$

109

$$C_A^f = I_3^f \qquad (78)$$

where I_3^f and Q_f are, respectively, the third component of isospin and the charge of fermion f. There are also direct couplings between W, Z and γ.

$Z \to f\bar{f}$ amplitudes can be calculated to first order from the Z propagator and vertex factors:

$$\frac{-i\left(g_{\mu\nu} - p_\mu p_\nu/m_Z^2\right)}{p^2 - m_Z^2} \qquad (79)$$

$$\frac{-ig}{\cos\theta_W}\gamma^\mu \frac{1}{2}\left(C_V^f - C_A^f\gamma^5\right) \qquad (80)$$

where $g_{\mu\nu}$ is the Minkowski metric, p is the four-momentum of the Z and γ^μ are the Dirac gamma matrices.

References

[1] S. Glashow, Nucl. Phys. 22 579 (1961).

[2] A. Salam and J. Ward, phys. lett. 13 168 (1964).

[3] S. Weinberg, Phys. Rev. Lett. 19 1264 (1967).

[4] S.L. Glashow, I. Illiopoulos, L. Maiani, Phys. Rev. D 2 1285 (1970).

[5] The first evidence for top quark observation was given by:

CDF collaboration, F. Abe *et al*, Phys. Rev. Lett. 73 225 (1994)

$(m_t = 174 \pm 10^{+13}_{-12}$ GeV$)$

Confirmation followed in:

CDF collaboration, F. Abe *et al*, Phys. Rev. Lett. 74 2626 (1995)

$(m_t = 176 \pm 8 \pm 10$ GeV$)$

D0 collaboration, S. Abacci *et al*, Phys. Rev. Lett. 74 2632 (1995)

$(m_t = 199^{+19}_{-21} \pm 22$ GeV$)$

The latest average from the Particle Data Group, R.M. Barnett *et al*, Phys. Rev. D54 1, (1996), is:

$(m_t = 180 \pm 12$ GeV$)$

[6] *Z Physics at LEP 1*, edited by G. Altarelli, R. Kleiss, C. Verzegnassi, CERN 89-08 (1989).

[7] W. Beenakker and W. Hollik, Z. Phys. C40 141 (1988).

[8] D.Bardin *et al*, CERN-TH 6443/92 (May 1992); Phys. Lett. B255 290 (1991); Nucl. Phys. B351 1 (1991); Z. Phys. C44 493 (1989).

[9] L3 Collaboration, O. Adriani *et al*, Phys. Rep. 236 (1993).

[10] The LEP collaborations ALEPH, DELPHI, L3, OPAL and the LEP Electroweak Working Group, CERN-PPE/95-172 (1995).

[11] See, for example, Proceedings of the EPS conference on High Energy Physics, Brussels 27 July - 2 August 1995.

[12] Contributions to the Moriond Workshop on R_b and R_c , XXXI Rencontres de Moriond, March 1996, CERN-PPE/96-91 (1996).

[13] ALEPH Collaboration, D. Buskulic *et al*, Phys. Lett. B313 535 (1993).

[14] ALEPH Collaboration, D. Buskulic *et al*, Phys. Lett. B313 549 (1993).

[15] ALEPH Collaboration, D. Buskulic *et al*, Z. Phys. C62 179 (1994).

[16] DELPHI Collaboration, Contributed paper EPS0570 to the EPS conference on High Energy Physics, Brussels, July 1995.

[17] DELPHI Collaboration, P. Abreu *et al*, Z. Phys. C66 323 (1995).

[18] L3 Collaboration, O. Adriani *et al*, Phys. Lett. B307 237 (1993).

[19] L3 Collaboration, O. Adriani *et al*, Phys. Lett. B292 454 (1994).

[20] OPAL Collaboration, Contributed paper EPS0278 to the EPS conference on High Energy Physics, Brussels, July 1995.

[21] OPAL Collaboration, R. Ackers *et al*, Z. Phys. C60 199 (1993).

[22] H. Przisieszniak, proceedings of XXXI Rencontres de Moriond, March 1996.

[23] H.P. Nilles, Phys. Reports 110 1 (1984).

[24] P. Chankowski, proceedings of XXXI Rencontres de Moriond, March 1996.

[25] P. Chiapetta, proceedings of XXXI Rencontres de Moriond, March 1996.

[26] F. Hasert *et al*, Phys. Lett. 46B, 138 (1973).

[27] G. Arnison *et al*, Phys. Lett. 122B, 103 (1983).
    G. Arnison *et al*, Phys. Lett. 126B, 398 (1983).

[28] L3 Collaboration, B. Adeva *et al*, Nucl. Inst. and Meth. A289 35 (1990);

L3 Collaboration, O. Adriani *et al*, Phys. Rep. 236 1 (1993).

[29] M. Acciarri *et al*, Nucl. Inst. and Meth. A351 300 (1994).

[30] A. Adam *et al*, Nucl. Inst. and Meth., A344 127 (1994);

A. Adam *et al*, Nucl. Inst. and Meth., A348 486 (1994).

[31] P. Bagnaia *et al*, Nucl. Instr. Meth. A317, 463 (1992); A324, 101 (1993).

[32] L3 Collaboration, B. Adeva *et al*, Z. Phys. C51 179 (1991).

[33] T. Sjöstrand, Comput. Phys. Commun. 82 74 (1994).

[34] The L3 detector simulation is based on GEANT Version 3.14; see R. Brun *et al*, GEANT 3, CERN DD/EE/84-1 (Revised), September 1987 and the GHEISHA program (H. Fesefeld, RWTH Aachen Report PITHA85/02, 1985) for the simulation of hadronic interactions.

[35] L3 Collaboration, B. Adeva *et al*, Nucl. Instr. Meth. A289 35 (1990).

[36] The LEP Experiments: ALEPH, DELPHI, L3, OPAL, *Combining Heavy Flavour Electroweak Measurements at LEP*, CERN-PPE/96-017.

[37] Particle Data Group, R.M. Barnett *et al*, Phys. Rev. D54 1, (1996).

[38] Mark III Collaboration, D. Coffman *et al*, Phys. Lett. B263 135 (1991).

[39] T. Aziz, M. Maity, Tata Inst. L3 note 2033 (1996).

[40] R.D. Field and R.P. Feynman, Nuc. Phys. B136 1 (1978).

[41] L3 Collaboration M. Acciarri *et al*, Z.Phys. C71:379-390 (1996).

[42] ALEPH Collaboration, D. Buskulic *et al*, CERN-PPE/96-09.

[43] OPAL Collaboration, R. Akers *et al*, CERN-PPE/95-50.

[44] Djouardi, Lampe and Zerwas, *A note on QCD Corrections to Forward-Backward Asymmetries of Heavy Quark Jets in Z decays*, MPI-Ph/94-81 (1994).

[45] L3 Lineshape Group, L3 Note 2065 (1997).

[46] *Trajectory Fit in Presence of Dense Materials*, V. Innocente, E. Nagy, Nucl. Instrum. Meth. A324 297 (1993).

[47] This technique was first described in SLD Collaboration, SLAC-PUB-96-7170 (1996).

[48] *UCSD 3D Neural Net B Tagging*, I. Fisk, L3 note 2089 (1997).

[49] See for example ALEPH Collaboration, Proceedings of the 28th International Conference on High Energy Physics, Warsaw, abstract PA10-015 (1996).

[50] *The LHC Conceptual Design Report*, CERN/AC/95-05(LHC) (1995).

[51] M.E. Peskin, SLAC-PUB-7479 (1997).

[52] R.P. Feynman, Phys. Rev. 76 749 and 769 (1949).

[53] J. Schwinger, Ann. Phys. 2 407 (1957).

[54] C.N. Yang and R.L. Mills, Phys. rev. 96 (1954).

[55] P.W. Higgs, Phys. rev. 145 1156 (1966).

[56] J. Goldstone, Nuovo Cimento 19 154 (1961).

[57] G. 't Hooft, Nucl. Phys. B35 167 (1971).

[58] F. Halzen and A. Martin, *Quarks and Leptons*, Wiley (1984).
E. Leader and E. Predazzi *An Introduction to Gauge Theories and Modern Particle Physics*, Cambridge University Press (1996).

[59] J.D. Bjorken and S.D. Drell, *Relativistic Quantum Mechanics*, McGraw-Hill (1964).